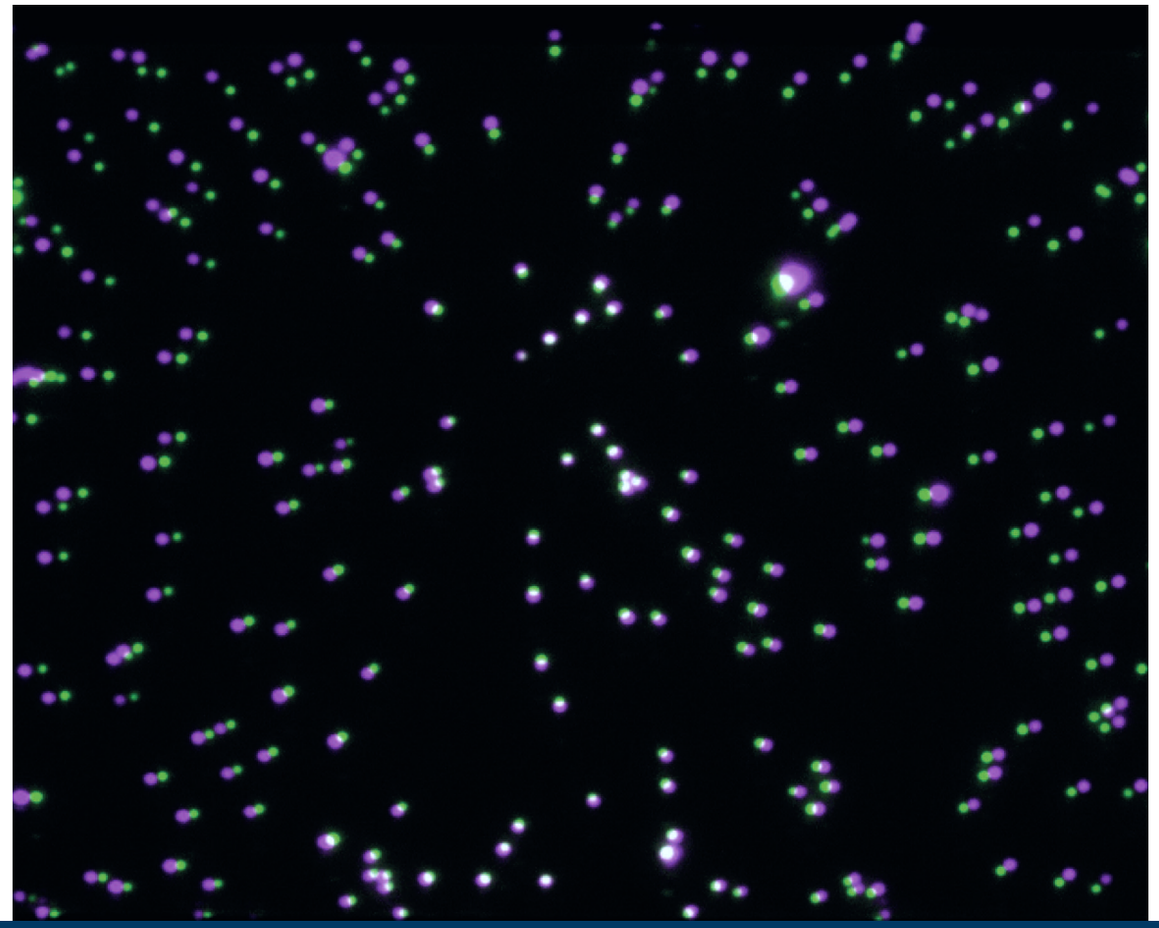

Simultaneous dual-color imaging on single-molecule level on a Widefield microscope and applications

Ralph Ledesch

Schlüsseltechnologien / Key Technologies
Band / Volume 178
ISBN 978-3-95806-348-8

Mitglied der Helmholtz-Gemeinschaft

JÜLICH
Forschungszentrum

Schriften des Forschungszentrums Jülich
Reihe Schlüsseltechnologien / Key Technologies Band / Volume 178

Forschungszentrum Jülich GmbH
Institute of Complex Systems
Molekulare Biophysik (ICS-5)

Simultaneous dual-color imaging on single-molecule level on a Widefield microscope and applications

Ralph Ledesch

Schriften des Forschungszentrums Jülich
Reihe Schlüsseltechnologien / Key Technologies Band / Volume 178

ISSN 1866-1807 ISBN 978-3-95806-348-8

Bibliografische Information der Deutschen Nationalbibliothek.
Die Deutsche Nationalbibliothek verzeichnet diese Publikation in der
Deutschen Nationalbibliografie; detaillierte Bibliografische Daten
sind im Internet über http://dnb.d-nb.de abrufbar.

Herausgeber und Vertrieb: Forschungszentrum Jülich GmbH
Zentralbibliothek, Verlag
52425 Jülich
Tel.: +49 2461 61-5368
Fax: +49 2461 61-6103
zb-publikation@fz-juelich.de
www.fz-juelich.de/zb

Umschlaggestaltung: Grafische Medien, Forschungszentrum Jülich GmbH

Druck: Grafische Medien, Forschungszentrum Jülich GmbH

Schriften des Forschungszentrums Jülich
Reihe Schlüsseltechnologien / Key Technologies, Band / Volume 178

D 82 (Diss., RWTH Aachen University, 2018)

ISSN 1866-1807
ISBN 978-3-95806-348-8

The complete volume is freely available on the Internet on the Jülicher Open Access Server (JuSER)
at www.fz-juelich.de/zb/openaccess.

Contents

1 Introduction **1**
- 1.1 The development of Fluorescence microscopy . . . 1
- 1.2 Intents and structure of this work . . . 3

2 Theoretical background **5**
- 2.1 Fluorescence . . . 5
  - 2.1.1 Electronic states and the Jablonski diagram . . . 5
    - Excitation . . . 6
    - Excited state lifetime . . . 6
    - Fluorescence . . . 6
    - Inter-system crossing and Phosphorescence . . . 6
    - Photo-destruction . . . 7
    - Rate equations and the fluorescence quantum yield . . . 7
    - Fluorescence rate and the molecular brightness . . . 8
    - Quenching . . . 8
- 2.2 Resolution in light microscopy . . . 9
  - 2.2.1 Gaussian approximation of the diffraction pattern . . . 10

3 Sample preparation **13**
- 3.1 Preparation of the Tetraspeck bead slides . . . 13
- 3.2 Buffers . . . 13
- 3.3 Single Alexa and Cyanine dyes in a polymer film . . . 14
- 3.4 Single GFPem on a plasma cleaned surface . . . 14
- 3.5 Photoprotection systems . . . 14
  - 3.5.1 GOC O_2-scavenging system . . . 15
  - 3.5.2 PCD/PCA O_2-scavenging system . . . 15
  - 3.5.3 Trolox solution . . . 15
- 3.6 Double-stranded DNA sample . . . 15
- 3.7 Ribosome samples . . . 16
  - 3.7.1 Multi-labeled ribosomes . . . 16
  - 3.7.2 Cell-free protein synthesis kit . . . 16
  - 3.7.3 Single-labeled re-associated ribosomes . . . 17

4 The Widefield microscope **19**
- 4.1 Introduction . . . 19
  - 4.1.1 Excitation path . . . 19
  - 4.1.2 Objective . . . 21
  - 4.1.3 Emission path . . . 22
    - Image splitter . . . 22
    - EMCCD camera . . . 22
  - 4.1.4 Nyquist criterion . . . 23
  - 4.1.5 Signal-to-noise-ratio and noise sources . . . 24
  - 4.1.6 Filter set spectra and the setup's transmission function . . . 26

4.2 Getting started with imaging . . . 29
4.2.1 Excitation intensity at the cover slide surface . . . 29
4.2.2 Alignment check with fluorescent beads . . . 32
4.2.3 Resolving performance of the setup . . . 32
4.2.4 Chromatic aberration . . . 36
4.2.5 Measurements in solution with a confocal microscope . . . 37

5 Data analysis **41**
5.1 Introduction . . . 41
5.2 The recorded image . . . 41
5.3 The analysis routine . . . 42

6 Imaging on single-molecule level **47**
6.1 Introduction . . . 47
6.2 Structure and photophysical properties of the employed fluorophores 47
6.2.1 Cy3 and Cy5 . . . 47
6.2.2 Alexa488 and Alexa647 . . . 49
6.2.3 GFP emerald . . . 49
6.3 Parameter optimization for the imaging of single fluorophores . . . 50
6.3.1 Observing single fluorophores on the surface . . . 50
6.3.2 Preliminary considerations . . . 52
6.3.3 Varying the illumination time . . . 53
Measurements . . . 53
Results and comments . . . 54
6.3.4 Power-series . . . 55
Observations and comments . . . 58
6.3.5 EM-gain series . . . 59
Preliminary considerations . . . 59
Measurements . . . 60
Results and comments . . . 61
6.4 Photoprotection . . . 63
6.4.1 Oxygen-scavengers . . . 63
6.4.2 The O_2-scavengers' impact on the observation time . . . 64
The labeled streptavidin-conjugates . . . 65
GFP emerald . . . 67
6.4.3 Comments . . . 68

7 Surface preparation: Tethering single molecules **69**
7.1 Introduction . . . 69
7.2 Slide preparation protocol . . . 69
7.3 The slide background . . . 73
7.4 Testing the slide performance with Alexa647-streptavidin . . . 74
7.5 Testing the linker accessibility with Atto655-conjugated biotin . . . 78
7.6 Testing the slide performance with Cy5-multilabeled bioCAN-ribosomes and GFPem . . . 79
7.7 Observations and comments . . . 79

8 Results: Observing functional ribosomes on single-molecule level **81**
8.1 Introduction: Colocalization measurements on the surface . . . 81
8.2 Preliminary measurements with double-labeled DNA . . . 81
8.2.1 Measurement . . . 81

8.2.2 Data analysis . . . 82
8.2.3 Results and comments . . . 82
8.3 Surface measurements of GFPem synthesized by exogenous modified ribosomes . . . 84
8.3.1 Introduction to the project . . . 84
8.3.2 Negative controls . . . 85
8.3.3 Measurements with the confocal microscope and co-precipitation 85
FCS and TCCD measurements . . . 85
Co-precipitation measurements . . . 87
8.3.4 *In vitro* measurement on plasma cleaned glass slides . . . 87
8.3.5 Data analysis and results . . . 89
8.4 Measurements on bioPEG-slides . . . 90
8.4.1 *In vitro* measurement . . . 90
8.4.2 *In situ* measurement . . . 90
8.4.3 Results and comments . . . 91
8.5 Re-associated ribosomes . . . 94
8.5.1 The measurements . . . 94
8.5.2 Results . . . 94
8.5.3 Stability of the re-associated ribosomes . . . 95
8.5.4 Results and comments . . . 96

9 Conclusions **99**
9.1 Imaging on single-molecule level . . . 99
9.2 The WFM as a tool for quantitative surface measurements on single-molecule level . . . 101

A Appendix **103**
A.1 Filter spectra . . . 104
A.2 Convolution of the setup's transmission function with the emission spectra of the employed fluorophores . . . 105
A.3 Illumination intensity . . . 107
A.4 Determination of the molecular brightness . . . 107

Acknowledgements **109**

Bibliography **111**

List of Abbreviations

a	aperture radius
BG	background level
BSA	bovine serum albumine
c	speed of light
cc	correction collar
CCD	charge coupled device
CE	collection efficiency of the objective
D	diffusion coefficient
DE_{dye}	detection efficiency of the setup of a dye
d_{min}	minimum resolvable distance between two diffraction-limited objects
E_{ex}	excitation energy
E_{det}	detection efficiency of the CCD
E_{SNR}	arithmetic mean of the signal-to-noise ratio
EMCCD	electron-multiplying charge-coupled device
EM-gain	electron-multiplying gain register
e^-	electron
F	fluorescence intensity time-trace
f	threshold factor
FCS	fluorescence correlation spectroscopy
FRET	Förster resonance energy transfer
FWHM	full width at half maximum
g	gravitational acceleration
GFP	green fluorescent protein
GFP_{em}	GFP emerald
GOC	glucoxe oxidase/ catalase
h	Planck constant
IC	internal conversion
ISC	inter-system crossing
J	excitation intensity
J_{sat}	saturation intensity
J_1	Bessel function of the first kind, first order
k	wave vector
k_{bl}	bleaching rate
k_{ex}	excitation rate
k_{isc}	rate of inter-system crossing
k_{nr}	rate of non-radiative decay
k_{ph}	phosphorescence rate
k_{10}	fluorescence rate
mB	molecular brightness
n	refractive index
NA	numerical aperture
N_{e^-}	number of photoelectrons
N_γ	number of photons

NHS	N-hydroxysuccinimide
PCA	3,4-Dihydroxybenzoic acid
PCD	Protocatechuate 3,4-dioxygenase
PEG	polyethylene glycol
PSF	point spread function
PVA	polyvinyl alcohol
P_{tot}	total measured excitation power
QY	fluorescence quantum yield
RMS	root mean square deviation
SNR	signal-to-noise ratio
S_n	higher excited singlet state
S_0	electronic ground state
S_1	first excited single state
s_0	occupation probability of S_0
s_1	occupation probability of S_1
T	temperature
TCCD	two-color coincidence detection
TS	TetraSpeck microspheres
t_{dbDM}	transmission function of the dual-band dichroic mirror
t_{dbEM}	transmission function of the dual-band emission filter set
t_{DMlp}	transmission function of the long-pass dichroic mirror
t_{obj}	transmission function of the objective
t_{obs}	observation time
t_{tot}	total transmission
T_1	first triplet state
t_1	occupation probability of T_1
VR	vibrational relaxation
WD	working distance
WFM	Widefield microscope
γ	photon
Δ	Nyquist sampling distance
Θ	half maximum opening angle
λ_{em}	emission wavelength
λ_{ex}	excitation wavelength
μ	mean of the Gaussian distribution
ν_{ex}	excitation frequency
ν_{10}	fluorescence frequency
σ	overall noise
σ_{dn}	dark noise
σ_{dye}	absorption cross-section
σ_{rn}	read noise
σ_{sn}	shot noise
$\sigma_{x,y}$	width of the Gaussian distribution along x-axis/ y-axis
τ	fluorescence lifetime

To my parents.

Chapter 1

Introduction

1.1 The development of Fluorescence microscopy

Abstracted from [1–4]

The epifluorescence microscope, as we know it today, has come a long way. Starting as a spin-off to the UV microscope at the beginning of the twentieth century, its development over the last century has made it a powerful tool, allowing the study of biological processes on single-molecule level in unprecedented detail.

The first fluorescence microscope, with UV illumination, was developed at Carl Zeiss by the german physicists Otto Heimstaedt and Heinrich Lehmann. Between 1925 and 1932, Philipp Ellinger and August Hirt from Heidelberg conceived the UV intravital microscope, that allowed them to study the distribution of previously injected fluorescent dyes in living kidney and liver of frogs and mice [5, 6] to study their deposition and transport through the blood vessels. The setup is considered the prototype epifluorescence microscope: Unlike the previously built transmitted light microscopes, where the illumination light source is transmitted from the opposite side of the specimen from the objective, in their setup, the objective itself acted as the illumination condenser. While the emitted red-shifted fluorescence was transmitted and imaged on a diapositive, the reflected UV light was blocked by a yellow filter, placed between the objective and the ocular. In contrast to the transmitted light microscope, the illumination light is not detected, resulting in a higher image contrast, while at the same time alignment problems could be avoided. The evolution to the modern epifluorescence microsope is due to the contributions of the russian scientist Evgenii Brumberg (State Optical Institue of Leningrad) and Johann Sebastiaan Ploem, a microscopist from the University of Amsterdam. They are responsible for the development of the dichroic beamsplitter, a key element in every modern fluorescence microscope. It physically separated the excitation light from the much weaker fluorescence signal, by deflecting the unwanted back-reflected excitation light [7]. Up to the 1950s, fluorescence microscopes used excitation light ranging from the UV to the blue spectra, that was isolated from (mercury or xenon) arc lamps by optical filters. The steadily increasing number of developed fluorophores were not necessarily optimally illuminated within the UV spectra only. In 1962, Ploem collaborated with the Schott glass company in Mainz to extend the spectral range for illumination, by producing dichroic filters (or mirrors), that deflected the blue and green spectra [8]. Furthermore, Ploem collaborated with the Ernst Leitz company, which constructed the first inverted microscope with epi-illumination and combined the optical filter(s) and the dichroic mirror in a unit (the filter cube). The filter cubes were arranged to match the excitation/emission spectra of the employed fluorophore. Mounted in a turret below the objective, they could be interchanged

conveniently to match the spectra of the imaged fluorophore.

Since its early development, fluorescence microscopy has been closely related to the field of fluorescent labeling. The observed sample's autofluorescence was often weak and resulted in a poor image contrast.
Herwig Hamperl, a pathologist from the university of Vienna and Max Haitinger, an expert in fluorescence microscopy, examined systematically the staining of organic tissues with more than 65 different fluorophores and introduced the fluorescence microscopy to the field of histology [9].
In 1941, Albert Coon, an American physician, labeled for the first time antibodies with a fluorophore, to bind them to their antigen, allowing the visualization of the distribution of the target molecule through the observed sample [10]. Coons' contributions initiated the highly specific fluorescent staining of the specimen and established the field of immunofluorescence.
The discovery of the green fluorescent protein (GFP) from the jellyfish *Aequorea victoria* in 1962 by Osamo Shimomura [11], was followed by extensive cloning in the following decades, to find new variants with enhanced brightness and photostability [12, 13], reduced oligomerization, better pH insensitivity and a faster maturation time [14, 15]. Roger Tsien's studies contributed much to the understanding of how GFP works. He engineered several mutations with improved spectral and fluorescent characteristics over the wild type GFP and developed mutations with different excitation and emission spectra throughout the visible spectra [14, 16]. This marked an immense gain to the field of microbiology, as the fluorescent protein's amino acid sequence could be used as a label to study the transport within a cell, but also its amino sequence could also be incorporated and expressed in a wide variety of organisms and cell types for structural and functional studies [17, 18]. The ongoing development of fluorophores with distinct excitation/ emission spectra and improved brightness and photostability [19], as well as photo-activatable fluorescent proteins and dyes [20, 21] have contributed to the new imaging techniques of super-resolution microscopy, that go beyond the diffraction-limit.

Up to the 1950's, imaging depended on traditional photomicrography with emulsion-based film and illumination times over one minute. The ongoing development of photodetectors and image-processing technologies since the 1940's led to the transition to digital imaging. With the invention of the photodiode by John Shive in 1948 and the development of the first charged-coupled device (CCD) camera in 1969, by George Smith and Willard Boyle from the AT&T Bell Labs, the incident photon signal could be converted into electrons and stored digitally. The invention of the laser in 1960 and its consequent development opened new possibilities to the field of fluorescence microscopy: Their much higher excitation intensities, when compared to conventional arc lamps, allowed a much higher fluorescence output and contrast, as well as an increased time-resolution. The performance of the microscope relied not only on its optical components, but also on the sensitivity of its photodetectors. Continuous improvements in the last 50 years have lead to photodetectors, such as high-sensitivity CCD [22] and electron-multiplying CCD cameras, that are sensitive enough to detect single photons. The technological advances have paved the road for single-molecule fluorescence microscopy techniques, that allowed the removal of the usual ensemble averaging and made it possible to study the otherwise hidden heterogeneity within a biological sample. Furthermore, the site-specific labeling of the sample, in combination with the high sensitivity of the setup, allowed dynamical studies on single-molecule level, such as the probing of a sample's conformational

changes by Förster resonance energy transfer (FRET), as well as the tracking of single particles on the surface.

The most basic illumination mode in epifluorescence microscopy is the conventional widefield illumination (WFM), where the surface is evenly flooded with illumination light. A variation of it is the total internal reflection fluorescence microscope (TIRF), that achieves an improved contrast by exciting the sample with evanescent light only at the very proximity of the glass/water interface [23–25]. In contrast, the focused illumination of the confocal microscope only illuminates the sample and only collects fluorescence from within the confined focal volume, by blocking out-of-focus light with a pinhole at the (con-)focal plane of the objective lens [26]. Both illumination modes are applied in biological studies. By their nature, they are commonly used to fulfill different tasks and can be considered complementary. On single-molecule level, the WFM allows the simultaneous imaging of several hundred distinct single molecules within the objective's field of view, at a time-resolution ranging from milliseconds to seconds. The implementation of multi-color excitation sources and multi-band pass filters, in combination with the high sensitivities of the setup, have allowed the study of conformational dynamics of single immobilized proteins, as well as co-translational protein folding, by methods of colocalization microscopy and single-molecule FRET (smFRET)[27–29]. The WFM has been used on single-molecule level to study the motion of fluorescently labeled motor proteins, that drive intracellular transport in eukaryotes [30]. Furthermore, the WFM has been employed to determine the orientation of immobilized single-molecules by studying their dipole radiation patterns with de-focused imaging [31].

The excitation intensities in a confocal microscope are typically much higher than in a WFM, due to the confinement of the focused excitation light. The illumination allows for much higher fluorescence rates and hence, the investigation of temporal processes in the sub-millisecond time range, that remain inaccessible to the WFM. In solution, confocal microscopy allows the characterization of the diffusing sample by Fluorescence correlation spectroscopy (FCS) [32]. FCS has become a standard tool, allowing the determination of a sample's characteristic diffusion coefficient, aggregation state, kinetic chemical reaction rates, as well as concentration. At single-molecule concentrations, the confocal microscope allows to perform two-color-coincidence-detection (TCCD) measurements, as well as smFRET, allowing the monitoring of the unfolding pathways of a labeled sample [33].

1.2 Intents and structure of this work

This work documents the necessary steps to image and analyze a surface-immobilized dual-colored biological sample on single-molecule level, by means of a WFM. The WFM was used as an independent tool, to provide quantitative results and to answer biologically relevant questions on single-molecule level, that would stay hidden in the averaging of ensemble measurements. The thesis is divided into the following chapters:

The following chapter 2 introduces the reader to fluorescence microscopy, by covering the necessary theoretical basics in fluorescence and diffraction-limited optics.

The WFM setup and its major components will be presented in chapter 4. In particular, the different types of noise will be introduced and their impact on the image quality (signal-to-noise). First measurements are presented to determine the WFM's excitation intensity at the surface and the setup's resolution performance in the relevant spectral ranges.

Chapter 5 introduces the analysis routine, that was employed to retrieve the desired information from the imaged fluorescence peaks' intensity distributions and to identify colocalizations in the case of simultaneous dual-color measurements.

The fluorophores that are relevant to this work, as well as their photophysical characteristics and limitations to single-molecule imaging, are introduced in chapter 6. Systematic measurements will be presented, that were done to find measuring parameters, that allowed the imaging of single molecules with a signal strength high enough, to be reliably detected with the methods of data analysis. Second, two different photoprotection systems were tested concerning their impact on the fluorophores' observation time.

The WFM was employed to image a sample, that has been immobilized to the surface of a glass cover slide. Chapter 7 presents the corresponding cover slide functionalization, that allows to bind the sample on the surface for the long-term observation, while maintaining its functionality.

Having set up the the methodological basics to perform dual-color imaging on single-molecule level, chapter 8 introduces several applications, that reveal the WFM microscope as an independent tool, to monitor and quantify single and rare events on the surface. On the example of a cell-free protein synthesis experiment (CFPS), the synthesis of GFP by modified ribosomes was studied. A colocalization experiment on the surface allowed to quantify the fraction of active ribosomes and to make a statement about the stalling efficiency of the used plasmid, employed to keep the synthesized GFP bound to the active ribosome. Also, the synthesis of GFP was observed *in situ* on the surface, here the increasing number of synthesized GFP could be monitored directly over time. Furthermore, on the surface, the samples are typically added at very low concentrations in the pM-concentration range. On the example of site-specifically single-labeled re-associated ribosomes, the WFM was used on one hand to determine the time of stability of the specific labeling below the construct's dissociation constant k_d, while in a second step, colocalization measurements over time where done to monitor, if the ribosomes dissociate over time, which would become visible by a decrease in the fraction of colocalized signals.

Chapter 2

Theoretical background

2.1 Fluorescence

Abstracted from [34–39]

Definition 1. *Fluorescence: Spontaneous emission of radiation (luminescence) from an excited molecular entity with the formation of a molecular entity of the same spin multiplicity. [40]*

2.1.1 Electronic states and the Jablonski diagram

A quantum mechanical system like an atom, a nucleus or a fluorescent dye can only exhibit quantized values of energy, called energy levels or electronic states. Mathematically, an electronic state is described by a combination of wave functions of each electron, in each of the orbitals of the molecule. Electronic states and the transitions

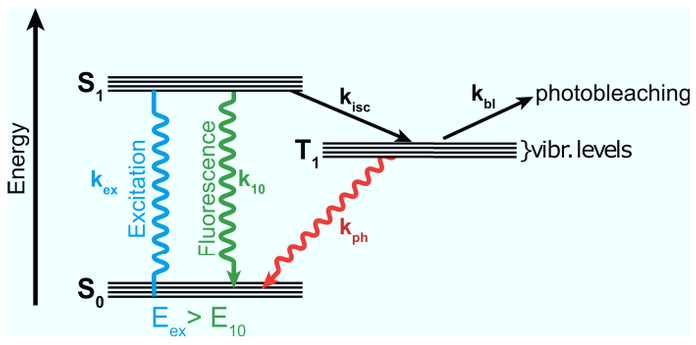

FIGURE 2.1: The Jablonski diagram with the main photophysical transitions of a fluorophore [34].

between them are typically illustrated in a Jablonski diagram. Figure 2.1 displays a Jablonski diagram that takes into account three electronic states: the ground state S_0, the first excited state S_1 and the first triplet state T_1. The electronic states are arranged vertically by energy and grouped horizontally by multiplicity. The relevant transitions, between the mentioned states, are illustrated by the different arrows and will be described in the following.

Excitation

Starting from the ground state S_0, light from the ultraviolet or visible spectrum can be absorbed by a molecule's electron, that lifts it to the first excited state S_1. The amount of transferred energy E_{ex} corresponds to the energy difference between S_0 and S_1. E_{ex} is given by

$$E_{ex} = \frac{h \cdot c}{\lambda_{ex}} = h \cdot \nu_{ex}, \tag{2.1}$$

with h being the Planck constant, c the speed of light, λ_{ex} the excitation light's wavelength and ν_{ex} the excitation frequency. In our case, the fluorescent dye or fluorophore will be exposed to laser light and the number of electrons, that are excited per second is given by the excitation rate k_{ex} ($[k_{ex}] = \frac{N_\gamma}{s}$)

$$k_{ex} = \sigma_{dye} \cdot J. \tag{2.2}$$

σ_{dye} is the absorption cross-section of the dye ($[\sigma_{dye}]$=cm^2), with typical values $\sim 10^{-16}\,\mathrm{cm}^2$. σ_{dye} is characteristic to a fluorophore and defines the capacity for light absorption at a given excitation wavelength. J is the intensity of the excitation light ($[J]=\frac{N_\gamma}{s \cdot cm^2}$). The process of excitation happens nearly instantaneously, on a time scale on the order of $10^{-15}\,\mathrm{s}$.

Excited state lifetime

After excitation, the electron resides in a vibrational level of an excited state, depending on the amount of absorbed energy. The fluorescent dye may undergo conformational changes and interact with its molecular environment. In general, the first transition after excitation (on a time scale of 10^{-14}-$10^{-11}\mathrm{s}$) is the vibrational relaxation down to the lowest vibrational level of the excited state S_1, by partly transferring the energy either to another electron of the same molecule or to a molecule in its surroundings. The lifetime of the excited state is typically on the order of 10^{-9} to $10^{-8}\mathrm{s}$. From the lowest vibrational level of S_1, the electron will then dissipate its energy by a number of radiative and/or non-radiative processes.

Fluorescence

Fluorescence is the only possible radiative transition by an electron from the S_1 down to S_0. Returning to S_0, the electron will emit a photon with an energy E_{10} that is typically smaller than the excitation energy, because of vibrational relaxation before and after emission. The fluorescence emission wavelength λ_{em} is red-shifted with respect to the excitation wavelength λ_{ex}. This is the characteristic Stokes shift of a molecule. The Stokes shift is an important criterion for fluorescence imaging techniques, as it allows the spectral separation of the emission light from the excitation light.

Inter-system crossing and Phosphorescence

Depending on the fluorophore and its environment, the electron transitions from S_1 to the triplet state T_1. The transition is called inter-system crossing (ISC). Quantum mechanically, it is a 'forbidden' transition that involves a change in the electron's spin-multiplicity. In general, the transition is less probable and happens on a much slower time scale than any other transition in the Jablonski diagram (in the range of

10^{-8} to 10^{-3}s).
Once in the triplet state T_1, the electron is trapped and can only return to the ground state S_0 by a second forbidden transition. The radiative transition is called phosphorescence. Photon emission by phosphorescence happens on a time scale of 10^{-3} to 10^{2}s.

Photo-destruction

The absorption/emission process is a cyclical stimulation of a fluorophore into fluorescence emission. This process comes to a halt after having completed a certain number of cycles on the order of 10^4 to 10^6, known as the irreversible photo-destruction or bleaching of the molecule. Bleaching is caused by a photochemical modification of the fluorophore . While being a stochastic process, the number of completed cycles depends critically on the fluorophore's chemistry and the excitation intensity and time it is exposed to. Another major factor is the fluorophore's environment. Being lifted to the excited state, a molecule is prone to oxidation by generated reactive oxygen species, especially singlet oxygen ($^1O_2$), resulting in the premature photo-destruction of the fluorophore. Bleaching is a severe constraint in fluorescence microscopy [41], it will be addressed in more depth in chapter 6.

Rate equations and the fluorescence quantum yield

The different states' probability of occupation is given by the rate equations

$$\dot{s}_0 = -k_{ex} \cdot s_0 + k_{10} \cdot s_1 + k_{ph} \cdot t_1, \tag{2.3}$$
$$\dot{s}_1 = k_{ex} \cdot s_0 - k_{10} \cdot s_1 - k_{isc} \cdot s_1 - k_{bl} \cdot s_1, \tag{2.4}$$
$$\dot{t}_1 = k_{isc} \cdot s_1 - k_{ph} \cdot t_1, \tag{2.5}$$

with k_{10} corresponding to the transition rate of fluorescence from S_1 to S_0, k_{isc} and k_{ph} to the rate of inter-system crossing and to the rate of phosphorescence and k_{bl} corresponding to the bleaching rate.
A fluorophore's fluorescence lifetime τ ([τ]=s) is defined by the following relation

$$\tau = \frac{1}{k_{10} + k_{nr}}, \tag{2.6}$$

where k_f is the fluorescence emission rate and k_{nr} is the sum of the non-radiative rate constants $k_{nr} = k_{isc} + k_{bl}$.
The fluorescence quantum yield QY is the probability that the molecule emits a photon when leaving the excited state S_1. QY is defined as the fraction of absorbed photons N_{abs} by a molecule that are emitted by fluorescence N_{em}:

$$QY = \frac{N_{em}}{N_{abs}} = \frac{k_{10}}{k_{10} + k_{nr}}. \tag{2.7}$$

The fluorophores used in fluorescence microscopy display typically a QY of $\sim$ 20-90%.

Fluorescence rate and the molecular brightness

The fluorescence rate k_{10} ([k_{10}] = $\frac{N_\gamma}{s}$), is given by

$$k_{10} = QY \cdot \sigma_{dye} \cdot J. \tag{2.8}$$

k_{10} is proportional to the fluorescence quantum yield and the molecular absorption coefficient of the fluorophore σ_{dye} [1].
The rate of fluorescence per fluorophore, that is collected by a setup, is defined as the fluorophore's molecular brightness mB ([mB]=$\frac{N_\gamma}{molecule \cdot s}$). mB is given by the following relation

$$mB = k_{10} \cdot E_f, \tag{2.9}$$

with E_f corresponding to the fluorescence detection efficiency of the setup. E_f quantifies the fraction of fluorescence output, that is collected by the setup. It is given by

$$E_f = CE \cdot \int f_{dye}(\lambda) \cdot t_{tot}(\lambda) d\lambda, \tag{2.10}$$

where CE corresponds to the collection efficiency of the setup's objective (the spherical sector of light entering the objective, 4), $f_{dye}(\lambda)$ corresponds to the normalized emission spectra of the fluorophore and $t_{tot}(\lambda)$ corresponds to the total transmission function of the setup (further details are found in chapter 6).

A high brightness is desired for reasons of detection sensitivity and its advantage of requiring a lesser amount of excitation light, resulting also in lesser photodestructive effects and bleaching.

Quenching

Quenching is an inter-molecular process that decreases a probe's fluorescence QY and hence, fluorescence intensity. Several mechanisms can result in quenching, but it origins in the short-range interactions between the fluorophore and the molecular environment (for example the oxygen-induced quenching of a fluorescent state (chapter 6)) or other fluorophores. Unlike photobleaching, quenching is a reversible process and it is at the basis of Förster resonance energy transfer assays.

[1] Equation 2.8 is valid under the assumption, that the excitation intensity J is below the intensity of saturation J_S of the fluorophore ($k_{ex} << \frac{1}{\tau}$), which is the case for the measurements done with the WFM).

2.2 Resolution in light microscopy

Abstracted from [42–46].
An optical microscope's resolving power is fundamentally limited by the laws of physics. Even the most advanced aberration-corrected lens cannot overcome the barrier of diffraction.
In fluorescence microscopy, the image of an emitting point-source will, because of diffraction and aberrations, not show an infinitesimal small spot. Rather the light waves collected by the objective's eye lense in the setup will converge and interfere to form a diffraction pattern at the image plane (depicted in figure 2.2).

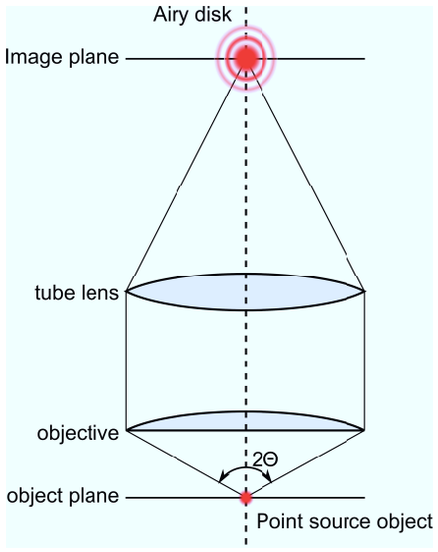

FIGURE 2.2: An objective collects a cone of light from an emitting point-like source at the focal plane. The light passes the optical system and will be focused by the objective's tube lens. Due to diffraction, the focused light will interfere and form an intensity pattern at the imaging plane, known as the Airy disk.

This diffraction pattern is known as the point spread function (PSF) of the optical system. Its size and appearance depend on the fluorescence wavelength, as well as on the objective's specifications. At the image plane of an optical system, the pattern is called Airy disk (after George Biddell Airy, 1801-1892). A simulated Airy disk is shown in figure 2.3. It consists of a bright central spot called zeroth order maximum and several concentric rings, the higher order maxima.

In 1874, Baron Rayleigh formulated one definition for resolution: Two Airy disks that are close together can still be resolved as separate entities, if the zeroth order maximum of the first Airy disk lies in the first minimum of the second Airy disk. The minimal distance between the two centers that can be resolved is given by the well-known Rayleigh criterion:

$$d_{min} = 0.61 \cdot \frac{\lambda_{em}}{NA}, \tag{2.11}$$

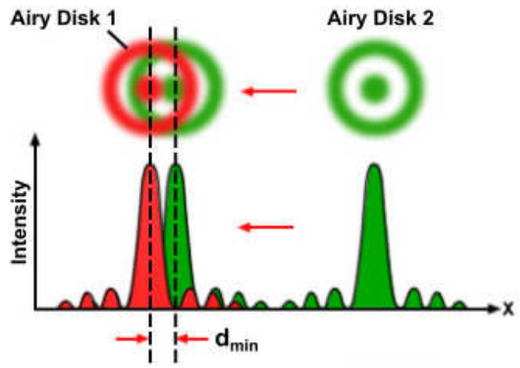

FIGURE 2.3: An Airy disk on the right along with a pair of Airy disks near the limit of optical resolution according to the Rayleigh criterion [47].

with λ_{em} being the emitted fluorescence wavelength and NA the numerical aperture of the objective. The NA is defined as

$$NA = n \cdot sin(\theta), \tag{2.12}$$

it gives a measure for the objective's ability to collect light in a medium with the refractive index n, further details are found in chapter 4.

While the NA is is a fixed characteristic of the setup, d_{min} is proportional to λ_{em} of the emitted light. The smaller λ_{em}, the nearer two point sources can be, while still being resolved as two distinct entities. Hence, in the spectra of visible light, the best resolving power is achieved with fluorescence from the blue or near ultra-violet spectra.

2.2.1 Gaussian approximation of the diffraction pattern

Mathematically, the Airy intensity distribution can be described by the Fraunhofer diffraction pattern of a circular aperture. The intensity pattern shown in figure 2.4 is given by the following formula

$$I_\theta = I_0 \cdot (\frac{2J_1(kasin(\theta))}{kasin(\theta)})^2 = I_0 \cdot (\frac{2J_1(x)}{x})^2, \tag{2.13}$$

with $k = 2 \cdot \pi/\lambda$ being the wave number, a the radius of the circular aperture and θ the angle of observation. $J_1(x)$ is the Bessel function of the first kind of the first order. At the image plane, $J_1(x)$ has consecutive zero points at the distances x=3.8317, 7.0156, 10.1735,... of the optical axis. 83.8% of the total power is concentrated within the central lobe, 91% within the second ring and 93.5% within the third.

The Rayleigh criterion determines the minimal distance between two point sources that can still be resolved. In practice, a more straightforward approach to characterize the resolution performance of an optical system is to determine the so-called 'full width at half maximum' (FWHM) of a point source's intensity distribution (e.g. sub-resolution sized fluorescent beads), as shown in figure 2.4. Therefore, the intensity

distribution of the diffraction pattern (PSF) is fitted with with a two-dimensional Gaussian:

$$I(x,y) = I_0 \cdot e^{-(\frac{(x-\mu_x)^2}{2\sigma_x^2} \cdot \frac{(y-\mu_y)^2}{2\sigma_y^2})}, \tag{2.14}$$

where $\sigma_{x,y}$ are the standard deviations along both axis and $\mu_{x,y}$ correspond to the mean of the intensity distribution. By employing the Gaussian model, the outer rings of the Airy diffraction pattern will be ignored, yet for our purposes, it describes the zeroth order maximum of the Airy disk sufficiently well. Fitting the center lobe

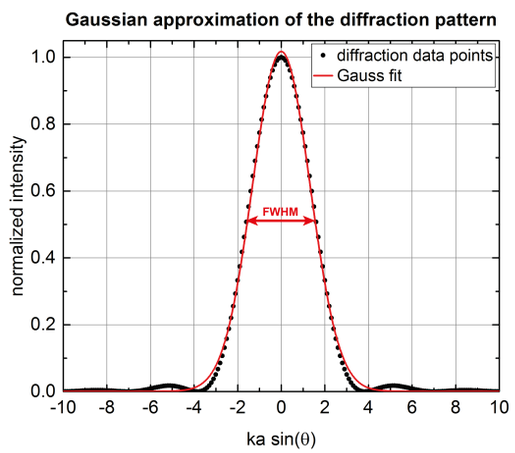

FIGURE 2.4: The profile of the intensity pattern of a diffraction-limited object and the corresponding Gaussian approximation

of the diffraction pattern provides σ of the Gaussian approximation. The $FWHM_{x,y}$ of the fit relate to $\sigma_{x,y}$ as follows:

$$FWHM_{x,y} = \sigma_{x,y} \cdot 2\sqrt{2ln(2)}. \tag{2.15}$$

It should be noted that the $FWHM_{x,y}$' size are slightly smaller than the minimal resolvable distance d_{min} from the Rayleigh criterion, between two Airy disks (formula 2.11):

$$FWHM_{x,y} = 0.51 \cdot \frac{\lambda_{em}}{NA}. \tag{2.16}$$

Chapter 3

Sample preparation

3.1 Preparation of the Tetraspeck bead slides

The alignment of the WFM (chapter 4) was checked with cover slides, that had been stained with fluorescent sub-resolution sized beads (TetraSpeck microspheres with a diameter of $0.1\,\mu\mathrm{m}$ from ThermoFisher Scientific, Massachusetts, USA). The TetraSpeck (TS) slides were prepared by spin-coating $5\,\mu\mathrm{l}$ of the undiluted TS bead stock-solution at a rotational speed of $100\,\mathrm{rps}$ on a square cover slide. The employed high-precision cover slides with a size of $22\,\mathrm{mm} \times 22\,\mathrm{mm}$ and a guaranteed thickness of $0.17 \pm 0.05\mathrm{mm}$ were plasma-cleaned before spin-coating to remove organic dirt from the surface. The spin-coating of the TS bead solution resulted in a density of ≈150 well distributed TS beads per imaged area of $40\,\mu\mathrm{m} \times 40\,\mu\mathrm{m}$ (an example is given in figure 4.12). The TS bead slides were stored in a box and could be used for at least a year at ambient conditions.

3.2 Buffers

The imaging buffers used during the experiments were prepared by dissolving the chemicals in milli-Q water. The prepared buffers were filtered with sterile filters in order to remove dust particles, bacteria and fungi. Stored at $4\,^{\circ}\mathrm{C}$, they were used for a maximum of 1 week. Depending on the sample requirements, three different types of buffers were used:

- **Tico buffer**
  Tico was the standard imaging buffer, employed during the parameter optimization for GFPem (chapter 6), during the surface functionalization tests (chapter 7) and the colocalization measurements with the exogenously modified ribosomes (chapter 8):
  $20\,\mathrm{mM}$ Hepes, $10\,\mathrm{mM}$ $Mg(OAc)_2$, $30\,\mathrm{mM}$ NH_4OAc and $4\,\mathrm{mM}$ β-mercaptoethanol, pH 7.6.

- **DNA buffer**
  The DNA buffer was used during the preliminary measurements with the double-stranded DNA (see 8.2 on page 81) [48]:
  $20\,\mathrm{mM}$ Tris, $100\,\mathrm{mM}$ NaCl, $10\,\mathrm{mM}$ $MgCl_2$, pH 7.5.

- **Poly-Tris buffer**
  The Poly-Tris buffer was used during the imaging of the re-associated single labeled ribosome subunits (see 8.5 on page 94), as it leads to an optimal oligonucleotide binding [49]:
  $50\,\mathrm{mM}$ Tris-OAc, $100\,\mathrm{mM}$ KCl, $5\,\mathrm{mM}$ NH_4OAc, $0.5\,\mathrm{mM}$ $Ca(OAc)_2$, $10\,\mathrm{mM}$ $Mg(OAc)_2$, $6\,\mathrm{mM}$ β-mercaptoethanol, $5\,\mathrm{mM}$ putrescine, $1\,\mathrm{mM}$ spermidine, pH=7.5.

The putrescine, spermidine as well as the β-mercaptoethanol were added to the filtered and autoclaved buffer, just before the experiment took place.

3.3 Single Alexa and Cyanine dyes in a polymer film

For the imaging parameter optimization (chapter 6), the relevant single fluorophores were embedded in a polymer film, that was spin-coated on a plasma cleaned cover slide.
The used fluorophore conjugates were the cyanine dyes Cy3-NHS ester and Cy5-NHS ester (from GE Healthcare Life Sciences, UK), as well as the Alexa fluors conjugates Alexa488-NHS ester and Alexa647-NHS ester (from ThermoFisher Scientific, Massachusetts, USA). The respective dyes were embedded in a poly-vinyl-alcohol (PVA) matrix (Mowiol 18-88 form Sigma-Aldrich, Miss.,USA), a water-soluble synthetic polymer that was chosen for its refractive index between 1.52-1.53 when dry, matching the refractive index of the glass cover slide. A 2%-solution (by mass) of PVA was prepared and filtered with $0.1\,\mu\mathrm{m}$ syringe filter (Whatman Puradisc, Sigma-Aldrich, Miss., USA). $10\,\mu\mathrm{l}$ of a low dye concentration ($\leq 50\,\mathrm{pM}$) in PVA were spin-coated (at a rotational speed of $100\,\mathrm{rps}$) on a plasma cleaned cover slide, resulting in approximately 200 separated single peaks per $40\,\mu\mathrm{m} \times 40\,\mu\mathrm{m}$ area. Stored in a box and kept clean, the prepared slides could be used for a prolonged amount of time at ambient conditions and were commonly used for the routine alignment check of the setup. In contrast, for the systematic imaging parameter optimization, the slides were freshly prepared. A section from an example of the recorded images with Cy5-NHS embedded in PVA is shown in figure 6.4 on page 51.

3.4 Single GFPem on a plasma cleaned surface

In the context of the imaging parameter optimization (chapter 6) and the surface functionalization test procedures (chapter 7), a GFP emerald (GFPem) stock solution was required. The one, that was employed during the measurements, came from an expression in *E.coli*. *E.coli* had been transformed with a plasmid, that contained the same GFPem sequence as used in the later experiments. The standard was stored at $-80\,^{\circ}\mathrm{C}$. After thawing, it was stored at $4\,^{\circ}\mathrm{C}$. Before use, the GFPem stock was centrifuged for 10 minutes at a rotational speed of $14\,000\,\mathrm{rpm}$, to remove eventual aggregations. The condition of the GFPem sample was checked by an FCS measurement. The determined diffusion coefficient should correspond to the diffusion coefficient of single GFPem: $120\,\mu\mathrm{m}^2/\mathrm{s}$. An example of a recorded FCS curve for GFPem is shown in figure 4.13 on page 39. A dilution of GFPem of approximately $50\,\mathrm{pM}$, injected into the imaging chamber and rinsed after 1 minute with $3\,\mathrm{ml}$ of Tico-buffer, resulted in a density of approximately 200 GFPem adsorbed on a $40\,\mu\mathrm{m}^2 \times 40\,\mu\mathrm{m}^2$ area. An example, recorded during the imaging parameter optimization (chapter 6), is shown in figure 6.7 on page 55).

3.5 Photoprotection systems

Our goal was to observe the labeled molecules of interest for a prolonged amount of time. Therefore, the photostability of the fluorophores needed to be increased.

This was done by adding a photoprotection system to the imaging buffer. Two O_2-scavengers and one triplet quencher have been tested in this context (chapter 6).

3.5.1 GOC O_2-scavenging system

The glucoxe oxidase from *Aspergillus niger* and catalase from bovine liver (both from Sigma-Aldrich, USA) came as a lyophilized powder and were stored at $-20\,°\mathrm{C}$. Both components are sold in units/g or units/mg respectively. The final concentration used is 20 units/ml for the glucose oxidase and 200 units/ml of catalase in Tico buffer. For the ease of use, a 100-fold stock of the GOC system as well as a 10-fold stock of glucose were prepared. Both components were stored at $4\,°\mathrm{C}$. Prior to their use, the stocks were centrifuged for 10 minutes at a rotational speed of $14\,000\,\mathrm{rpm}$ to remove aggregates that could introduce an unwanted background signal to the surface measurements.

3.5.2 PCD/PCA O_2-scavenging system

Protocatechuate 3,4-dioxygenase (PCD) from the *Pseudomonas* species came as a lyophilized powder and was resuspended and stored as a 50% glycerol stock in $50\,\mathrm{mM}$ KCl, $1\,\mathrm{mM}$ EDTA and $100\,\mathrm{mM}$ Tris-HCl set to a pH value of 8. 3,4-Dihydroxybenzoic acid (PCA) was resuspended to $100\,\mathrm{mM}$ in de-ionized water and it was adjusted with NaOH to a pH value of 9, according to [50].

3.5.3 Trolox solution

Trolox was dissolved in methanol to have a stock concentration of $100\,\mathrm{mM}$ that could be stored at $4\,°\mathrm{C}$. The final concentration in the measuring buffer was $1\,\mathrm{mM}$, according to [51].

3.6 Double-stranded DNA sample

Labeled DNA was used as a test sample for the later carried out colocalization measurements on single-molecule level. Two DNA strands were used: The first DNA strand had a length of 48 base pairs and was modified with an Alexa488 dye and an Alexa647 dye at the opposite ends of the strand (IBA Lifesciences, Göttingen, Germany). Before the measurement took place, an unlabeled complementary strand of 48 base pairs (Eurofins Scientific SE, Luxembourg) was added to the DNA-solution in a 100-fold excess to stabilize the labeled DNA strand and hence prevent the bending of the strand, that could eventually lead to FRET and thereby to a potential decrease in fluorescence intensity of the dyes. A sketch of the DNA sample is shown in figure 3.1.

FIGURE 3.1: Sketch of the double-labeled single DNA strand of 48 base pairs and its unlabeled complementary strand. The double-stranded DNA has a length of $\approx 16\,\mathrm{nm}$.

3.7 Ribosome samples

The applications presented in chapter 8, the Cell-free protein synthesis study and the study concerning the stability of re-associated ribosomes at single-molecule concentration, involved two different ribosome samples, its preparation will be presented in the following [52].

3.7.1 Multi-labeled ribosomes

The employed 70S ribosomes for the CFPS study [1] were purified from *Escherichia coli*. The ribosomes were prepared from a ribonuclease deficient strain (CAN20/12-E) to avoid the degradation of ribosomal RNA. The ribosomes were biotinylated *in-vivo* with a single biotin at the uL4 ribosomal protein of the 50S ribosome subunit, allowing their specific binding on a functionalized surface. After biotinylation, the ribosomes were labeled overnight with NHS-Cy5 at the accessible amine groups on both subunits of the ribosome (at the N-terminus of the polypeptide chain as well as in the side-chain of the Lysine residues) by reacting with the N-hydroxysuccinimide (NHS) ester functionalized Cy5 in a pH environment ranging from 7.2 to 9. Due to the high number of lysines at the surface, the ribosomes carry multiple labels, in average 7 dyes per ribosome [52].

3.7.2 Cell-free protein synthesis kit

For the cell-free protein synthesis (CFPS) of the GFPem by the ribosomes, the translation-kit (PURExpress Δ Ribosome Kit NEB #E3313) was prepared as it is advised by the manufacturer [53]. The reaction, performed at a temperature of $37\,^{\circ}\mathrm{C}$, contained

- $10\,\mu\mathrm{l}$ of the kit's solution A,
- $3\,\mu\mathrm{l}$ of the kit's factor mix,
- $500\,\mathrm{nM}$ of the previously mentioned biotinylated Cy5-labeled CAN20/12E ribosomes and
- $5.5\,\mathrm{nM}$ of the linear plasmid DNA, that was modified with an enhanced arrest sequence (SecM strong [54]) to keep the folded GFPem bound to the ribosome after the translation step.

After adding Tico buffer to a final volume of of $25\,\mu\mathrm{l}$, the ribosomes synthesized the GFPem *in-vitro* during an incubation time of two hours. For the *in situ* experiment on the surface, the reaction was scaled up to a total volume of $50\,\mu\mathrm{l}$.

[1] The ribosome preparation and characterization was done by Cristina Remes from ICS-5: Molecular Biophysics, Forschungszentrum Jülich

3.7.3 Single-labeled re-associated ribosomes

Within the framework of a re-associated ribosome study, ribosomal subunits 30S and 50S from the bacterial strain ZS-22 (from E.coli, a kind gift from Prof. Knud Nierhaus, Charite, Berlin) were site-specifically labeled by hybridizing fluorescently modified oligonucleotides to mutated ribosomal RNA loops, resulting in single-labeled subunits with one Cy3 and/or Cy5 dye each respectively. The resulting complex had a dissociation constant k_d of $5\,\mathrm{nM}$.

The labeling reaction was made in Poly-Tris buffer by mixing 1 to $5\mu\mathrm{M}$ of ribosomes with a 30-times excess of modified oligonucleotides in a thermomixer for an incubation time of 15 minutes at $37\,^{\circ}\mathrm{C}$, followed by 20 minutes at $30\,^{\circ}\mathrm{C}$.

After the purification of the labeled ribosomes by centrifugation, the labeling ratio was determined by measuring the absorbance of the ribosomes at $260\,\mathrm{nm}$ and the absorbance of the dyes at $550\,\mathrm{nm}$ and $640\,\mathrm{nm}$ respectively. The relation lead reproducibly to a labeling ratio of one dye per subunit.

The re-association of the ribosomal subunits is done in an environment with a high concentration of Mg^{2+} at a temperature of $40\,^{\circ}\mathrm{C}$ and a 50% excess of the Cy3-30S subunits. After a gradient centrifugation, the 70S fraction (re-associated ribosomes) are collected and centrifuged overnight. The pellet was washed with $1\,\mathrm{ml}$ of Tico buffer and dissolved in $50\,\mathrm{ml}$ of Tico buffer at $4\,^{\circ}\mathrm{C}$.

Chapter 4

The Widefield microscope

4.1 Introduction

Imaging was done on a home-built inverted microscope, set up as a WFM. This chapter describes the setup and its major components. A sketch of the setup is depicted in figure 4.1.

4.1.1 Excitation path

Fluorescence imaging starts with the excitation of the sample. Excitation was done with continuous-wave optically pumped semiconductor lasers (Coherent Inc., California, USA). The excitation wavelengths, shown in table 4.1 match the excitation spectra of the fluorophores: Alexa488, Alexa647, Cy3, Cy5 and GFP emerald (chapter 6, section 6.2). The linearly polarized laser beams had a diameter of approximately $1\,\mathrm{mm}$. In order to eliminate noisy spontaneous emission of the laser output, clean-up filters, with a very narrow bandwidth, were mounted in front of every laser source. The three excitation beams were superimposed on one optical axis. An acousto-optic tunable filter (AOTF.nc-TN from AA optoelectronics, France) allowed to selected between the three different excitation wavelengths independently by remote control. The superimposed laser beams passed two condenser lenses with a $50\,\mu\mathrm{m}$ pinhole, mounted in between, at the lenses' focal distance. This so-called spatial filter or mode cleaner [55] removes aberrations in the beam, resulting in a cleaner Gaussian beam profile. The laser beam was then directed to the entrance level of the microscope tower. Before reaching the microscope tower (IX-81 IX2series ZDC, Olympus, Japan), the laser beam's diameter was expanded and focused to the back focal plane of the objective. Only the central part of the laser beam's Gaussian intensity profile is selected and the beam intensity, reaching the back focal plane, is more homogenous. Thus, a more even illumination of the sample is achieved.
Located in a turret, below the objective, are two filter cubes, that allow the imaging within the two spectral range combinations (green/red and yellow/red).

TABLE 4.1: Excitation wavelengths of the three excitation lasers

Laser	central wavelength λ_{ex} (nm)
Sapphire 488-200 CW	488±2
Sapphire 532-150 CW	532±2
Obis 639-150 CW	639±2

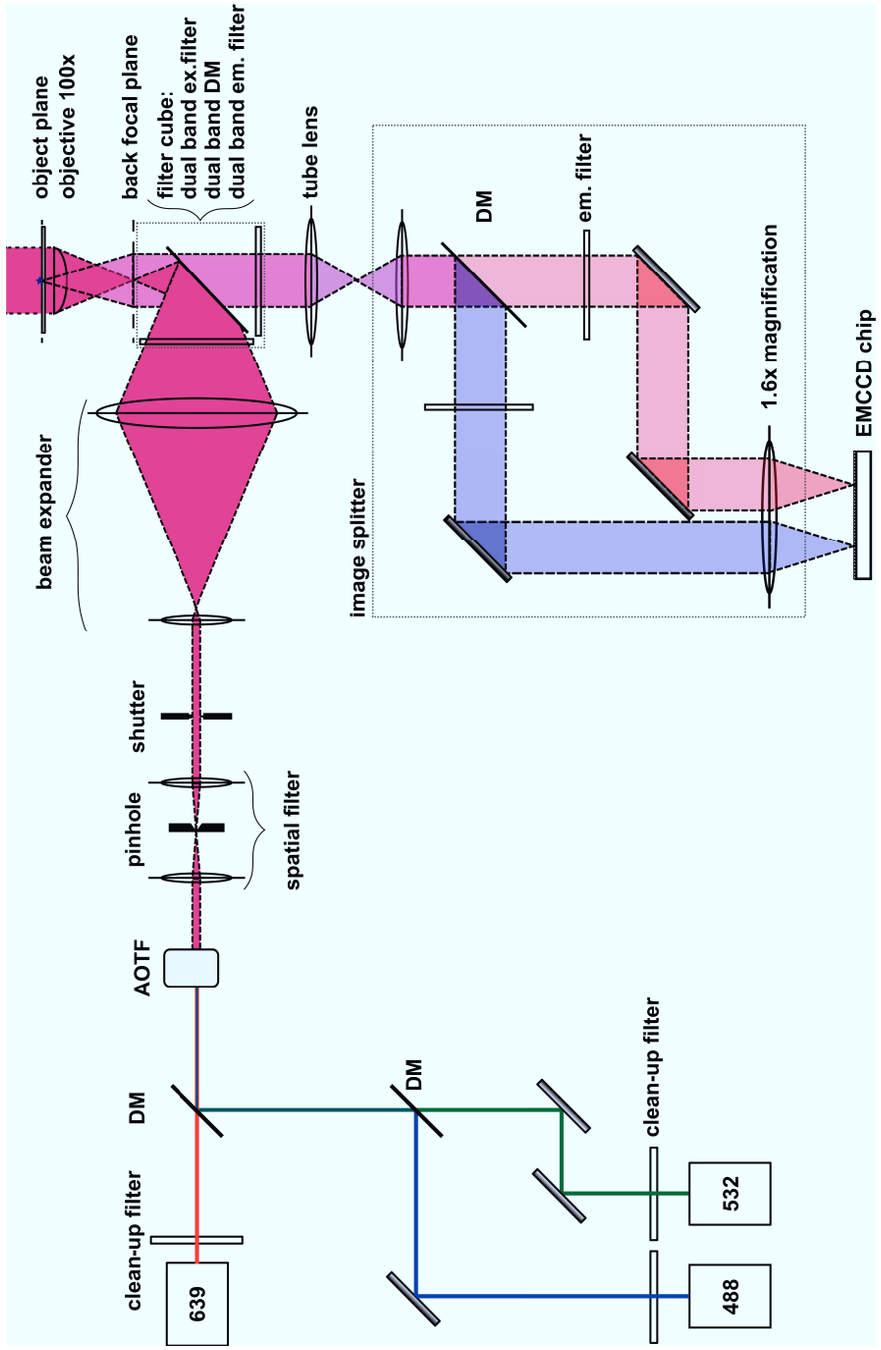

FIGURE 4.1: Shematic depiction of the WFM setup with its most important components. The dashed line box shows the beam path inside the image plitter used for colocalization experiments.

Each filter cube houses a dual-band filter set, consisting of the excitation filter, the dichroic mirror and the emission filter (see section 4.1.6 on page 26).
After having passed the excitation filter, the laser beam is reflected by the dichroic mirror and guided through the objective onto the sample.

4.1.2 Objective

In epifluorescence microscopy, the objective is used as the illumination condenser, as well as the fluorescence light collector. It is mounted in a turret below the microscope stage. The microscope stage is motorized along the z-axis. It allows the positioning of the stage in steps of $100 \pm 10\text{nm}$ (according to the microscope's specification sheet). Considering a fluorophore at focal distance from the objective (at the surface/ air-glass interface), the objective does not collect all the fluorescence emitted by the fluorophore, but only a fraction of light, a spherical sector of a maximum opening angle of 2Θ (illustrated in figure 4.2).

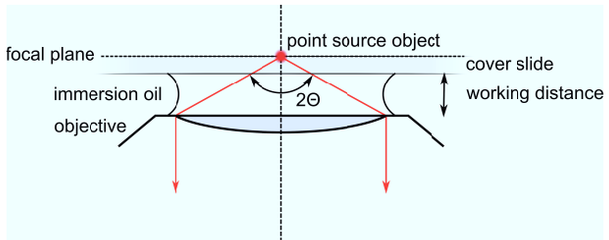

FIGURE 4.2: The objective's maximum opening angle

On single-molecule level, imaging requires the collecting of as many photons emitted by the sample, as possible. The photon yield depends critically on two characteristics: The objective's numerical aperture (NA) and its transmission function (section 4.1.6) in the spectral range of interest. The NA gives a measure for the objective's ability to collect light in a specified medium with a refractive index n:

$$NA = n \cdot sin(\Theta). \tag{4.1}$$

Θ represents half of the maximum opening angle, at which the objective is still able to collect light. The NA is one of the objective's major parameters, determining the resolution ability of the objective. The employed objective (UAPON 100XOTIRF, Olympus, Japan) is an oil-immersion objective. The employed immersion-oil's (Olympus immersion oil, n=1.516 at T=23 °C) refractive index matches the refractive index of the glass cover slide. The objective's specified NA of 1.49 leads to a maximum opening angle of $80.7°$. Originating from a point-source at the cover slide interface, the fraction of light entering the objective, over the total fluorescence emitted by the fluorophore (the radiation being modeled by a sphere), is the objective's collection efficiency CE

$$CE = \frac{V_{sph.sector}}{V_{sphere}} = \frac{1}{2}(1 - cos\theta). \tag{4.2}$$

An opening angle of $80.7°$ results in a collection efficiency of 0.419, the objective collects 41.9% of the emitted light.

A large opening angle results in a low working distance (WD). WD is defined as the distance between the front end of the objective lens and the closest cover slide surface, when the sample is in focus. In this setup, the objective's specified WD is $0.1\mathrm{mm}$.
The objective has a correction collar (cc), that allows the adjustment of the inner lens group to accommodate for variations in the cover slide thickness (ranging from 0.13 to $0.19\mathrm{mm}$), that can lead to spherical aberration. By employing high precision cover slides (High precision 1.5H cover slides, Marienfeld-Superior, Germany), with a thickness of $0.170 \pm 0.005\mathrm{mm}$, the need for correction-collar adjustments should be minimized.

The objective is an apochromat: Its optical elements are designed to focus 3 different colors (typically blue, green and red) at the same focal plane [56]. This is important in the context of simultaneous dual-color imaging, where the fluorescence signal of a diffraction-limited object should colocalize in both color channels (section 4.2.4).

The relation between the objective's 100x magnification and the area's size, that will be ultimately recorded by the setup's camera, will be discussed at the end of section 4.1.3.

4.1.3 Emission path

Once the sample has been excited, the fluorescence, collected by the objective, passes the filter cube. The dual-band dichroic mirror separates the fluorescence from reflected excitation light. The signal passes a dual-band emission filter, removing any unwanted wavelength. Details on the employed filter sets are given in section 4.1.6.
Having passed the filter cube, the fluorescence signal is guided to the image splitter.

Image splitter

For simultaneous dual-color imaging, the recorded image was split (spectrally as well as spatially) by an image-splitter (OptoSplit II, Cairn Research, UK). The schematic depiction of the image-splitter is found in figure 4.1 on page 20, marked by the dashed square. At the entrance of the image-splitter, the two-color-signal passes a rectangular aperture. The aperture adjusters allow to clip the imaged area to a size, that fills half of the chip ($13.2\,\mathrm{mm} \times 6.6\,\mathrm{mm} \equiv 40\,\mu\mathrm{m} \times 80\,\mu\mathrm{m}$). A long-pass dichroic mirror (DCLP 600DCXR, Omega Optical Inc, N.Carolina, USA) inside the image-splitter separated the two-color signal according to its spectral range. The two components, representing the two color channels of the same $40\,\mu\mathrm{m} \times 80\,\mu\mathrm{m}$ area, are then positioned side by side, using mirrors. The two components are further magnified by a factor of 1.6 by a pair of condenser lenses, before being focused onto the camera chip where image formation takes place. The image obtained by the camera chip is divided in two sections: The lower energy component of the signal (red channel) next to the higher energy part of the signal (green or yellow channel respectively).

EMCCD camera

Image formation takes place in an electron-multiplying charge-coupled device (EMCCD). The EMCCD camera's (iXon Ultra 888, Andor Technology Ltd, Belfast, UK) chip has an edge length of $13.3\,\mathrm{mm}$. It consists of an array of 1024x1024 pixels, with a pixel edge length of $13\,\mu\mathrm{m}$. Each pixel is a capacitor, that is able to store a number of photoelectrons, proportional to the fluorescence intensity hitting the capacitor's area.
Under low-light conditions [1], the EMCCD camera's EM-gain register multiplies the stored number of e^- per pixel, before reaching the chip's output amplifier, where the read noise is introduced. In this setup, the read noise is, without the application of the EM-gain, $12e^-$ per pixel (according to the manufacturer[2]). By multiplying the number of photoelectrons before read out, the impact of the introduced read noise component per pixel becomes negligible, which can lead to an improved image quality. More details on the EM-gain will be given in chapter 6, in the context of the parameter optimization for the reliable imaging of single fluorophores on the surface.

The software (Andor Solis) of the EMCCD camera also controls the external shutter (Uniblitz, Vincent Associates, New York, USA) in the excitation light path.

Taking into account the setup's total magnification of 160, the edge length of the recorded square section of the objective's field of view is given by

$$l_{edgelength} = \frac{length_{chip}}{Magnification_{tot}} = \frac{13.3mm}{160} = 83.1\mu m. \tag{4.3}$$

The camera's chip records a square area with an edge length of $83.1\mu\mathrm{m}$, each pixel representing an area of $81.2\,\mathrm{nm} \times 81.2\,\mathrm{nm}$.

4.1.4 Nyquist criterion

The recording of the emitted signal onto the camera chip involves the division of an analog image into discrete picture elements (the pixels). This conversion process is the sampling of the image. To fully benefit from the system's resolving performance, the chip's pixel size (or the sampling density) must match the microscope's resolving performance:
The signal recreation of two diffraction-limited signals still resolvable by the microscope requires a sampling density high enough to display the separation. In other words, the arrangement of the pixels must be close enough, so that in between the signal pixels, there is at least one pixel with a dimmer intensity making the separation visible.
In the field of digital processing, the theorem of Shannon-Nyquist states that in order to reconstruct a (sinusoidal) signal faithfully, the sampling rate (or frequency) must be at least double the highest frequency component of the original signal in order to not lose information during its reconstruction [57, 58]. In the context of imaging, the signal to be reconstructed is of spatial nature and the sampling rate relates to the pixel size of the camera chip. The pixel edge length must not be larger than half of the microscope's resolution limit. Approximating the microscope's resolution limit by the Gaussian fit's FWHM (equation 2.16) leads to a critical sampling distance,

[1] The read noise of the camera (see section 4.1.5) is the limiting factor to sensitivity [47].
[2] chip read out rate of $1\,\mathrm{MHz}$, application of the camera's EM-amplifier

given by

$$\Delta_x \approx \frac{FWHM}{2}. \tag{4.4}$$

At a sampling rate lower than FWHM/2, information of the initial image will be lost, the image is 'undersampled'. At a sampling rate much higher than the critical sampling, the initial image will be reconstructed faithfully, at the expense of creating an unnecessary amount of data volume, without necessarily a benefit to the image quality.
In this setup, at the GFP emerald's emission wavelength of $509\,\mathrm{nm}$ (the fluorophore with the shortest emission wavelength used in the presented measurements) and the objective's NA of 1.49, the critical sampling distance is reached at $87\,\mathrm{nm}$, according to equation 4.4. A pixel edge length representing $81.2\,\mathrm{nm}$ (as determined in section 4.1.3) complies with the Nyquist criterion.

4.1.5 Signal-to-noise-ratio and noise sources

Abstracted from [59, 60].
Imaging requires the discrimination of the molecule's signal from the signal's inherent fluctuation, that is collected or introduced by the camera during image acquisition. The signal's fluctuation is the so-called noise. On single-molecule level, noise can impose a major limitation: Since noise and the signal itself are likely to be of the same order of magnitude, it may become difficult or impossible to discriminate between them. If a discrimination is not possible, the molecule's signal becomes invisible. This section introduces the different noise sources and how they affect image quality.

During image acquisition, a pixel (photodiode) of the camera chip is hit by a number of photons N_γ. The number of photons each photo-diode converts to photo-electrons

$$N_{e^-} = E_{det} \cdot N_\gamma \tag{4.5}$$

depends on the detection efficiency of the camera E_{det}. For an ideal detector, E_{det} would be 1: one arriving photon would generate one photo-electron. Real detectors don't reach the value of 1, due to the (gate electrode) structure of the chip and the wavelength-dependency of the photodiode's performance to absorb photons. The camera's E_{det} is wavelength dependent. In this setup, E_{det} exceeds 90% within the spectral range of interest (see figure 4.4 on page 28).

The intensity fluctuation or noise σ is the result of the particle nature of light itself and detector physics.

The contribution to σ from the light itself is shot noise σ_{sn}: Because of the particle nature of photons, light arrives in quantized amounts at the detector chip. The random arrival of photons at the detector introduces an inherent stochastic variation of N_γ within the illumination time. Although the precise moment of arrival cannot be predicted, its probability of arrival time within the illumination time can be described by a Poisson distribution, with σ_{sn} being its standard deviation

$$\sigma_{sn} = \sqrt{N_{e^-}}. \tag{4.6}$$

While N_{e^-} increases with the fluorescence signal, the shot noise σ_{sn} increases only by the square root of the number of collected photons $\sqrt{N_{e^-}}$, showing the importance to collect as many photons as possible.
Other sources of noise are introduced during data processing:
In low-light conditions, the limiting factor for imaging is imposed by the read noise σ_{rn} of the camera: Read noise happens as a consequence of the chip being unable to convert one photon into one photo-electron one by one. It becomes more important with short exposure times (high read out rates of the chip) and at low photon levels.

Dark noise or thermal noise σ_{dn} is the statistical variation from pixel to pixel originating from thermally generated electrons. σ_{dn} depends on the exposure time and temperature of the chip. With a CCD chip cooled down to a temperature of $-80\,°\mathrm{C}$ and short exposure times, this component becomes negligible.
The different types of noise add up to the overall noise

$$\sigma = \sqrt{\sigma_{sn}^2 + \sigma_{dn}^2 + \sigma_{rn}^2} \approx \sqrt{\sigma_{sn}^2 + \sigma_{rn}^2} \tag{4.7}$$

Ultimately, image quality depends on the achieved signal-to-noise ratio (SNR). It is defined as the ratio of the generated photoelectrons N_{e^-} to the overall noise

$$SNR = \frac{N_{e^-}}{\sigma}. \tag{4.8}$$

The SNR gives a measure for the quality of the signal and determines the optical performance of the system. A signal with a SNR ≤ 1 is indiscernible from the noise and hence, invisible. The higher the SNR of a single molecule's signal, the better the image quality and the easier a signal is identified. During data analysis, the SNR must be high enough, that the analysis routine (chapter 5) can reliably identify and fit a fluorophore's intensity distribution.

While the SNR depends on a fluorophore's inherent characteristics like brightness and photostability, as well as on the imaging conditions, it is hard to name a typical SNR value for single fluorophores, yet the values, found in the literature, were mostly below 10 [61–63]. Figure 4.3 shows two $4\,\mu\mathrm{m} \times 4\,\mu\mathrm{m}$ cutout areas on the left with a fluorescent microsphere (introduced in chapter 4) on top and a single fluorophore (Alexa647-NHS, chapter 5) below. The corresponding intensity profiles are plotted on the right. The difference in emission intensity is evident and the reason why a good SNR is important becomes apparent: A single fluorophore's intensity distribution must 'stand out' from the noise to be discernible.

The goal of the preliminary measurements (chapter 6) was to determine imaging parameters, that allow the reliable imaging and identification of single fluorophores on the surface. Therefore, the effect of the imaging parameters on the SNR of single dyes, rather than their impact on a dye's signal intensity alone, will be reported.

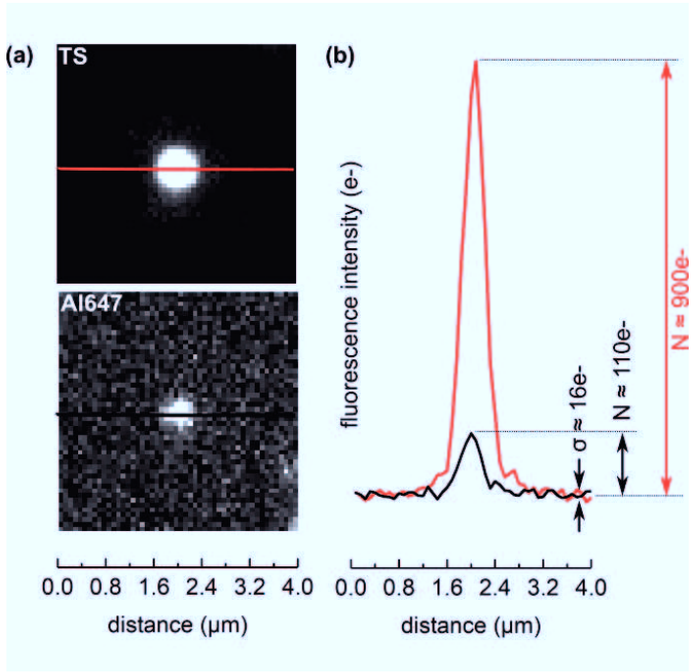

FIGURE 4.3: (a) $4\,\mu\mathrm{m} \times 4\,\mu\mathrm{m}$ area cutouts of a TS bead and a single Alexa647 dye. The comparison of the intensity profile plots (b) of the bead and the single dye show exemplarily the relation between the noise σ and the signal height of a single dye and a TS bead. Typically, the determined SNR are <10 for single dyes and >10 for TS beads.

4.1.6 Filter set spectra and the setup's transmission function

Dual-color experiments on single-molecule level need the separation of the sample's signal from any unwanted signal. The separation is done by appropriate filter combinations. In this setup, two filter sets were used:

1. the yellow/red dual-band set for the dye pair Cy3 and Cy5, consisting of the $532\mathrm{nm}/640\mathrm{nm}$ dual-band exc.filter, DM and em.filter (ZET532/640x, ZET532/640m-TRF and ZT532/640rpc-UF2, Chroma Technology Co., Vermont, USA).

2. the green/red dual-band set for the Alexa647/Alexa488 pair as well as Cy5/GFP emerald, consisting of the $488\mathrm{nm}/640\mathrm{nm}$ dual-band exc.filter, DM and em.filter (ZET488/640x, ZET488/640m-TRF and ZT488/640rpc-UF2, Chroma Technology Co., Vermont, USA).

Figure 4.4 shows the transmission spectra of both filter sets measured with a photospectrometer (UV-2401PC UV-VIS recording photospectrometer, Shimadzu Co., Japan). The transmission spectra of the objective and the quantum efficiency of the camera were provided by the manufacturers. In order to estimate the amount of fluorescence signal lost during image acquisition (after having entered the objective), the transmission function for the spectral ranges of interest was determined. It was assumed that the signal loss coming from the lenses and mirrors in the emission

path is negligible. The components taken into consideration were the transmission spectra of:

- the objective,
- the dual-band emission filter along with the dual-band dichroic mirror,
- the long-pass dichroic mirror of the image-splitter (plus the additional $655\,\mathrm{nm}$ long-pass filter in the red spectra) as well as,
- the quantum efficiency of the EMCCD camera.

The convolution of all the components, the overall transmission of fluorescence t_{tot} is given by

$$t_{tot}(\lambda_{em}) = t_{obj}(\lambda_{em}) * t_{dbDM}(\lambda_{em}) * t_{dbEM}(\lambda_{em}) * t_{DMlp}(\lambda_{em}) * E_{det}(\lambda_{em}). \quad (4.9)$$

The fraction of transmitted signal in the three different spectral bands (along with the different components) is illustrated as the colored areas in figure 4.4. It can be seen that, while the transmission of the filters are high (above 90%), a more noticeable fraction of the signal is lost, due to the quantum efficiency of the camera in the red spectra and the transmission spectra of the objective. The convoluted transmission spectra show that, between a quarter and a third of the fluorescence entering the objective is lost.

The convolution of the transmission function with the emission spectra of the fluorophores, employed in this work (chapter 6), are illustrated in figure A.3 on page 106.

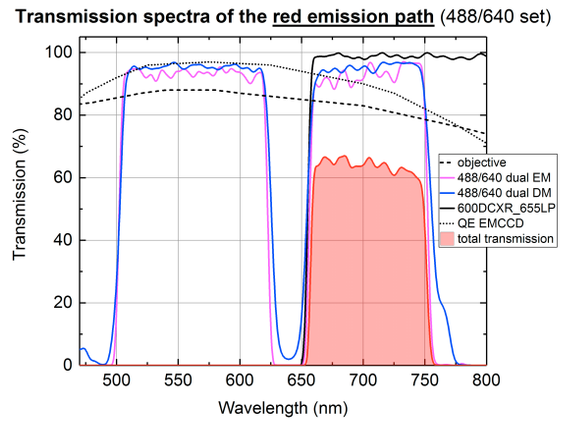

FIGURE 4.4: The transmission spectra of all the components in the emission path along with the quantum efficiency of the camera for the three spectral ranges. Their convolution, the total transmitted signal, is represented by the colored areas.

4.2 Getting started with imaging

4.2.1 Excitation intensity at the cover slide surface

On the way to the cover slide surface, the excitation power decreases, as the laser beam passes the optical elements. While the dielectric mirrors and appropriately selected optical filters have a negligible or minor impact on the excitation power, mainly clipping elements, like the pinhole, decrease the excitation power. The fractions of power, that reach the surface, were measured for the three excitation wavelengths and will be reported in the following.

For a stable output, the lasers had been warmed up for one hour. The power measurements were done with a power meter (FieldMate, Coherent, Califonia, USA) with a high-sensitivity optical sensor (OP-2 VIS). The power ranges of the three lasers (λ_{ex}= $488\mathrm{nm}$, $532\mathrm{nm}$ and $639\mathrm{nm}$), were measured at the cover slide surface. A cleaned cover slide was fixed onto the stage, with immersion oil in between the objective and the cover slide, to simulate experimental conditions. The optical sensor was fixed just above the cover slide surface and positioned at the center of the objective's eye lens, making sure it measures the highest intensity. As the intensity distribution tends to open up with increasing distance from the surface, it was verified that the distance between the surface and the optical sensor is small enough, so that no excitation light is clipped by the sensor's round active area (of a diameter of $7.9\mathrm{mm}$). After warming up the lasers, the measurement was done by increasing the excitation power stepwise. The mean value of different power measurements was determined, taking into account the system accuracy of $\pm 6\%$ from the power meter (specified by the manufacturer). The set power vs. the measured power on top of the cover slide's surface is illustrated in figure 4.5.

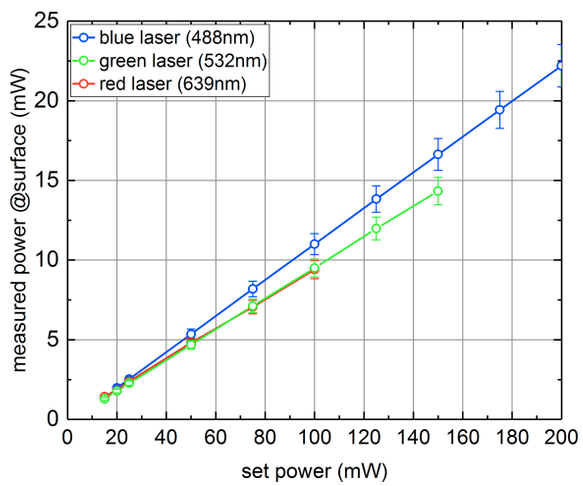

FIGURE 4.5: The set power vs. the measured power at the surface for the three lasers used in the setup.

Figure 4.5 shows the linear relation between the set power value and the measured value near the surface. By the way the excitation beam has reached the surface, its power has decreased by approximately 90%. The found values are in the mW-range, which is in agreement with the values found in the literature [64].

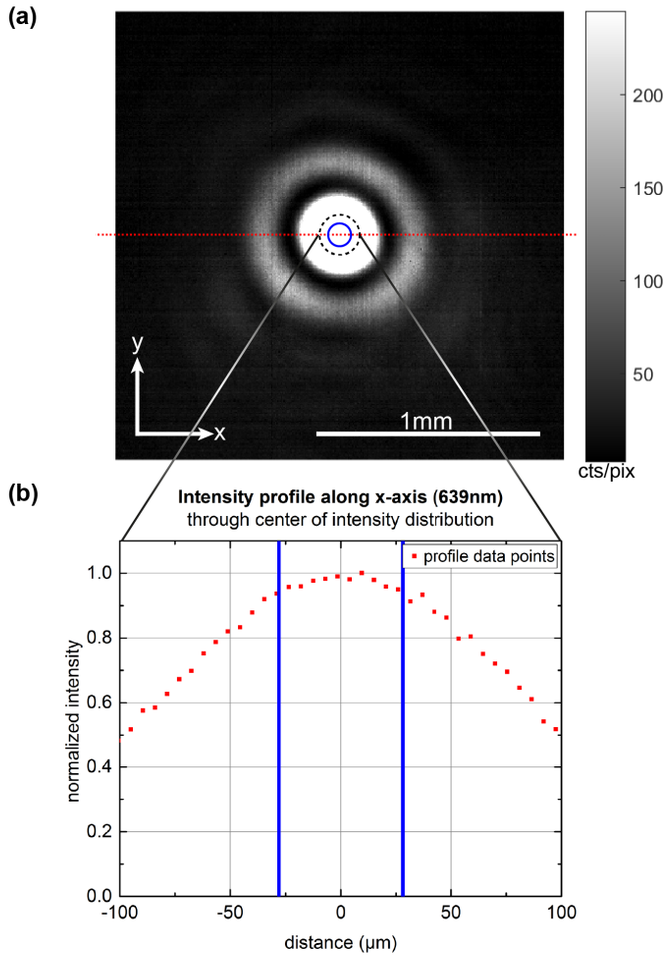

FIGURE 4.6: (a) A $2\,\mathrm{mm} \times 2\,\mathrm{mm}$ area of the red laser's intensity distribution less than $1\,\mathrm{mm}$ above the objective. The blue circle represents the central area of the distribution, where the power distribution is considered to be constant. (b) The excitation power profile across the center of the distribution (red dotted line in (a)), the blue bars mark the area, where the drop in power is not more than 5%

.

In the following step, the excitation power distribution within the imaged area, was measured. Due to diffraction (chapter 2), the excitation power distribution within the excited surface area is not homogeneous. Its variation, for each excitation color, within the imaged area was measured with a beam profiler (Beamage 3.0, gentec-eo, Canada). To do so, the beam profiler's photosensitive aperture was placed on top of the objective's front lens, separated by less than $0.5\,\mathrm{mm}$). To prevent soiling of the beamprofiler's photo-sensitive area, the excitation profile was measured without applying immersion-oil between the photo-sensitive area and the objective lens.

The measured excitation power distribution for the red laser is shown in figure 4.6 (a). Within the blue marked circular area (with a radius of approximately $30\,\mu\mathrm{m}$), the excitation intensity drops less than 5%, visible in the corresponding data profile along the x-axis through the center of the power distribution (red dotted line). This circular area, comprising the square central $40\,\mu\mathrm{m} \times 40\,\mu\mathrm{m}$ area, that will be imaged by the camera, was approximated to be constant.

The central lobe of the excitation power distribution (0th order Airy disk) contains 84% of the total measured power P_{tot}. The fraction of power contained within the blue circled area P_{center} could be related to P_{tot}, $P_{center}=(0.09 \pm 0.01)\cdot P_{tot}$. The excitation intensity J_{center} (within the blue circle with an area of $2.45 \times 10^{-5}\mathrm{cm}^2$) is then determined by the ratio

$$J_{center} = \frac{P_{center}(mW)}{2.45 \cdot 10^{-5}(cm^2)}.$$

The derived excitation intensities for the three lasers, at different powers measured at the surface, are displayed in figure 4.7.

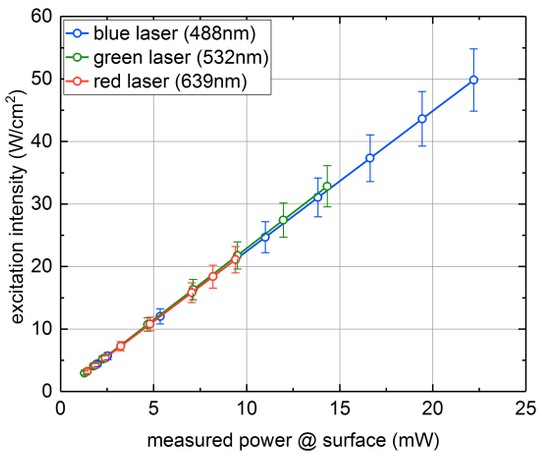

FIGURE 4.7: The intensities at the excitation center, derived from the excitation power profiles and the previous power measurements.

It can be seen that, in this setup, the excitation intensities range from approximately $5\mathrm{W/cm}^2$ to $50\mathrm{W/cm}^2$. Converted to a photon flux (with a photon energy

$E = \frac{h \cdot c}{\lambda_{ex}}$), the excitation intensity is on the order of $10^{19} \frac{photons}{cm^2 s}$ for the three excitation wavelengths λ_{ex}. The converted intensity values are found in table A.1 on page 107.

This intensity estimation does not claim to be quantitative, since due to the omitted cover slide and immersion oil, the exact imaging conditions cannot be replicated. Furthermore, a slight variation in the excitation power may occur during realignment of the microscope setup. Yet, the determined values for the excitation intensities were in good agreement with the later measured fluorescence output of the single fluorophores, confirming the obtained results from the method A.2 on page 107.

4.2.2 Alignment check with fluorescent beads

The microscope setup must be aligned in order to allow the reliable imaging of single molecules. In a first approach, the excitation beams are guided through the objective, they should pass the objective centrally, as well as perpendicularly. Projected onto a bull's eye under the ceiling, their diffraction patterns should overlap in the best possible way. The next alignment steps are done directly with the camera and TS beads. The employed TS beads are sub-resolution-sized microspheres of $0.1\,\mu\mathrm{m}$ diameter. They are stained throughout with four different dyes, displaying four separated excitation/emission peaks: $360/430\mathrm{nm}$ (blue), $505/515\mathrm{nm}$ (green), $560/580\mathrm{nm}$ (yellow) and $660/680\mathrm{nm}$ (dark red). TS beads display a high SNR and negligible photobleaching, which is ideal for the alignment of the setup.
Cover slides stained with TS beads (chapter 3) are employed to check the homogenous illumination of the camera's FOV, by comparing visually the beads' fluorescence intensity distribution in the center with beads' intensities at the edge of the imaged area. If the center of the excitation intensity is not meeting the center of the FOV area, this is indicated by the heterogeneous emission intensity of the beads. In the case of two-color measurements, TS bead slides are used to check the alignment of the image splitter, a crucial step for two-color imaging, that was done before every colocalization measurement.

4.2.3 Resolving performance of the setup

Displaying a high SNR and insignificant photo bleaching, a TS bead slide was employed to determine the setup's resolving power within the three relevant spectral ranges (displayed in figure A.2 on page 105). In order to separate the emission spectra of the TS beads, additional emission filters of the following central wavelength λ_{center} and bandwidth were used:
1. λ_{center} of $535\,\mathrm{nm}$ and a bandwidth of $45\,\mathrm{nm}$ in the green spectra (XF3084 535AF45, Omega Optical, Brattleboro, Vermont, USA),
3. λ_{center} of $575\,\mathrm{nm}$ and a bandwidth of $50\,\mathrm{nm}$ in the yellow spectra (HQ575/50, Chroma Optics, Burlington, Vermont, USA) and
2. λ_{center} of $670\,\mathrm{nm}$ and a bandwidth of $40\,\mathrm{nm}$ in the red spectra (XF3030 670DF40, Omega Optical, Brattleboro, Vermont, USA).

The resolving power of the setup is the highest at the objective's focal plane. By performing a stack measurement along the optical axis, the change in the intensity distribution of the PSF can be monitored. The objective's z-position was varied in steps of $0.1\,\mu\mathrm{m}$, the focal plane is located between the two z-positions, that result

in the narrowest PSF. In practice, the setup's obtainable resolution was the lowest determined average $FWHM_{x,y}$ from the z-stack measurement in each of the three spectral ranges. An example, showing a cutout of a single bead taken from the measurement, is shown in figure 4.8.

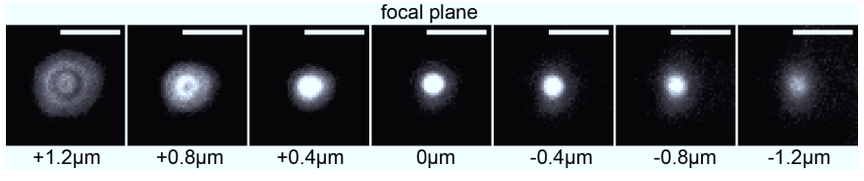

FIGURE 4.8: Shown is a z-stack of an imaged TS bead around the focal plane. At the focal plane, the imaged beads show the narrowest intensity distribution (Airy disk), the fitted Gaussian will have the smallest width $\sigma_{x,y}$. As a result of the rays' different pathways above and below the focal plane, the observed diffraction patterns are not symmetrical at inter- and extrafocal distance of the focal plane [65]. The scale bar length is $2\mu\mathrm{m}$.

During a z-stack, a single area was imaged, ensuring, that the focus position does not drift. The recorded intensity distributions of the TS beads were fitted with a two-dimensional Gaussian to determine their width $\sigma_{x,y}$. According to section 2.2, the resolving power (the $FWHM_{x,y}$ of the TS intensity distribution) and the width $\sigma_{x,y}$ relate in the following way,

$$FWHM_{x,y} = \sigma_{x,y} \cdot 2\sqrt{2ln(2)}. \tag{4.10}$$

$FWHM_x$ and $FWHM_y$ from the two-dimensional Gaussian fits, displayed the same behavior and very similar values. Therefore, only the determined values for $FWHM_x$ will be shown in the following.
In a first measurement, the impact of the objective's correction collar (cc) setting on the setup's resolution power was tested. A set of z-stack series was performed, each stack with a different cc-position, ranging from 0.16 to $0.19\mathrm{mm}$. A mismatch in the refractive indices will lead to spherical aberration, that will reduce the resolution performance of the setup. The refractive indices of both the cover slide and the immersion oil are matching, which should eliminate spherical aberration for an observed specimen touching the cover slide surface. Figure 4.9 displays the $FWHM_x$ values for each z- and cc-position tested, derived from the fit widths σ_x (with $r^2 \geq 0.9$):
While a change of the correction collar position involves a drift in the focus position along the optical axis, the average achievable $FWHM_x$-minimum for beads is practically not affected by the tested cc-positions, the resolution minimum remains nearly constant throughout the tested cc-settings. Since the refractive index of both the cover slide and the immersion oil match, no refraction of the light waves occur and the full NA of the objective can be used, resulting in the maximum resolution [66]. Furthermore, it could be concluded that, the measurement procedure's illumination did not lead to a change in the (temperature dependent) refractive index of the employed immersion oil (nominal refractive index of 1.51). By employing beads with a diameter of $100\mathrm{nm}$, the measured $FWHM_x$ in the green is $330 \pm 11\mathrm{nm}$. The correction collar was set to $0.17\,\mathrm{mm}$ for all the following measurements.

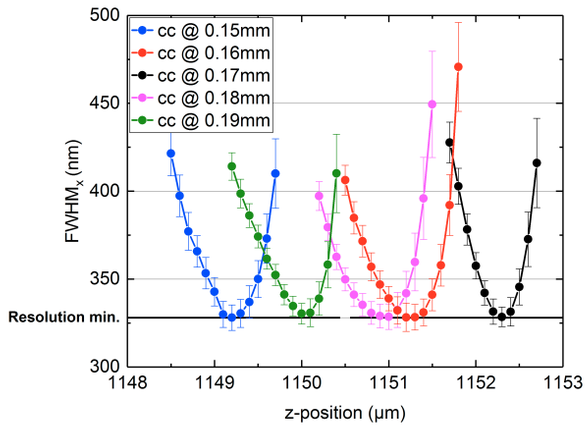

FIGURE 4.9: Impact of the objective's correction collar on the $FWHM_x$ of TS beads on the surface

In a second step, the wavelength-dependency of the resolving power was tested. While the measurement procedure was the same as in the previous step, this time, the measurements were performed in the green, yellow and red spectra (at the cc-position of $0.17\mathrm{mm}$). Figure 4.10 combines the trend of the average $FWHM_x$ versus the distance from the focal plane in the three spectral ranges of interest. The corresponding table displays again the measured $FWHM_x$ versus the theoretically expected $FWHM_x$. Expectedly, the $FWHM_x$ decreases with the emission wavelength, the smallest emission wavelength results in the highest resolution.
Within a z-range of $\sim 200\mathrm{nm}$, the $FWHM_x$ value is nearly constant. Comparing the measured $FWHM_x$ value with the theoretically expected value reveals a discrepancy: In a theoretical, optically perfect system, the resolution is determined only by the numerical aperture of the objective and the light's wavelength. In a real system however, the theoretical values cannot be achieved for several reasons: deteriorating effects coming from aberration, pixelation of the analog signal and the recorded noise level in comparison to the signal height [67].
Beyond that, the physical size of the TS beads needs to be considered. With a diameter of approximately $100\mathrm{nm}$, their size may not be considered true point-sources anymore, compared to the theoretically obtainable PSF. In fact, the recorded intensity distribution corresponds to the convolution of the microscope's PSF with the physical dimensions of the bead. To determine the system's PSF requires either a deconvolution of the recorded bead image (as proposed in the literature [68, 69]), or the imaging of single dyes, at the conditions that their SNR is high enough and that they are photo-stable enough to perform the measurement (as proposed in [70]).

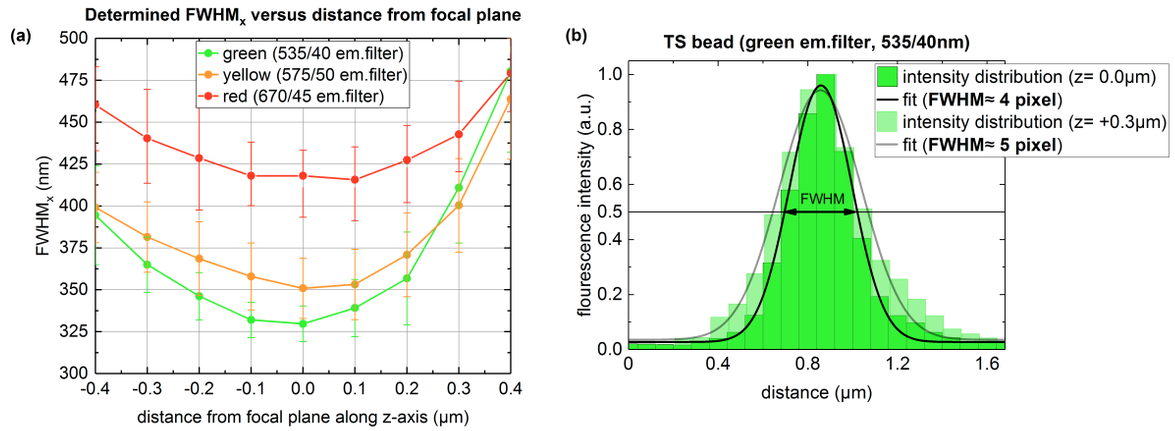

spec. range	FWHM$_{x,theo}$ (nm)	FWHM$_{x,meas}$ (nm)
green	183	330±11
yellow	197	351±20
red	229	413±15

FIGURE 4.10: The FWHM$_x$ determined from a z-stack of images in the three spectral ranges (a). The error bars correspond to the RMS of the fitted signals. For illustration, representative profile plots along the x-axis of a TS bead are shown, imaged (in the green channel) at the focal plane and $0.3\,\mu\mathrm{m}$ above. In focus, a TS bead displays an FWHM of approximately 4 pixel in the green spectra (b). The table lists the expected FWHM$_{x,theo}$ and the measured FWHM$_{x,meas}$ in the three spectral ranges. FWHM$_{x,theo}$ was calculated according to equation 2.16, taking into account the central wavelength of the auxiliary emission filters ($535\,\mathrm{nm}$, $575\,\mathrm{nm}$, $670\,\mathrm{nm}$, see figure A.2 on page 105) and the objective's NA of 1.49.

After having optimized the imaging parameters for the single dyes of interest to this work (presented in chapter 6), the measurements to determine the resolution performance of the setup were repeated with single dyes, embedded in polymer film (Alexa488, Cy3 and Cy5). The major constraints are in this case the lower SNR, compared to beads, as well as the limited observation time before bleaching.
Knowing from the bead measurements, that the FWHM is relatively constant near the focal plane, a high number of areas 'in-focus' were imaged. Again, the signals from each image were fitted with a two-dimensional Gauss. The (selected) peak fits with $r^2 \geq 0.9$ were averaged, the derived FWHM$_x$ with the corresponding statistical variation from 150 peaks are listed in figure 4.11.

Displayed are the measured FWHM$_x$ of the single dyes and the theoretically expected values for comparison. Still being larger than the theoretical values, the found values for the single molecules are in average approximately 15-25% smaller than for the beads. Since the single dyes' size ($\sim 1\mathrm{nm}$) is much smaller than the beads', the physical size of the dyes can be considered a point-source, with a negligible impact on the setup's PSF. The determined FWHM$_x$ in the green spectra is in good agreement with the values found in the literature of approximately $250\,\mathrm{nm}$ [71–73], allowing the conclusion, that the setup is well aligned.

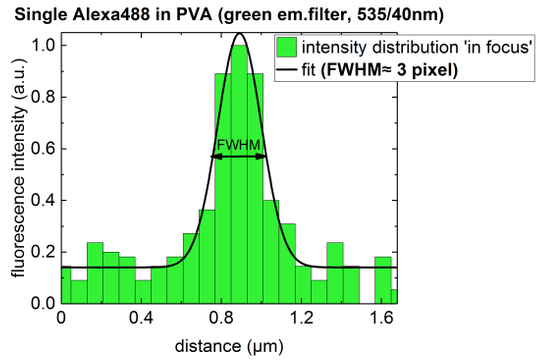

spec. range	dye	$FWHM_{x,theo}$(nm)	$FWHM_{x,meas}$(nm)
green	Alexa488	183	261±17
yellow	Cy3	197	294±22
red	Cy5	229	311±20

FIGURE 4.11: The determined $FWHM_x$ derived from the imaging parameter optimization (chapter 6) in the three spectral ranges, together with a representative profile plot of a single Alexa488 dye in the green spectra and the marked $FWHM_x$ of approximately 3 pixel.

4.2.4 Chromatic aberration

A colocalization experiment is the simultaneous imaging of an area in two color channels. By superimposing the recorded two channel images, assuring the adequate overlap of both color channels, the fraction of colocalized signals can be determined. As a result of chromatic aberration, an effect resulting from dispersion, light waves of different color, that pass through a lens, do not focus on the same focal plane (along z), or off-axis, not on the same lateral position (along x-y). These two forms of aberration are the axial chromatic aberration and lateral chromatic aberration [65].

Considering data analysis, the impact of the axial focal shift is negligible, though the lateral chromatic aberration leads to a relative position shift, between the fluorescence signals in the image plane, as illustrated in figure 4.12(a). Figure (b) shows the uncorrected merge of the red and green channel of an $80\,\mu\mathrm{m} \times 40\,\mu\mathrm{m}$ area, on the example of a TS bead slide: While in the center of the image, the overlap of both channels is assured (as can be seen by the white spots), towards the edges, the shift becomes obvious. The green signal and corresponding red signal of the same spot are clearly separated (by more than $2\,\mu\mathrm{m}$ or 25 pixels).
The relative shift is essentially proportional to a signal's distance from the image center bottom and will be taken into account by the analysis routine (chapter 5). For the ease of data analysis, only the central $40\,\mu\mathrm{m} \times 40\,\mu\mathrm{m}$ area was taken into consideration, as marked by the white dashed box.

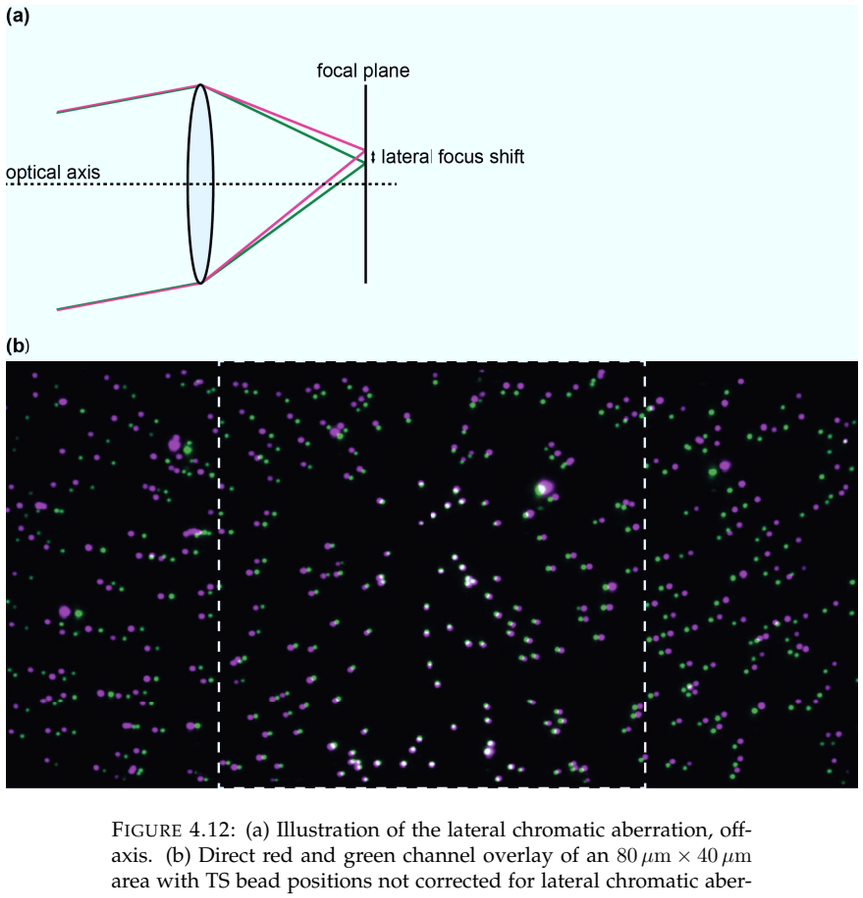

FIGURE 4.12: (a) Illustration of the lateral chromatic aberration, off-axis. (b) Direct red and green channel overlay of an $80\,\mu\mathrm{m} \times 40\,\mu\mathrm{m}$ area with TS bead positions not corrected for lateral chromatic aberration.

4.2.5 Measurements in solution with a confocal microscope

The major part of the presented measurements were performed with the WFM. Especially in the case of colocalization measurements, additional measurements in solution were performed in parallel, to check the sample's condition and to compare the obtained results from the surface measurements from the WFM with a complementary method. The measurements were done with a confocal microscope (Microtime 200 from Picoquant, Berlin Germany). The confocal microscope's characteristics and its applications, relevant to this work, will be outlined in the following.

In contrast to the WFM, the excitation light is focused into a diffraction-limited spot, the confocal volume. The confocal volume is diffraction-limited in size (hence dependent on the excitation wavelength) and of an ellipsoidal shape. Since the excitation light is focused, the excitation intensities are in general much higher than in a WFM (by several orders of magnitude) and allow a time-resolution down to ns during a FCS measurement. Fluorophores, diffusing through the confocal volume, are exposed to the highest excitation intensity and only the emitted fluorescence from within the confocal volume is collected: A pinhole ($50\,\mu\mathrm{m}$), positioned at confocal

distance from the tube lens, blocks any fluorescence signal, not coming from the within the confocal volume. The fluorescence signal is then split by a dichroic mirror, before it passes the appropriate emission filters and is recorded by avalanche photo-diodes.
A molecule diffusing through the confocal volume results in an intensity burst in the fluorescence intensity time-trace F(t). In a fluorescence correlated spectroscopy measurement (FCS), F(t) will be correlated to F(t+τ), τ corresponding to the correlation time. The auto-correlation curve G(τ) is given by

$$G(\tau) = \frac{< \delta F(t) \cdot \delta F(t+\tau) >}{< F(t) >^2}. \tag{4.11}$$

In its simplest form (purely diffusive model) [74, 75], the auto-correlation function is given by

$$G(\tau) = \frac{1}{N} \cdot (1 + \frac{\tau}{\tau_{dt}})^{-1} \cdot (1 + \frac{\tau}{k^2 \tau_{dt}})^{-1/2}, \tag{4.12}$$

where N is the number of molecules present in the focal volume, τ_{dt} corresponds to their average dwell time within the focal volume and k is the ellipticity of the focal volume, defined as the ratio of the major axis and the minor axis $\omega = \frac{z_0}{\omega_0}$. G($\tau$) was fitted to extract the sample's characteristic diffusion coefficient D

$$D = \frac{\omega_0^2}{4\tau_{dt}}. \tag{4.13}$$

The characteristic diffusion coefficient D allows to conclude about the sample's condition considering aggregates. In this work, FCS measurements were mainly done with ribosome- and GFPem samples in the context of a CFPS study (chapter 8). A representative example of an FCS curve for Cy5-labeled ribosomes and GFPem is illustrated in figure 4.13.
Furthermore, two-color coincidence detection measurements (TCCD) were done with a highly diluted two-color sample (less than 0.01 molecule in the confocal volume at one time). During a TCCD measurement, pulsed interleaved excitation is used to excite the sample. Depending on the time-window between the recorded intensity bursts in the two channels (inter-photon distance), it is possible to determine the fraction of two-colored molecules within the sample [76]. In our case for example, TCCD measurements were done to determine the fraction of red-labeled ribosomes with a bound green fluorescent protein (GFPem).

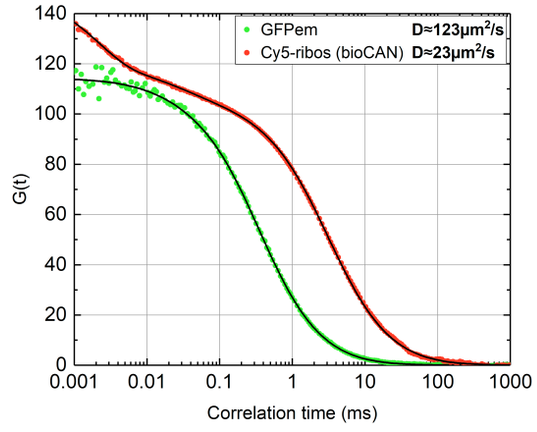

FIGURE 4.13: The auto-correlation data points from Cy5-labeled ribosomes and GFPem measured in solution with the corresponding fits (pure diffusion model for GFPem and conformational change for the Cy5-labeled ribosomes). The determined characteristic diffusion coefficients allow to make a statement about the sample condition considering aggregates.

Chapter 5

Data analysis

5.1 Introduction

The data set, recorded with the WFM, comprised in general a high number of 16-bit gray scale images. To retrieve the desired information from the images, each image was processed by an analysis routine [1]. Depending on the goal of the measurement, the routine was employed to

- determine the resolving power of the setup, by determining the width of the intensity distributions of the sub-diffraction sized TS beads and single fluorophores, imaged near the focal plane (chapter 4),
- to point out the imaging parameters, that resulted in the highest SNR for the different single fluorphores (chapter 6),
- evaluate the impact of the photoprotection systems on the photostability of single fluorophores, as well as to evaluate the success of the surface functionalization, by counting the number of fluorescence peaks per imaged area (per frame) (chapters 6 and 7),
- quantify different populations within a sample in the context of a dual-color measurement, by determining the fraction of colocalized signals (chapter 8).

The principal steps of the analysis routine will be outlined in the following.

5.2 The recorded image

As mentioned in chapter 4, the raw image consisted of a 1024x1024 count value array, representing the two color channels of a $80\,\mu\mathrm{m} \times 40\,\mu\mathrm{m}$ area, that are projected side by side. To limit the shifting effects of chromatic aberration, only the central section of the image, a 512x1024 count value array, was processed by the routine. Each region (512x512 pixel) represents an area of $40\,\mu\mathrm{m} \times 40\,\mu\mathrm{m}$. An example of a TS bead slide area is displayed in figure 5.1.

[1] provided by Dr. Tina Züchner from ICS-5: Molecular Biophysics, Forschungszentrum Jülich

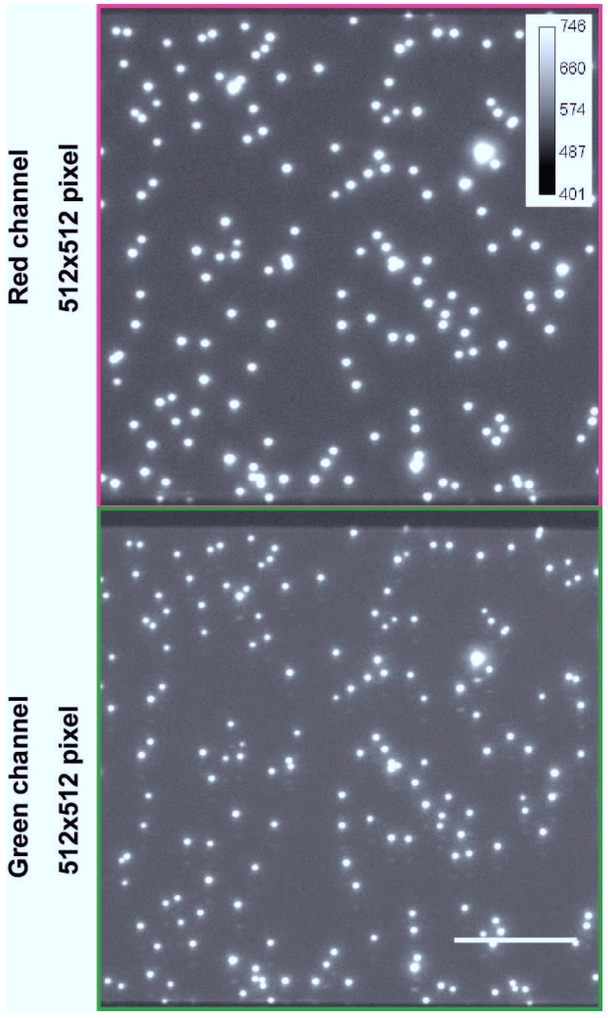

FIGURE 5.1: The two color channels of the central $40\,\mu\mathrm{m} \times 40\,\mu\mathrm{m}$ section of a TS bead image, displaying in each color approximately 120 TS signal peaks (scale bar $10\,\mu\mathrm{m}$).

5.3 The analysis routine

In most cases, the relevant information came from the results of the Gaussian fit, that was applied to each identified fluorescence peak within the images. The fit results for each fluorescence peak included for example

- the width of the intensity distribution,
- the SNR and the integrated intensity, as well as

- the number of colocalized signals in the case of a dual-color measurement, based on the center coordinates of the fit in both channels.

The routine's processing steps, necessary for the identification of the imaged fluorescence peaks and the fitting of their intensity distribution, will be outlined in the following.

1. Determination of the background value and standard deviation

   In a first step, the background and noise values BG and σ of the selected channel will be determined. BG and σ are necessary parameters to identify the fluorescence peaks in each channel.
   To determine BG and σ, the routine generates a histogram from the area's pixel values, that will be fitted by a two-component Gaussian. The determined mean of the Gaussian component with the corresponding highest occurrence, is considered the BG of the image (illustrated in figure 5.2).
   The noise σ was defined as the standard deviation of all the pixels below a threshold factor f set by the user.

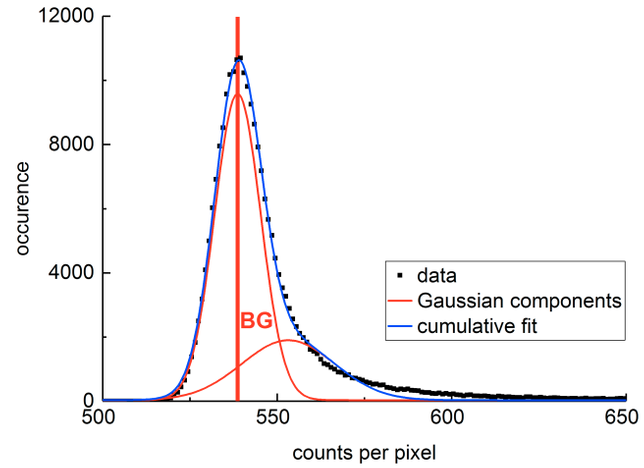

FIGURE 5.2: Histogram generated from the image's pixel count values displayed in figure 5.1, fitted with a two-component Gaussian. The marked center of the Gaussian is determined as the BG value of the selected area.

2. Identifying the potential peaks

   Having determined BG and σ, the script identifies the image peaks with a signal height above the set threshold factor f, according to

$$S \geq f \cdot \sigma + BG. \tag{5.1}$$

While for TS bead slides, f was set to 10, f ranged from 2-3 for single molecules (compare with figure 4.3 on page 26). Figure 5.3(a) shows a profile plot, taken from the bead slide image in (b). Single pixels, large connected areas with pixel intensities above the threshold, as well as peaks too close to the border of the area are discarded at this point.

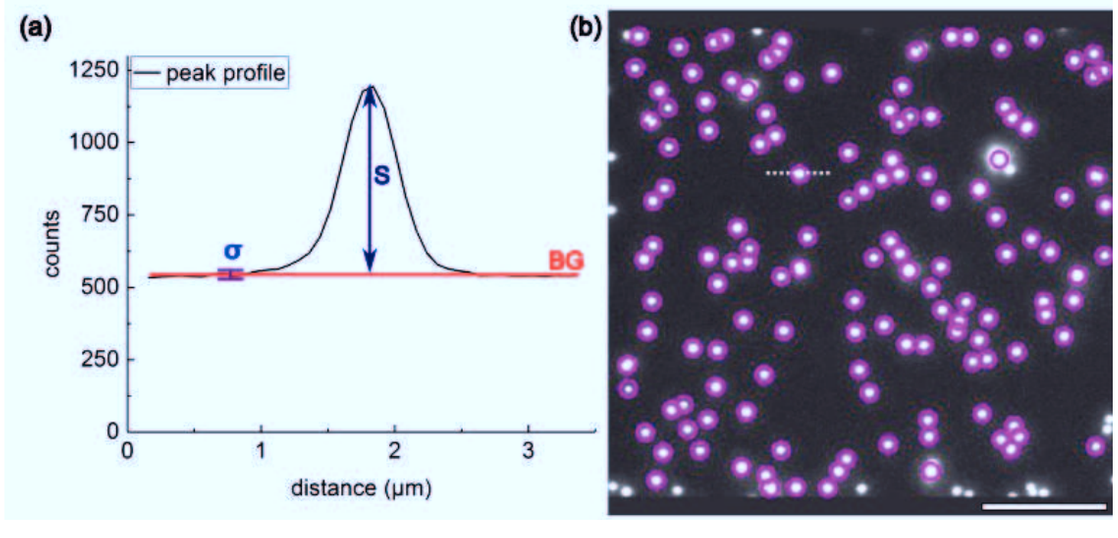

FIGURE 5.3: (a) A profile plot of a TS bead, with the marked signal height S, determined background BG and noise σ. (b) shows the figure with the identified potential peaks, marked by magenta circles (scale bar of $10\,\mu\mathrm{m}$).

3. Fitting potential peaks and quality check

The central step of the routine is the fitting of the identified peaks with a two-dimensional Gaussian.

Each potential peak from the previously generated list is cut out to be fitted. The size of the square cutout must be big enough to comprise the diffraction limited peak and partly the surrounding background, while not cutting into the neighboring peaks. In theory, 99.7% of a Gaussian distribution is comprised within a distance of 6 standard deviation σ. In practice, a 13x13 pixel array was cut out around each potential peak center, corresponding to an edge length of approximately $1\,\mu\mathrm{m}$. Figure 5.4(a) displays a TS profile plot, with the corresponding, marked cutout length around the peak center and the Gaussian fit.
The analysis routine employs the iterative Levenberg-Marquardt algorithm to fit a two-dimensional Gaussian to each cutout. The fit provides the mentioned

- center coordinates,
- amplitude S_{fit} as well as the background BG_{fit},
- standard deviation $\sigma_{x,y}$ along both axis,
- SNR_{fit} ($SNR = S_{fit}/\sigma$),

- and the integrated intensity.

The fit results pass a quality check, intended to remove fit results, that do not originate from a single peak (the fit results need to comply with boundaries, set by the user, considering for example the goodness of fit and the width of the Gaussian distribution). In figure 5.4(b), the accepted peaks are marked by the red circles, the rejected ones by the magenta circles.

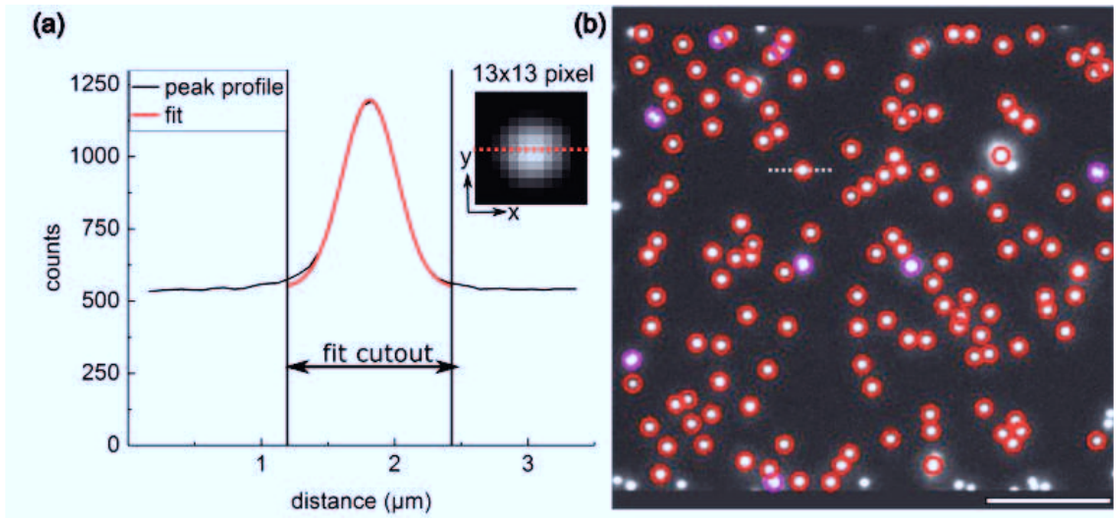

FIGURE 5.4: (a) A profile plot of a TS bead, together with the marked size of the cutout and the Gaussian fit (shown along the x-axis). (b) The figure generated by the routine (scale bar of $10\,\mu\mathrm{m}$) with the marked potential peaks and accepted peaks having passed the quality check (red circles).

4. Determination of a colocalization
   In the case of a colocalization experiment, both color channels are selected to be processed by the routine. The routine counts the fluorescence peaks as colocalized, if they have a corresponding partner in the other channel within a range of 3 pixel ($\equiv 240\,\mathrm{nm}$). As mentioned already, it was necessary to apply a correction for the lateral chromatic aberration (chapter 4) to the peak coordinates from one color with respect to the other color. The correction of the coordinates is essentially a radial shift, that is proportional to a peak center's distance from the bottom center of the image. After the correction, the routine determines iteratively for each peak in one channel the distance to the nearest peak from the other channel and counts the colocalizations. With a successful shift correction, the overlaid corrected peak coordinates from both colors should coincide, as illustrated in figure 5.5 (b).

   The literature proposes a cover slide with an etched regular grid pattern [77] to perform the correction of the aberration shift. In this work, the correction of the shift was tested with TS bead slides. Since TS beads are stained throughout with different fluorophores, theoretically 100% of the fluorescence peaks

should colocalize. Figure 5.5 shows, that the correction for the chromatic aberration is effective: the overlay of the corrected peak positions overlap. In general, the routine identifies over 95% of the TS bead peaks as colocalized. The remaining peaks have either not been accepted as single potential peak or didn't pass the quality check in one of the color channels. In the case of colocalization measurements (chapter 8), eventually missed colocalized peaks have been added to the automatically determined value manually, after a visual inspection of the image.

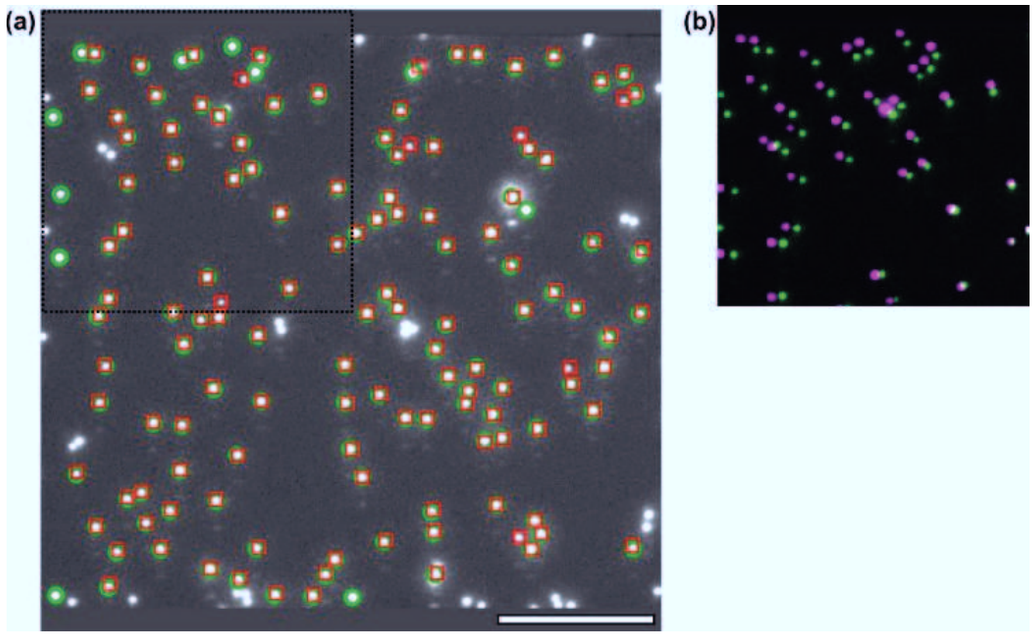

FIGURE 5.5: (a) The control figure of the green channel with the marked accepted peaks (green circles), shown with the overlaid corrected red peak positions (red squares). (b) A detail of the upper left section of the imaged area ($20\,\mu\mathrm{m} \times 20\,\mu\mathrm{m}$), composed of the direct overlay of both channels, shown to visualize the impact of the lateral chromatic aberration on the relative peak position (scale bar $10\,\mu\mathrm{m}$).

Chapter 6

Imaging on single-molecule level

6.1 Introduction

Biological processes can be investigated by methods of fluorescence microscopy only if the sample shows fluorescence. Either the sample is intrinsically fluorescent, or in case it is not fluorescent, or its fluorescence is not adequate to perform the desired experiment, it must be decorated (labeled) with fluorophores extrinsically [78].

Fluorophores are chemical compounds, that can be classified into the family of fluorescent proteins and non-protein organic fluorophores. Their chemical structure, containing aromatic hydrocarbon rings, as well as cyclic or planar molecules with π-bonds, is at the origin of fluorescence [79].
While the excitation wavelength and filter set of the microscope need to match the fluorophores' excitation/emission spectra, the key characteristics of a fluorophore in the context of imaging are its brightness and photostability.

An ideal fluorophore would display a high brightness with little or no fluctuations in fluorescence intensity (blinking) and negligible photobleaching. Unfortunately, a fluorophore's photophysical characteristics, like brightness and photostability, can impose a major constraint in the imaging and studying of biological phenomenons on single-molecule level [80].

This chapter introduces the employed fluorophores and presents the preliminary measurements, that were done to determine suitable parameter settings for the reliable imaging of single fluorophores on the surface.

6.2 Structure and photophysical properties of the employed fluorophores

6.2.1 Cy3 and Cy5

Cyanine dyes are among the oldest and most studied families of synthetic dyes. In the field of biological imaging, their popularity is due to two major factors:

They are commercially available as derivates and can be used as markers, that covalently bind to proteins and nucleic acids. In this work, Cy3 and Cy5 derivates with an NHS-ester reactive group were employed as labels.
Also, cyanine dyes can be excited with common lasers. Table 6.1 displays the peak absorption/emission wavelengths of Cy3 and Cy5, as well as the fluorophore's molecular absorption coefficient σ_{dye} and QY.

TABLE 6.1: The relevant photophysical values of Cy3 and Cy5 [81]

	λ_{ex}(nm)	λ_{em}(nm)	$\sigma_{dye}(cm^2)$	QY
Cy3	550	570	$5.74 \cdot 10^{-16}$	0.15
Cy5	649	666	$9.56 \cdot 10^{-16}$	0.27

Cyanine dyes have an elongated structure, containing polymethine bridges between two heterocyclic groups. In the case of Cy3 and Cy5, it is indole at both sides of the polymethine chain. The chemical structures of Cy3 and Cy5 are displayed in figure 6.1.Their excitation and emission wavelengths increase with the number of polymethine bridges, 3 and 5, for Cy3 and Cy5.

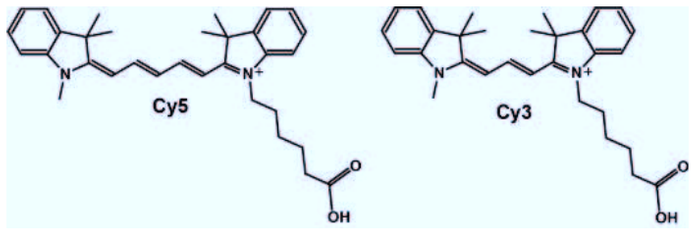

FIGURE 6.1: The chemical structure of Cy3 and Cy5 [82]

Like all organic fluorophores, cyanine dyes show photobleaching (introduced in chapter 2). In an excited state, a fluorophore's collision with electron donors or acceptors can yield radical ions (a consequence of oxidization or reduction). The radical ions react fast with molecular oxygen in the fluorophore's proximity, leading to a permanent loss of fluorescence.
The triplet state plays a key role in terms of photostability: Because of its longer lifetime compared to the singlet state, oxidation is likely to occur from the triplet state. Besides photobleaching, the transition to the triplet state has an impact on the fluorophore's SNR: With a triplet-lifetime ranging from milliseconds up to seconds, the molecule is in a dark state during that time. In the case of cyanine dyes, the triplet state formation has been reported to be related mechanically to the *cis-trans* photo-isomerization. The rate of isomerization depends on both, the viscosity of the environment and the length of the polymethine chain [83–85], with the planar *trans*-conformation being the non-fluorescent, or dark state.

6.2.2 Alexa488 and Alexa647

Alexa Fluor dyes are a family of dyes, that have been synthesized by sulfonation of other dyes. In this case, Alexa488 is derived from fluorescein and Alexa647 from Cy5. They have been chemically designed to display better photophysical properties, compared to the compounds they are derived from. Sulfonation makes the dyes hydrophilic and negatively charged [86].
Alexa647 displays a reduced *cis-trans* isomerization, reducing the transition to the (long-lived) dark state [87]. Also, the absorption and fluorescence emission spectra is reported to change very little when conjugated to proteins or nucleic acids, yielding in a higher fluorescence output at the same degree of labeling [86]. Alexa488 has similar excitation/emission spectra than fluorescein, but it is brighter, more photostable and less pH-sensitive [88, 89]. Figure 6.2 shows the chemical structure of both employed dyes, table 6.2 lists their photophysical properties.

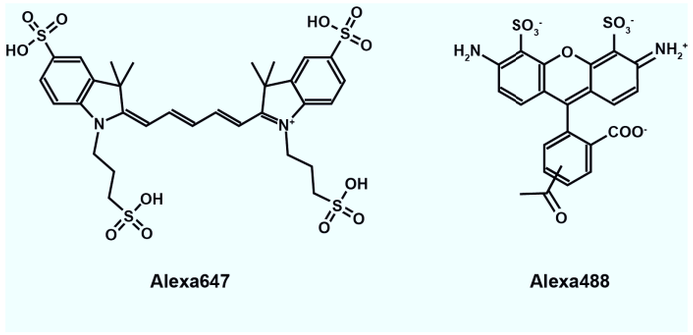

FIGURE 6.2: The chemical structure of the Alexa488 and Alexa647 [90].

TABLE 6.2: The relevant photophysical values of Alexa488 and Alexa647 [91, 92]

	λ_{ex}(nm)	λ_{em}(nm)	$\sigma_{dye}(cm^2)$	QY
Alexa488	490	525	$2.79 \cdot 10^{-16}$	0.92
Alexa647	650	665	$10.33 \cdot 10^{-16}$	0.33

6.2.3 GFP emerald

GFP is composed of 238 amino acids with a molecular weight of 26.9kDa. All GFP variants have the same beta barrel structure with the fluorophore itself running through the center, as depicted in figure 6.3. The beta barrel's dimensions are 42Å in length and 24Å in diameter, with alpha helices forming the caps and end of the barrel structure [12, 93].
The mutant used in this work is GFP emerald, chosen for its fast maturation time at $37°\text{C}$, good brightness and improved photostability over wild-type GFP

[94]. The main properties are given in table 6.3.

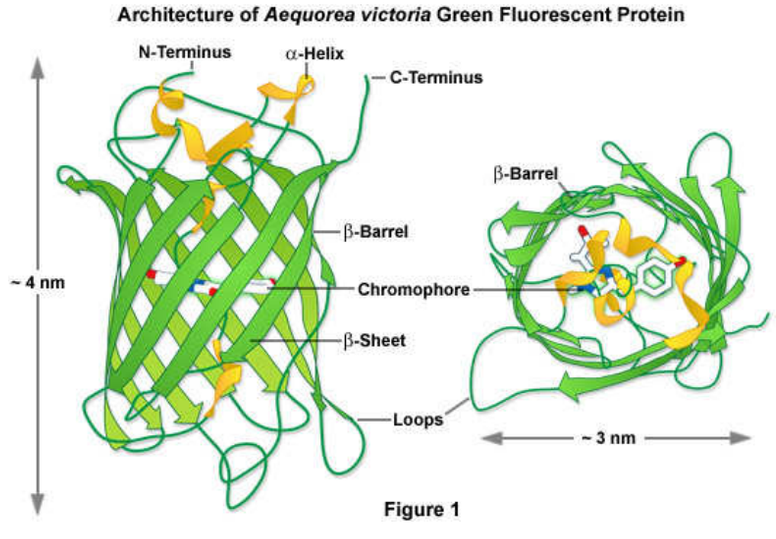

FIGURE 6.3: GFP architecture with the fluorophore shielded by the β-barrel [12].

TABLE 6.3: The photophysical properties of GFP emerald [94].

	λ_{ex}(nm)	λ_{em}(nm)	$\sigma_{dye}(cm^2)$	QY
GFPem	487	509	$2.20 \cdot 10^{-16}$	0.68

6.3 Parameter optimization for the imaging of single fluorophores

6.3.1 Observing single fluorophores on the surface

As a preface to the systematic measurements, the general characteristics of single fluorophores, imaged on the surface will be specified.

In general, single fluorophores of the same type display a similar behavior, considering their brightness and observation time. Figure 6.4 illustrates the characteristics, that allow the identification of a single molecule, imaged on the surface. In (a), the fluorescence signal of single Cy5, imaged at the focal plane, is shown. If the movement/rotation on the imaging time-scale is hindered, the characteristic electromagnetic dipole pattern of single dyes becomes visible in de-focused imaging, shown in (b). Three other characteristics of single fluorophores are apparent in time-series (c): A single fluorophore emits a

relatively constant fluorescence signal, if it is excited by a constant illumination intensity. Another characteristic is the blinking of the fluorophore, that is the statistic switching between the fluorescent and dark state, under continuous illumination. Blinking has different origins (for example photo-induced isomerization of the fluorophore) and is impacted by the excitation intensity, with time-scales ranging from milli-seconds to hours [95]. After a certain number of absorption-emission cycles, the fluorophore will photobleach and stop emitting in one single step.

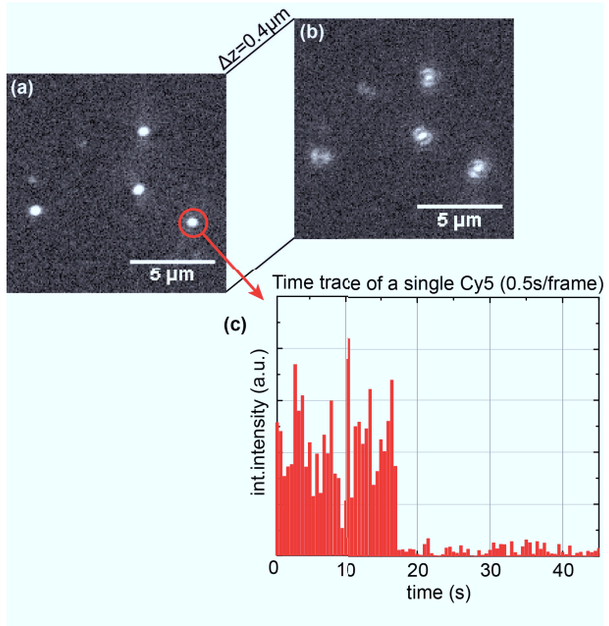

FIGURE 6.4: A low Cy5-dye density area imaged in focus on the left and the corresponding area imaged $0.4\mu\mathrm{m}$ closer to the objective on the right.

The goal of the systematic measurements was to determine a combination of imaging parameters, that allowed the imaging of single fluorophores. The found imaging parameters should (1) allow the reliable identification of all the single fluorophores within an imaged area and (2) lift their SNR above 3, a value where a fluorescence peak can be clearly distinguished from the image's overall noise.
Optimization of the imaging parameters was addressed in the following steps:

(a) A fluorophore's fluorescence output is affected by the time it is exposed to excitation light and the excitation light's power. To determine the impact of the illumination-time on the SNR of a single fluorophore, a series of measurements with **different illumination-times** and a fixed excitation power was done on the example of Cy3-NHS and Cy5-NHS. The

illumination-time resulting in the highest SNR was chosen for all of the subsequent systematic measurements.
This was followed by the systematic **power-series**, where the excitation power was varied, aiming again for the highest possible SNR. After having determined the optimum excitation power within the available range, additional measurements were done to assess, if the impact of the camera's **electron-multiplying gain setting** can lead to a further increase of the fluorophores' SNR.

(b) After having determined suitable imaging parameters, the photostability of the fluorophores should be improved. In this context, the impact of two **photoprotection systems** on the fluorophores' observation-time was tested with time-series.

6.3.2 Preliminary considerations

A fluorophore's fluorescence signal increases with the number of emitted/collected photons. Its expected SNR, versus the number of incident photons per pixel, is given by [60]

$$SNR = \frac{E_{det} \cdot N_{\gamma}}{\sqrt{(E_{det} \cdot N_{\gamma}) + {\sigma_{rn}}^2}} = \frac{N_{e^-}}{\sqrt{N_{e^-} + 12^2}}. \tag{6.1}$$

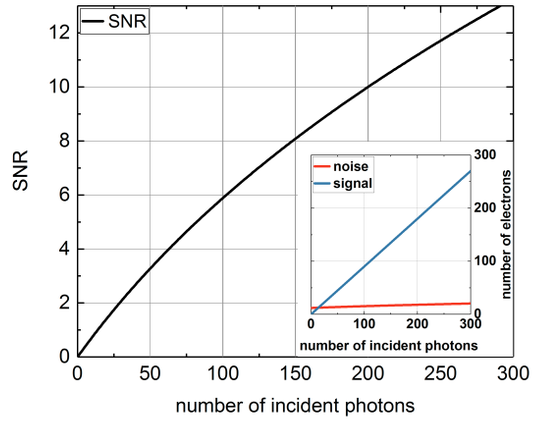

FIGURE 6.5: The theoretical SNR versus the number of incident photons per pixel, according to equation 6.1. Inset are the linearly increasing signal and the overall noise in electrons, with a lower limit of 12 e^- from the CCD camera [96]. The assumed quantum efficiency of the camera is 90%.

As mentioned in chapter 4, the overall noise depends on the number of incoming photons and the read noise of the camera, it is $12e^-$ at a read out rate of $1\mathrm{MHz}$ (see the Andor iXon Ultra888 specification sheet [96]). Figure 6.5 displays the theoretically expected behavior of the SNR, versus the number of incident photons per pixel. Inset to the figure is the linear increase of the signal itself, along with the overall noise. At a high level of incident photons, the read noise component becomes negligible and the SNR will become $\approx \sqrt{N_{e^-}}$.
The systematic measurements were done with the Cyanine and Alexa Fluor dyes embedded into a PVA-film on a plasma cleaned cover slide. The GFPem was bound unspecifically on a plasma cleaned cover slide surface. Details on the sample preparation are reported in chapter 3.

6.3.3 Varying the illumination time

While the relation between the number of excitation photons ($\propto$ P_{exc}) and emitted photons by fluorescence is governed by a fluorophore's photophysical properties (like its fluorescence QY and absorption cross-section σ_{dye}), as well as its environment (quenching effects, pH of the buffer etc.), the most straightforward way to influence a fluorophore's fluorescence output is by varying the illumination-time and the excitation power.

Measurements

Preliminary measurements were done to determine the illumination-time, that results in the highest SNR. The measurements were done, by employing the PVA slides with the embedded Cy3-NHS and Cy5-NHS respectively (chapter 3). At a constant excitation power (of $7\,\mathrm{mW}$ for Cy5-NHS and $10\,\mathrm{mW}$ for Cy3-NHS respectively), series of areas were imaged with an illumination-time ranging from $0.5\,\mathrm{s}$ to $3\,\mathrm{s}$.
By the consecutive imaging of different areas, approximately 3000 signal peaks were collected for each illumination-time. The analysis routine processed the recorded images, determined the overall noise and fitted the signal peaks with a two-dimensional Gaussian, providing the determined SNR for each signal peak (see chapter 5). For each illumination-time, a SNR-histogram with a binning of 0.5 units of SNR was generated. The histograms were fitted with a log-normal distribution

$$L(x) = \frac{1}{\sqrt{2\pi}\sigma x} e^{(-\frac{(ln(x)-\mu)^2}{2\sigma^2})}, \quad \mathrm{x} > 0, \tag{6.2}$$

that accounts for the non-symmetric distribution of the signals' SNR [97]. The fit provided the SNR's arithmetic mean E_{SNR} for a single fluorophore at the set excitation power. It is given by the log-normal distribution's arithmetic mean **E**(L(x))

$$\mathbf{E} = \frac{1}{\sqrt{2\pi}\sigma} \int_0^\infty x \frac{e^{-\frac{(ln(x)-\mu)^2}{2\sigma^2}}}{x} dx = e^{\mu+\frac{\sigma^2}{2}}, \tag{6.3}$$

where μ and σ correspond to the center and width of the distribution.

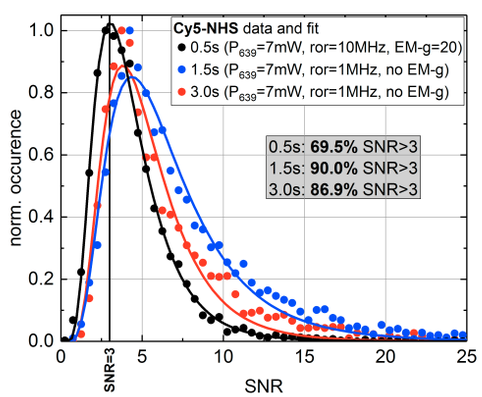

(A) SNR-distribution of single Cy5-NHS in PVA for 3 different illumination-times.

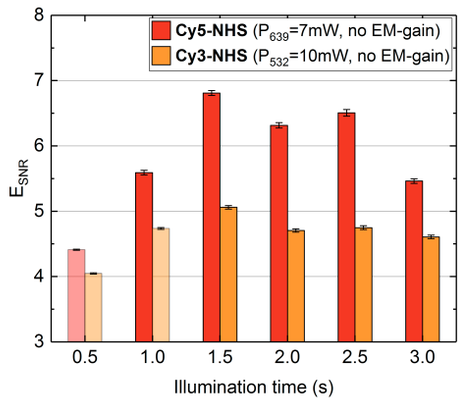

(B) The SNRs' arithmetic means vs. illumination-time for Cy3-NHS and Cy5-NHS. The E_{SNR} depicted by faint bars were derived from image series recorded with a read out rate of 10 MHz and by applying an EM-gain of 20 (see section 6.3.5).

FIGURE 6.6: SNR-distributions and corresponding fits on the example of Cy5 (A) and the determined E_{SNR} of Cy3-NHS and Cy5-NHS for the different illumination-times (B). The finally selected illumination-time for all the fluorophores was 1.5s.

Results and comments

Figure 6.6a displays the generated SNR-distributions with the corresponding log-normal fits for three of the six tested illumination-times on the example of Cy5-NHS. The distributions' width and and their arithmetic mean shift with the illumination-time, the finally selected illumination-time was the one that leads to the highest arithmetic mean E_{SNR} and shifts the highest fraction of entries above SNR$\geq$3. Figure 6.6b shows the trend of the SNR's arithmetic mean E_{SNR} for the different illumination-times tested with Cy3-NHS and Cy5-NHS. Up to an illumination-time of 1.5s, the SNR increases with illumination-time, but comes eventually to a halt at higher illumination-times. The total fluorescence output of a fluorophore, and consequently its SNR, is limited by photo-bleaching, therefore a longer illumination-time brings no advantage. The illumination-times of 0.5 s and 1 s were imaged at a chip read out rate of 10 MHz. A read out speed of 10 MHz comes with a higher read out noise. Combined with the shorter illumination-time, this resulted in a lower SNR, approaching the limit of the camera to reliably detect a single Cy3-NHS and Cy5-NHS dye respectively. The faint bars represent the measurements, where the EM-gain of the camera was applied (see section 6.3.5), that enabled the imaging of the single dyes at these lower levels of recorded photons per pixel. The adopted illumination-time for the further systematic measurements was 1.5s for all the fluorophores, the fluorescence output for each fluorophore was consequently governed by the applied excitation power. The corresponding

systematic measurements will be presented in the following.

6.3.4 Power-series

The effect of the excitation power on the SNR was tested in steps of $25\mathrm{mW}$ (corresponding to 2 to $3\mathrm{mW}$ at the surface) for each type of fluorophore. Approximately 5000 signal peaks were collected for each step and for each of the employed fluorophores. The sets of images were processed by the analysis routine, to identify, count and fit the images' fluorescence peaks.

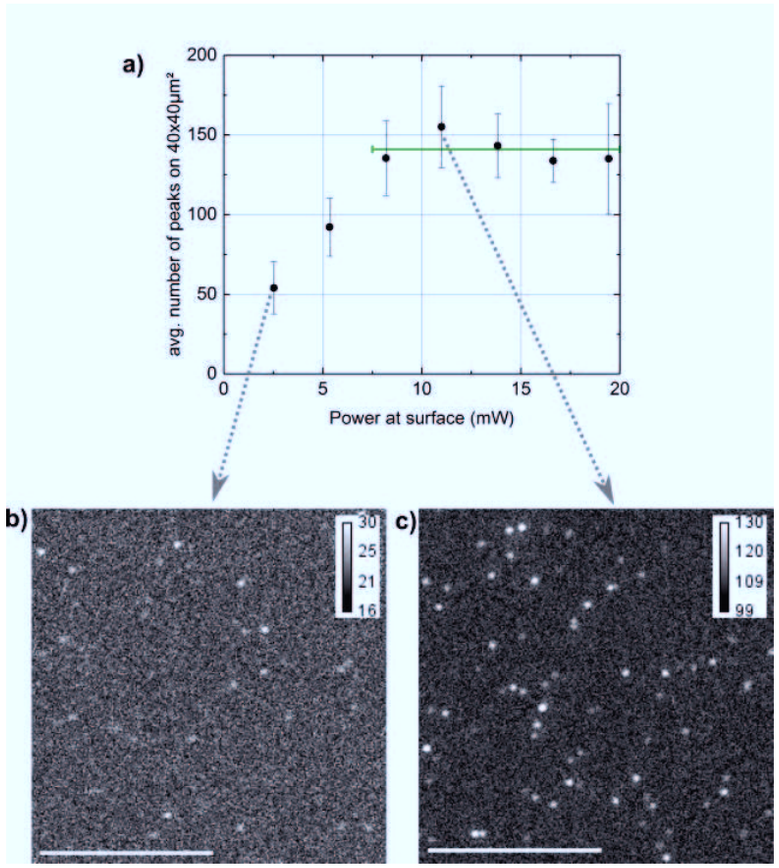

FIGURE 6.7: (a) Excitation power vs. number of identified peaks per image on the example of GFPem. The number of visible peaks increases with power and reaches eventually a plateau, marked with a green bar. Two examples of image sections taken from the GFPem power-series at an excitation power of $2.5\mathrm{mW}$ and $11\mathrm{mW}$ are shown in (b) and (c) respectively, displaying a difference considering the number of visible fluorescence peaks, as well as their SNR (Scale bar of $10\mu\mathrm{m}$, calibration bar in counts).

It was observed, that an increase of the excitation power leaded to a higher average number of identified fluorescence peaks per image. Eventually, a plateau was reached, as a further power increase did not lead to a higher number of identified peaks. Within this plateau, it was concluded, that all the present fluorophores in the imaged area, were identified. Figure 6.7(a) illustrates the average number of peaks within $40\,\mu\mathrm{m} \times 40\,\mu\mathrm{m}$ versus the applied power, together with the plateau region, on the example of GFPem.

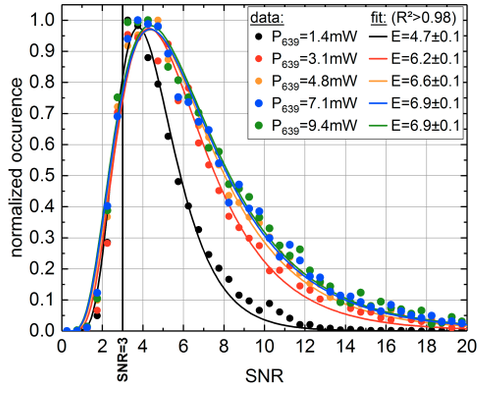

(A) SNR-distributions of single Cy5-NHS in PVA for the different excitation powers.

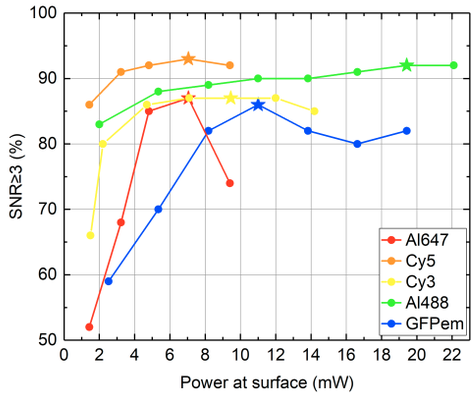

(B) The fraction of fluorophores with a SNR≥3 vs. the excitation power

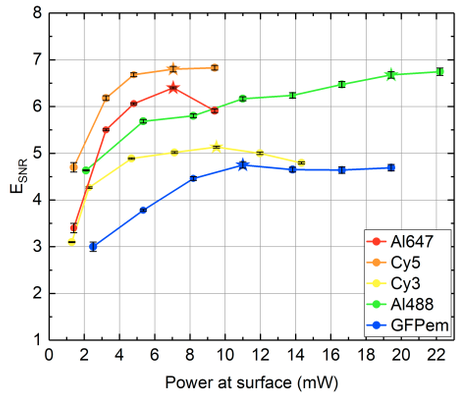

(C) The SNRs' arithmetic means E_{SNR} vs. excitation power for the employed fluorophores.

FIGURE 6.8: Log-normal fit of the SNR-distributions on the example of Cy5-NHS (a). The determined E_{SNR} of the fluorophores for the different power settings (b), as well as the corresponding fractions of fluorescence signals with a SNR≥3 (c). The finally selected powers are marked by the stars.

The normalized SNR-histograms, generated for each power setting together with the corresponding log-normal fits, are shown in figure 6.8a on the example of Cy5-NHS. The histograms' width range over several units of SNR, a behavior, that was observed for all the fluorophores. The stochastic blinking during the illumination-time (as well as the random dipole orientations of the single fluorophores embedded in the PVA film in case of the Alexa Fluor and Cyanine dyes[1]) may contribute to the broadening of the width.
For each type of fluorophore and excitation power, the fraction of entries with a SNR$\geq$3 (displayed in figure 6.8b) was determined, as well as the arithmetic mean E_{SNR} of a single fluorophore's SNR (displayed in figure 6.8c). Ideally, an increase in power would lead to a higher fraction of fluorescence peaks with a SNR$\geq$3 and a higher arithmetic mean E_{SNR}.
The trends illustrate, that the E_{SNR} correlates with the fraction of fluorescence peaks, that display a SNR$\geq$3. At low regimes, a power increase leads to a fast rise of both trends, that slows down or comes eventually to a halt by further increasing the excitation power, possibly as a result of increased blinking. The selected powers, marked by the stars, were the ones, that lead to the highest fraction of SNR$\geq$3 and simultaneously to the highest E_{SNR}.
Table 6.4 lists the excitation powers selected for the different fluorophores, for the further measurements. The majority of fluorophores displays a SNR$\geq$3 with the selected excitation powers.

The software of the EMCCD camera allowed the back-calculation of the number of photons, collected per pixel at a given λ_{em} [2] and hence the average signal amplitude, from the fit, in photons. The determined values are listed in the final column of table 6.4. Furthermore, the determined molecular brightness mB can be found in the appendix A.4.

TABLE 6.4: The fraction of signals with SNR$\geq$3, the signals' arithmetic mean E_{SNR} and the corresponding power.

	P_{meas} (mW)	SNR$\geq$3(%)	E_{SNR}	signal amp. $E_{N_\gamma}(N_\gamma)$
Alexa647	7	85	6.4$\pm$0.1	163$\pm$2
Cy5	7	91	6.8$\pm$0.1	220$\pm$5
Cy3	9	87	5.1$\pm$0.1	234$\pm$2
Alexa488	19	92	6.7$\pm$0.1	1152$\pm$32
GFPem	11	86	4.8$\pm$0.1	265$\pm$4

[1] The embedding of fluorophores in PVA hinders a rotating movement on the time-scale of the measurement, a linearly polarized excitation beam does not equally excite every dipole orientation. In this context, tests were done also with a $\lambda/4$-polarizer foil in the linearly polarized excitation beam. While the foil had a positive impact on the homogeneity of the signals' SNR, the excitation power itself was reduced, leading to a much decreased SNR. Since in the later experiments, the fluorophores' dipole orientation will not be 'locked' by the polymer matrix, it was decided to continue the excitation with linearly polarized light.

[2] The selected λ_{em} corresponded to the maximum emission wavelength of the fluorophore. This is an approximation not taking into account the distinct emission spectra for each fluorophore.

Observations and comments

Comparing the determined photon amplitudes E_{N_γ} and corresponding E_{SNR} from table 6.4 with the expected values from figure 6.5 reveals a discrepancy: The determined E_{SNR} are lower than expected (as derived from equation 6.1). On the example of GFPem, the determined overall noise values are plotted together with the expected values in figure 6.9. In this case, the determined noise values are roughly double the theoretically expected value, leading to the decrease of the SNR of approximately 50%. While in general, the determined noise was generally above the theoretically expected values, it was more pronounced in the green and yellow spectra. Also, the number of incident photons does not increase linearly with the the excitation power (and hence the number of excitation photons), a result a the fluorophores' photophysics. Considering their fluorescence quantum yield QY and molecular absorption cross-section σ_{dye} from the literature (see tables 6.1, 6.2 and 6.3), the determined values deviate from the expectations: The values found for Alexa647-NHS are slightly lower than the ones of Cy5-NHS and also the values found for GFPem are lower than the ones for Cy3-NHS, which is the fluorophore with the lowest QY and σ_{dye} of this list. This may be a result of the different environments, whereas the Cyanine and Alexa Fluor dyes are embedded in a PVA film, GFPem is bound unspecifically to a plasma cleaned cover slide (chapter 3).

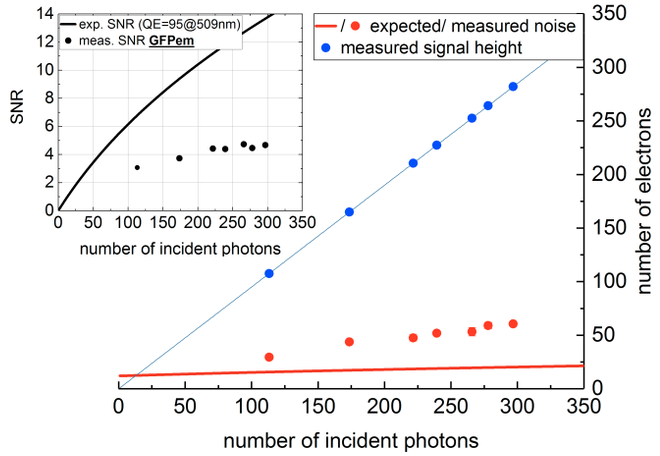

FIGURE 6.9: Displayed are the measured noise and the expected noise value versus the number of incoming photons. Inset are the determined E_{SNR} versus the expected value, according to equation 6.1: The graph reveals that the measured noise is higher than the theoretically expected, leading to a decreased SNR.

6.3.5 EM-gain series

The camera's EM-gain can be a useful tool to boost the fraction of signals with a low SNR, while imaging under low-light conditions. This section presents the measurements, done in order to find out, if the use of the EM-gain is advantageous in combination with the previously determined excitation power.

Preliminary considerations

In low-light conditions, the read noise from the camera is the limiting noise factor, that needs to be overcome. The EM-gain's task is to multiply the electron signal, generated from the incoming photons, before the chip is read out. In this way, the impact of the read noise on a fluorophore's SNR is reduced, leading to an improved SNR.

Two factors were considered when using the EM-gain:

(a) **Relevant photon range for the EM-gain application [98, 99]**
Figure 6.11a shows the theoretically expected SNR per pixel depending on the number of incident photons, with and without the EM-gain application. The figure illustrates that the EM-gain application is advantageous only up to a cross-over point where the shot noise becomes the limiting noise component. The EM-gain multiplies the signal created by the incident photons (photoelectrons), yet it also affects the shot noise and the dark noise in the following way

$$\sigma_{sn,EM} = g \cdot f \cdot \sqrt{E_{det} \cdot N_\gamma} \tag{6.4}$$
$$\sigma_{dn,EM} = g \cdot f \cdot \sqrt{\sigma_{dn}}, \tag{6.5}$$

resulting in a SNR given by

$$SNR_{EM} = \frac{E_{det} \cdot N_\gamma}{\sqrt{f^2 \cdot ((E_{det} \cdot N_\gamma) + \sigma_{dn}^2) + (\frac{\sigma_{rn}}{g})^2}}. \tag{6.6}$$

f corresponds to the excess noise factor. It is due to the fact that the multiplication is a probabilistic process with variation in the EM-gain. With noise factor of 1.4 and a read noise of $12e^-$, the cross-over point is reached at a signal strength of ~160 photons per pixel.

(b) **Selecting the EM-gain factor**
According to equation 6.6, an excessive EM-gain multiplication factor brings no further advantage. The impact of the EM-gain value on the SNR for different numbers of photons per pixel is shown in figure 6.10b, revealing that above a certain EM-gain value, the SNR will approach a constant value.

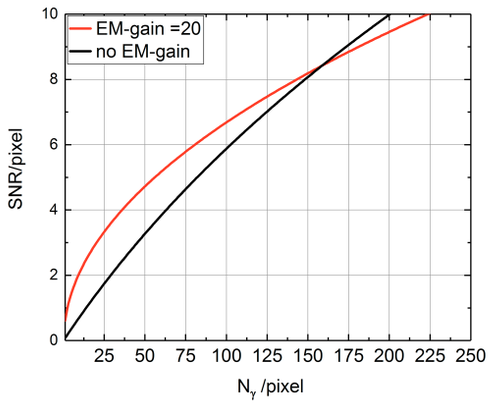

(A) The theoretically expected SNR with and without the EM-gain application vs. the number of incoming photons N_γ per pixel.

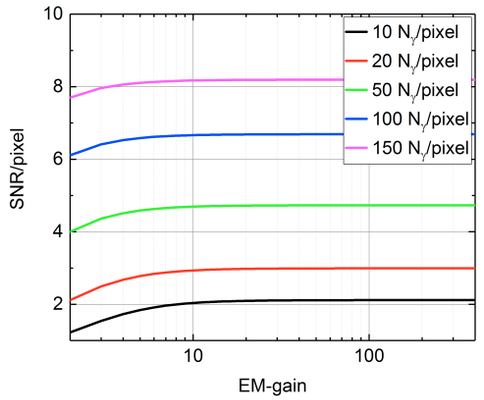

(B) Influence of the EM-gain value on the SNR depending on the number of photons N_γ per pixel.

FIGURE 6.10: The impact of the EM-gain application on a fluorophore's SNR, according to equation 6.6 .

Data analysis of the recorded power-series images revealed the fraction of signals with an amplitude below 160 photons for each fluorophore (in table 6.5), to assess if an EM-gain application can improve the signals' SNR. In the case of Alexa488, over 99% of the fluorescence signals have a SNR$\geq$3, an EM-gain application may not bring a benefit.

TABLE 6.5: The fraction of signals with a signal height $N_\gamma \leq 160$, with the formerly determined excitation powers.

	P_{meas} (mW)	peak height $\leq$160 γ/pixel (%)
Alexa488	19	$\leq$1
GFPemerald	11	8
Cy3	9	25
Cy5	7	34
Alexa647	7	49

Measurements

In analogy to the previously presented power-series, measurements with each fluorophore were done, where the EM-gain factor was varied. The selected EM-gain ranged from the lowest multiplication factor 2 up to 50. For each setting, approximately 5000 fluorescence signals were recorded.

The EM-gain application was judged useful for a type of fluorophore, if it led to an increase of the fraction of signals with a SNR≥3, compared the case without EM-gain application, and if the application would lead to a higher E_{SNR}.

Results and comments

The figures 6.11a to 6.11e show the impact of the EM-gain on the SNR distribution of the fluorophores, exemplified for low EM-gain factors.
For both Alexa Fluor conjugates, the EM-gain lifts the E_{SNR} and increases the fraction of signals with a SNR≥3.
While the EM-gain application leads to a higher E_{SNR} in the case of Cy5-NHS, the fraction of signals with a SNR≥3 remains unchanged. It can be seen that for Cy3, the application of the EM-gain had hardly any impact on the SNR distribution, considering both criteria. In the case of GFPem, the SNR distribution had a clearly negative impact on the SNR distribution, as both the fraction of signals with a SNR≥3, as well as E_{SNR} were shifted to lower values. This trend is in agreement with the result from table 6.5, since only 8% of the signal peaks have an amplitude below 160 photons.
The application of a high EM-gain did not bring a further improvement for the determined excitation time and powers, shown in figure 6.11f. As a reference, the arithmetic means without EM-gain application are plotted as horizontal lines.
The impact of the EM-gain on the fluorescence signals deviates from the expectations, considering figure 6.10 and table 6.5. The EM-gain application lead to an improvement of the E_{SNR} in the case of Alexa488-NHS, although the average peak height is far above the range of incoming photons, that is considered useful for a potential EM-gain application, according to figure 6.11a. This may be a result of underestimated overall noise.

The results of the imaging parameter optimization are summarized in table 6.6. With the selected parameters, the majority of the fluorophore populations are lifted to a SNR level above 3 and an E_{SNR} close to 5 or more. The determined imaging parameters are hence considered suitable for the imaging on single-molecule level.

TABLE 6.6: The results of the imaging parameter optimization for t_{frame}=1.5 s.

	P_{meas}	SNR≥3	E_{SNR}	EM-gain
Alexa488	19	95%	8.9±0.3	20
Alexa647	7	91%	9.1±0.1	20
Cy5	7	91%	8.9±0.1	20
Cy3	9	87%	5.1±0.1	-
GFPemerald	11	86%	4.8±0.1	-

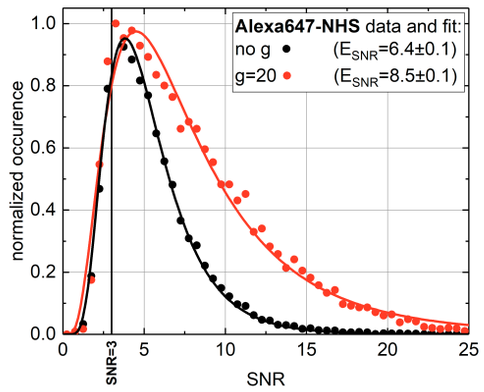

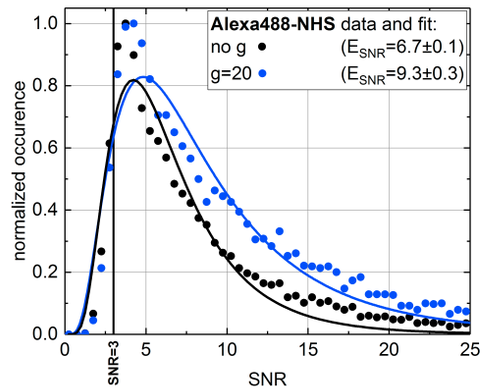

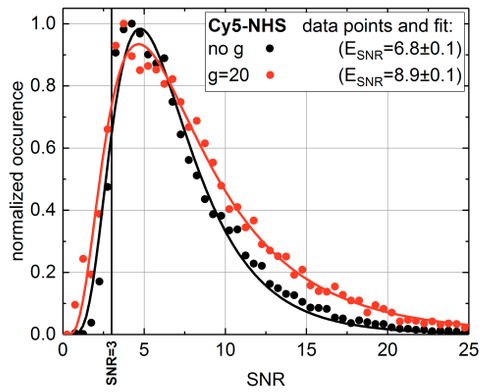

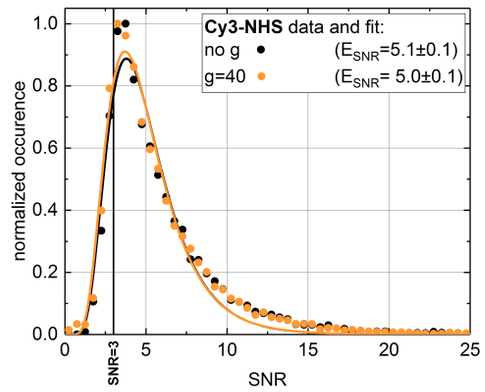

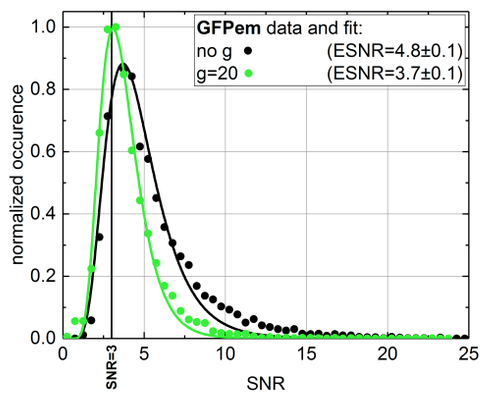

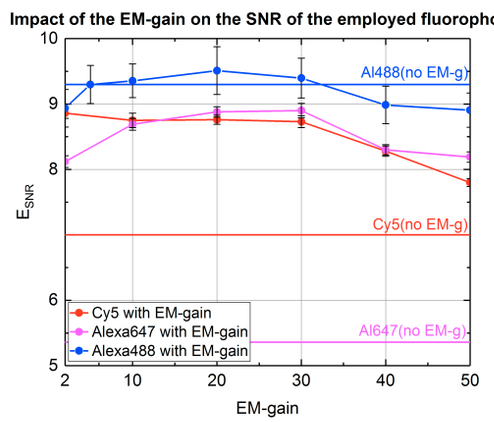

FIGURE 6.11: Impact of the EM-gain on the different fluorescence intensity distributions and E_{SNR}.

6.4 Photoprotection

Following the imaging parameter optimization, this section introduces two photoprotection systems that have been tested, in order to improve the fluorophores' photostability.

6.4.1 Oxygen-scavengers

In the context of a fluorophore's photostability, molecular oxygen (O_2) plays a key role:
On one hand, triplet oxygen efficiently quenches the fluorophore's triplet states, that are responsible for its blinking. On the other hand, quenching results in the formation of the higher energy singlet O_2, which rapidly reacts with the exposed chemical groups in organic dyes, leading to oxidization. Due to the high reactivity of singlet O_2, oxidization occurs fast. The oxidative damage is permanent and the fluorophore does not fluoresce anymore [100, 101].

The approach, to improve the fluorophores' photostability, is to scavenge the oxygen, present in the imaging buffer surrounding the fluorophore, while simultaneously adding a chemical component to prevent or to ameliorate blinking, by depopulating the triplet state.
Both enzymatic oxygen scavenging systems, that have been tested, are commonly in use [102],[103]: The well established Glucose oxidase and catalase (GOC) system, as well as the protocatechuic acid / protocatechuate-3,4-dioxygenase (PCD) system [50]. As an alternative triplet quencher, reports have suggested β-mercaptoethanol[104] as well as Trolox [105]. In this work, Trolox has been added to the buffer solution. It is a water-soluble vitamin E analog, that suppresses blinking and that has also been reported to reduce photobleaching [106].

(a) **The GOC oxygen-scavenging system (GOC)**
GOC consumes the oxygen from the buffer by oxidizing the glucose. The product of this reaction is gluconic acid and hydrogen peroxide H_2O_2. H_2O_2 shows adverse effects on the fluorophores [107], it will be broken down by in the second step the catalase, the products being water and again O_2. The gluconic acid will lead to an acidification of the solution, which can have a deteriorating effect on the fluorophores' brightness [108].

(b) **The PCD oxygen-scavenging system (PCD)**
PCD is a well studied enzyme in biological applications, that demand an anaerobic environment and a stable pH for a prolonged amount of time [109]. It catalyzes the conversion of protocatechuic acid (PCA) to β-carboxy-cis, cis-muconic acid in one step, consuming the oxygen present in the buffer solution.

The corresponding reaction schemata are shown in figure 6.12.

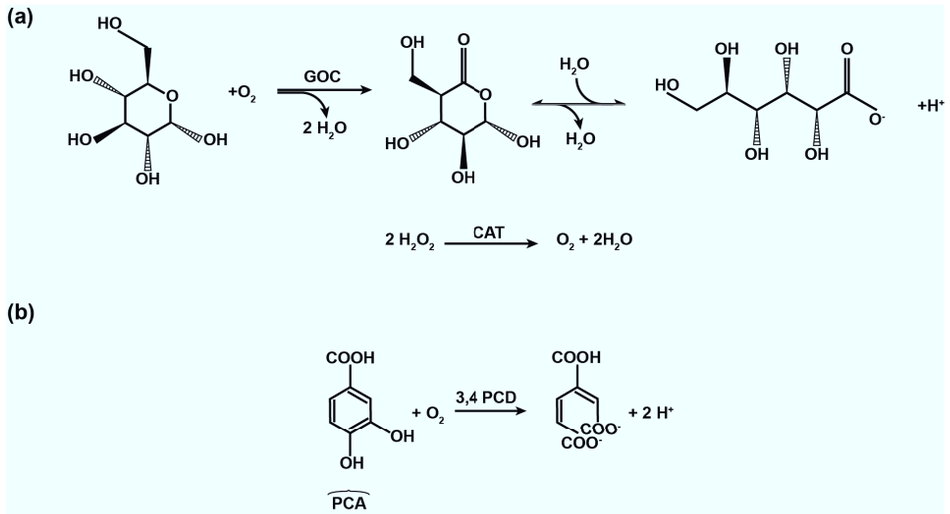

FIGURE 6.12: The reaction shemes of the O_2-scavenger systems GOC (a) and PCD (b) [50].

6.4.2 The O_2-scavengers' impact on the observation time

The O_2-scavenger's impact on a fluorophore's photostability was tested with time-series. Consecutive imaging of the same area provides the average observation time of the fluorophore, with and without added photoprotection, and allows to quantify the percentage of fluorophores, that have photobleached after each frame of $1.5\mathrm{s}$.

The samples, used to test the O_2-scavengers effectiveness, were different streptavidin conjugates, multilabeled with one of the fluorophores of interest (Alexa488 or Alexa647 from Thermofisher, Massachusetts, USA), respectively Cy3 or Cy5 form Amersham plc, Buckinghamshire, UK). Before imaging, the streptavidin-conjugates were tethered specifically to the functionalized glass cover slide surface, a concentration of $\approx 200\,\mathrm{pM}$ resulted in a density of more than 300 fluorescence signals per area of $40\,\mu\mathrm{m} \times 40\,\mu\mathrm{m}$ (details about the surface preparation are given in chapter 7).
For reference, the first time-series were recorded (with the previously determined excitation powers) without an added scavenging system. A time-series consisted of 40 consecutive frames, corresponding to an illumination time of $60\mathrm{s}$. In a second step, the buffer in the imaging channel was replaced by the buffer with the added O_2-scavenger and Trolox. The results of the time-series with the different streptavidin samples and both O_2-scavengers will be presented in the following.

The labeled streptavidin-conjugates

Figure 6.13 displays examples of the recorded measurement series for the different streptavidin-conjugates. The trends display the normalized number of fluorescence peaks versus the observation time. The series with the added PCD system are marked red, the series with the added GOC system are marked blue and the series without any added scavenging system, are marked black.

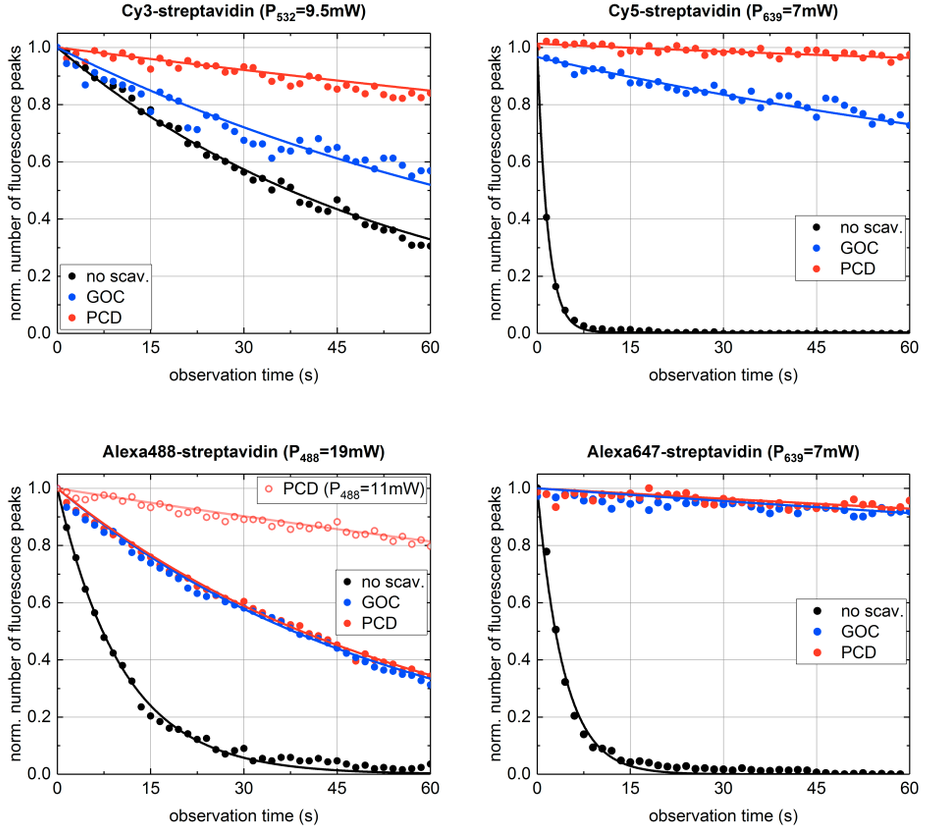

FIGURE 6.13: Impact of the oxygen-scavenger systems GOC and PCD on the observation time of the streptavidin-conjugates. One data point corresponds to an illumination time of 1.5s.

At first sight, the figures reveal that both scavenging systems have a substantial impact on the observation time of the labeled streptavidin-conjugates. In combination with the tested cyanine dyes, the PCD system seemed to be more effective than the GOC system. In the case of Alexa647-streptavidin, both O_2-scavengers perform similarly well.

The normalized time-series were modeled with a mono-exponential decay fit

$$N(x) = e^{-\frac{t}{t_{obs}}}, [t] = s, \tag{6.7}$$

where t_{obs} ($[t_{obs}]$=s) corresponds to the average observation time of a single fluorophore, before photobleaching occurs when imaged with the previously set parameters.
The resulting observation times t_{obs}, displayed in table 6.7, list the percentage of fluorophores, that bleach per second and how this number is affected by the photoprotection systems.
By employing either one of the O_2-scavengers, the calculated fraction of photobleached fluorophores per second, decreased down to 1% and less, becoming negligible. The determined imaging parameters for Alexa488 lead to a more pronounced decrease of 4% per frame. By decreasing the excitation power down to $11\mathrm{mW}$, the average observation time of the fluorophore increased to a level similar to the other streptavidin-conjugates and the decrease per frame dropped below 1% [3].

TABLE 6.7: The determined average observation time t_{obs}, resulting from the exponential fit for the different streptavidin-conjugates, together with the average percentage of fluorophores, that bleach per second.

	Cy3-strep.		**Cy5-strep.**	
	t_{obs} (s)	decrease/s	t_{obs} (s)	decrease/s
no scav.	60±5	2%	1.7±0.2	44%
GOC/TX	108±11	≤1%	203±29	≤1%
PCD/TX	339±39	≤1%	1214±126	≤1%
	Alexa488-strep.		**Alexa647-strep.**	
	t_{obs} (s)	decrease/s	t_{obs} (s)	decrease/s
no scav.	8±2	12%	4.2±0.3	22%
GOC/TX	36±2	3%	617±83	≤ 1%
PCD/TX	41±5(293±48)	2% (≤1%)	870±59	≤ 1%

[3] From the systematic power measurements with single Alexa488 in PVA resulted, that with an excitation power of 11mW, still over 90% of the imaged single Alexa488 maintain a SNR≥3.

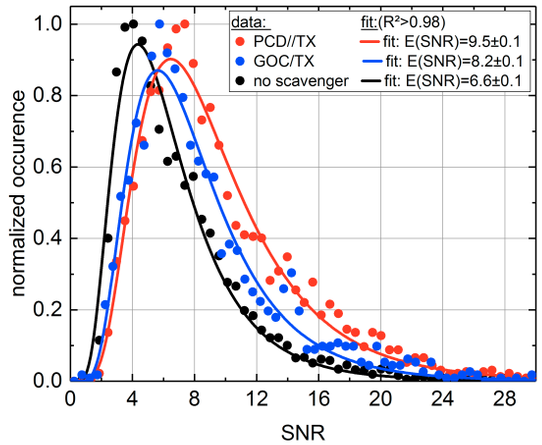

FIGURE 6.14: The impact of the scavenging systems on the fluorescence peaks' SNR of the kinetic series' first frames on the example of Cy5-streptavidin.

An effective scavenger-system results in less photoblinking during the exposure time and consequently to an improved SNR. The impact of both systems on the SNR is shown in figure 6.14 on the example of Cy5-streptavidin, both scavengers shift the average SNR to higher values.

GFP emerald

In analogy to the previous systematic measurements, single GFPem were bound unspecifically to the surface of a plasma cleaned cover slide. Time-series with and without the added oxygen scavenger systems were recorded with the previously determined optimum excitation intensity of $11\mathrm{mW}$ set and an exposure time of $1.5\mathrm{s}$ per frame. Examples of the recorded time-series are shown in figure 6.15, the average observation times from the decay fits are listed in table 6.8.
While GFPem has an improved photostability over the wild-type GFP, it has been reported to display a fast bleaching component [110, 111]. With an excitation power of $11\mathrm{mW}$, the average observation time t_{obs} per GFPem is $6.6\,\mathrm{s}$, meaning the number of fluorescence peaks has decreased by 20% after each frame without the application of a photoprotection system. Compared to the previously tested organic fluorophores, the impact of the oxygen scavenger systems on the observation time was lesser, when applied to GFPem. With the PCD system, t_{obs} extends to over $12\mathrm{s}$, which corresponds to a decrease of number of fluorescence peaks of 12% per frame.

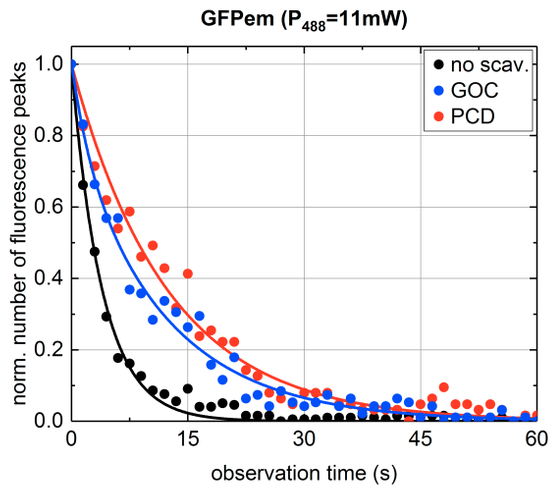

FIGURE 6.15: The impact of the enzymatic O_2-scavengers on the observation time of GFP emerald with an excitation power of $11\,\mathrm{mW}$ and illumination time of $1.5\,\mathrm{s}$ per frame.

TABLE 6.8: The average observation time of single GFPem resulting from the exponential fit.

	t_{obs}(s)	decrease/s
no scav.	6.6± 0.3	14%
GOC	10.5± 1.7	9%
PCD	12.2± 1.4	8%

6.4.3 Comments

While both scavenger systems have a great impact on the photostability of the Cyanine and Alexa dyes, reducing the fraction of photobleaching to less than 1% per second, the impact of the O_2-scavengers is less for GFPem. Using the PCD-system, 8% of the GFPem spots are bleached per second, which needs to be taken into consideration while performing the colocalization studies (see chapter 8): Evidently, an area to be imaged must not be exposed to excitation light before the imaging takes place, to prevent any avoidable photobleaching.

Chapter 7

Surface preparation: Tethering single molecules

7.1 Introduction

Single-molecule imaging on a WFM requests the tethering of the sample to the cover slide surface. Although proteins tend to stick by nature to an untreated silica surface, this should be avoided, as it may result in the surface-induced denaturation or malfunction of the protein.

The cover slide treatment aims to block unwanted non-specific binding, while offering specific binding sites, that allow the tethering of the protein without affecting its functionality. A number of passivation protocols have been reported. Two widely applied methods are the covalent surface coating with Polyethylene glycol (PEG) [112–114] and the adsorption of bovine serum albumin (BSA) [115–117]. In both cases, the surfaces are covered with macromolecules, which mask the glass surface and thus prevent the sticking of biomolecules.
In a first approach, the blocking performance of BSA, adsorbed to the surface, was tested. Unfortunately, the intrinsic fluorescence of the BSA in the green/yellow spectra was too high to be useable for the planned measurements on single-molecule level.
The finally applied method in this work was the surface passivation with a PEG 'carpet'. The surface's binding sites are introduced by mixing a small fraction of PEG with biotin at the terminal end of the PEG chain to the PEG. The specific binding between the biotinylated sample and the surface is achieved by a neutravidin linker. The finally employed protocol [1] will be outlined in the following.

7.2 Slide preparation protocol

It is mandatory for a successful single-molecule experiment to have a surface as clean as possible. Fluorescent dirt, that cannot be differentiated from the sample, gives a false positive signal, that can lead to misinterpretation of the data. Any kind of negligence must be avoided during the slide preparation. Most steps of the surface protocol were performed inside the clean air box, in order to avoid dust particles on the cover slide. Before starting, the inside

[1] provided by Dr. Iris von der Hocht from ICS-5: Molecular Biophysics, Forschungszentrum Jülich

of the clean air box was cleaned with de-ionized water and ethanol of a high spectral purity. A flow chart of the slide preparation is shown in figure 7.1, followed by the description of each step involved.

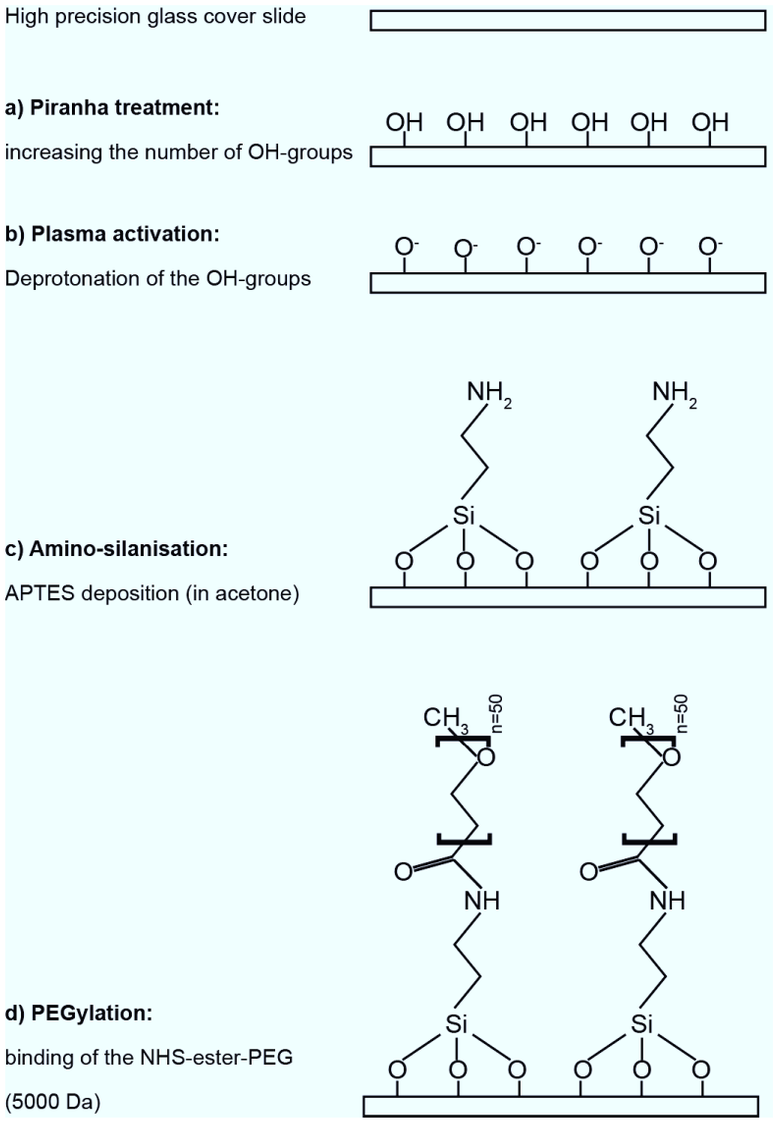

FIGURE 7.1: The surface protocol steps

a) Piranha cleaning:

Usually a batch of one PEG and four bioPEG slide sandwiches composed of one $24\,\mathrm{mm} \times 50\,\mathrm{mm}$ and one $22\,\mathrm{mm} \times 22\,\mathrm{mm}$ were prepared. The top faces of

the rectangular slides were marked, by breaking off one corner. The first step of the protocol is the piranha cleaning of the cover slides under the ventilated hood. Piranha cleaning was done to remove organic dirt from the surface and to introduce surface hydroxyl groups (OH). The piranha solution needed to be freshly prepared. It consisted of one part of a $35\,\%$ aqueous solution of hydrogen peroxide and two parts of concentrated sulfuric acid. Mixing up these two reactive components started a strong exothermic reaction. The hydroxylation of the surface increased the number of OH-groups, making the surface hydrophilic.
After one hour of incubation, each one of the immersed cover slides were removed from the piranha solution. They were transferred, one by one, to a glass rack filled up with de-ionized water and then transferred to the clean air box. It was imperative to not touch the wet cover slides with the bare fingers. They were rinsed thoroughly with milliQ water and dried with a stream of nitrogen. During the drying, care was taken to blow off the water droplets quickly and in a single direction, to prevent residues from the drying process. It was avoided to move the hand, holding the nitrogen valve, over the slide, to prevent dust or skin particles being blown to the surface.

b) Plasma activation:

Having rinsed and dried the slides, they were placed on a cleaned glass rack and plasma cleaned for ten minutes at full power. The oxygen-plasma breaks effectively most organic bonds contaminating the surface. Also, the surface is activated; the hydroxyl groups of the surface will be replaced by O^- groups. While the cover slides were being activated in the plasma cleaner, the glass racks used for the piranha cleaning were rinsed thoroughly with water and dried with a nitrogen stream, to get rid of any remaining piranha. The racks were then washed with acetone and dried again with nitrogen. This was repeated twice, to make sure the racks were absolutely dry for the next step: the silanization.

c) Silanization:

Silanization of the surface was needed to later bind the PEG 'carpet'. The amino-silane used in this protocol, acting as a coupling agent between the activated glass surface and the NHS-ester PEG, was (3-Aminopropyl)triethoxysilane APTES (from Sigma-Aldrich, Missouri, USA). APTES binds to the hydroxylated surface by hydrolysis of the silane's ethoxy groups (with ethanol as leaving group), resulting in an aminopropyl-terminated surface. Amino-silanization was done with a 2%(v/v) solution of APTES in acetone at room temperature. In order to avoid absorption of air humidity that decreases the components' reactivity, the silane, as well as the acetone, were removed from the fridge, to reach room temperature. After activation, the slides were removed from the plasma cleaner and transferred to the dried glass racks. The silane solution was poured to the racks and the slides stayed immersed for $15\,\mathrm{min}$. After $15\,\mathrm{min}$, the slides were removed, one by one with tweezers and rinsed quickly with milliQ water. Silanization made the slides water-repellent; drying with nitrogen was now fast and straightforward. The slides were then placed in a

petri dish and covered with a lid.

d) PEGylation:

The PEG and terminal biotinylated PEG (bioPEG) with a molecular weight of 5000Da (CH_3O-PEG-NHCO-C_2H_4-CONHS and Biotin-CONH-PEG-NH_2 from Rapp-Polymere, Tübingen, Germany) was aliquotized under nitrogen atmosphere to retain its reactivity and stored at $-20\,°\mathrm{C}$.

During plasma activation of the cover slides, the PEG and biotinylated PEG aliquots were removed from the freezer and allowed to gain room temperature. For the highest reactivity, the PEG and bioPEG solutions were prepared just before the PEGylation step. Conveniently, the PEG and bioPEG had been aliquotized to prepare an amount of solution enough for five slides in total; approximately $50\,\mathrm{mg}$ of PEG and approximately $5\,\mathrm{mg}$ of bioPEG, in powder form. A $1\,\mathrm{M}$ solution of sodium bicarbonate $NaHCO_3$ was freshly prepared and adjusted with hydrochloric acid to a pH of 8.5. To remove impurities, the solution was filtered with $0.1\,\mu\mathrm{m}$ syringe filters (puradisc, Whatman plc, Buckinghamshire, UK.).
For the PEG-slides, the PEG was dissolved in a mixture of $450\,\mathrm{ml}$ of water and $50\,\mathrm{ml}$ of $NaHCO_3$ resulting in a 10% PEG-solution. The solution was then de-gazed in the sonicator for $30\,\mathrm{s}$ to remove air bubbles from the solution to achieve a more homogeneous PEGylation. $100\,\mu\mathrm{l}$ of this solution were then pipetted on top of the large rectangular cover slide in the petri dish. The solution was spread and covered with the smaller slide placed on top.
For the bioPEG-slides, $5\,\mathrm{mg}$ of bioPEG was dissolved in $500\,\mathrm{ml}$ of water. The solution was then diluted 10 times. For four bioPEG slides, $4\,\mu\mathrm{l}$ of the bioPEG solution was mixed with $400\,\mu\mathrm{l}$ of the PEG solution, resulting in a ratio of $1{:}10^4$ bioPEG:PEG. Before pipetting the solution to the cover slides, it was again de-gazed for $30\,\mathrm{s}$. The cover slide sandwiches were incubated for at least two hours or preferably overnight in a humid environment, to allow the reaction to complete and to prevent the drying out of the solutions.

d) Building the imaging chambers and storing of the cover slides:
After the incubation time, both slides of the sandwich were separated with tweezers. The cover slides were rinsed with de-ionized water, to wash off the excess of unbound PEG. After a successful PEGylation, a clear difference in hydrophobicity between the PEGylated slide and the untreated opposing side of the slide could be observed. Both slides rinsed and dried were then used immediately or they were stored in falcon tubes, with their untreated side facing each other. The falcon tubes were flushed gently with nitrogen to remove air humidity. The closed tube was sealed with parafilm. The cover slides could be stored at $-20\,°\mathrm{C}$ for at least several weeks.
The assembled imaging chambers consisted of two PEGylated cover slides, held together by a piece of double-sided sticky tape with the channels cutout, to accommodate the sample solution. A schematic representation is given in figure 7.2.

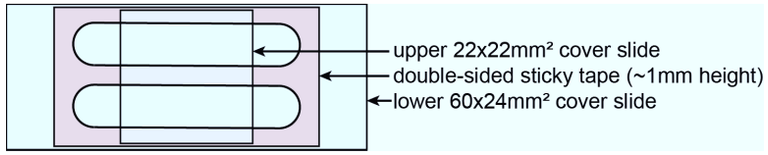

FIGURE 7.2: The cover slide sandwich with the imaging chambers

7.3 The slide background

Every single-molecule experiment on the surface starts with the check of the slide's surface for background signals. The imaging of the surface (before putting the sample), followed by the assessment of the slide background's suitability for the planned measurement, is mandatory for a later statement about the sample condition and the success of the experiment. Ideally, the background has an even intensity distribution and very few background peaks. While single background peaks are helpful to focus on the surface, an increased number can make the slide useless for surface measurements on single-molecule level.
There are two types of unwanted background peaks and they can have different sources: Fluorescence coming from impurities attached to the surface and scattering. On single-molecule level, differentiating between an impurity peak and a sample peak may become impossible since the SNR can be low and similar in both cases. They can show a similar bleaching behavior as well. Scattering typically differs from small dust particles as it does not show photobleaching.

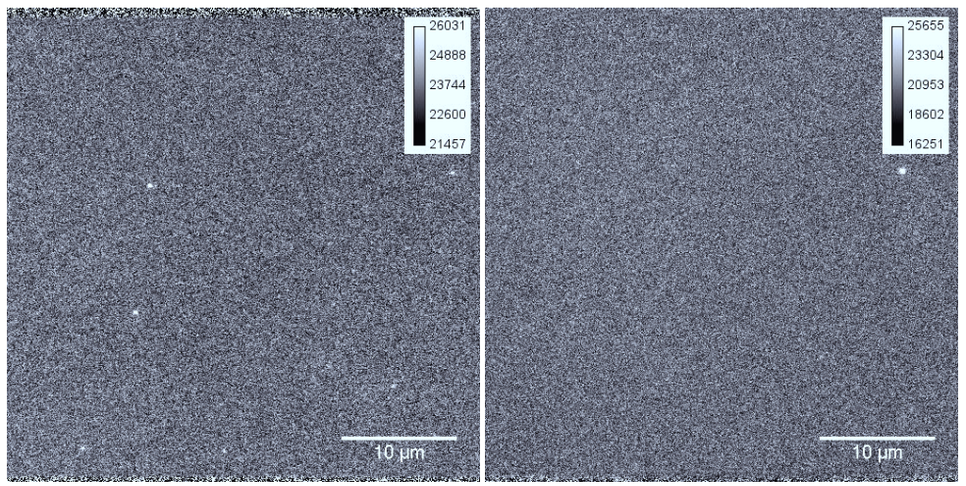

(A) Background in the green channel.

(B) Background in the red channel.

FIGURE 7.3: Representative background images of a $40\,\mu\mathrm{m} \times 40\,\mu\mathrm{m}$ area in the green **(a)** and the red channel **(b)** of a bioPEG surface imaged with Tico buffer.

Background characteristics are not identical in all colors. Having prepared the slides with all due care, a higher number of background spots is more likely to occur in the green and yellow channel, than in the red channel. Impurities are more likely to fluoresce in the green and yellow spectral range, than in the red. The acceptable number of background peaks for measurements on single-molecule-level is not a strict border, rather it must be in accordance with the number of expected sample peaks. The average number of background spots is assessed from the images of a dozen different surface areas, imaged with measuring buffer only. A surface was considered suitable for the experiment if it displayed an average number of background spots not exceeding 10% of the total number of sample spots to be expected. In general, the maximum number of peaks on a $40\,\mu\mathrm{m} \times 40\,\mu\mathrm{m}$ area should not exceed 300 peaks (for the ease of automatized data analysis), the maximum number of background peaks should therefor not exceed 30 peaks. In the case of the CFPS system, presented in chapter 8, the number of synthesized GFP per $40\,\mu\mathrm{m} \times 40\,\mu\mathrm{m}$ is lower, the maximum number of background peak in the green channel should therefore not exceed approximately 5 spots. Figure 7.3(a) and figure 7.3(b) show two $40\,\mu\mathrm{m} \times 40\,\mu\mathrm{m}$ areas in the green and the red channel of a PEG slide, that were considered suitable for the carried out colocalization measurements.

7.4 Testing the slide performance with Alexa647-streptavidin

The background check of the slides was followed by the check of the blocking performance and binding capability using a standard sample. The slides' ability to prevent non-specific binding, as well as the number of occupied biotin anchors on the surface, were tested separately. The chosen standard sample was Alexa647-labeled streptavidin (Life Technologies Co., California, USA). With a dissociation constant k_d of approximately $10^{-14}\,\mathrm{mol/L}$, the streptavidin-biotin bond is one of the strongest non-covalent bonds known in nature. It enables the estimation of occupied biotin anchors at very low concentrations of Alexa647-labeled streptavidin added.
With its labeling-ratio of approximately 5, Alexa647-streptavidin shows a good SNR. Its long term stability allows to compare the reproducibility of the slide batches over time.
As a starting point, the PEG-slides' ability to prevent non-specific binding was tested. The testing procedure, which was the same for both the PEG slides, as well as the biotinylated PEG slides, will be described in the following.

A dilution series was made of the Alexa647-streptavidin's stock solution in Tico buffer; ranging from $90\,\mathrm{pM}$ up to $1\,\mathrm{nM}$. Starting with $90\,\mathrm{pM}$ of streptavidin, $100\,\mu\mathrm{l}$ of solution was injected into the cover slide sandwich channel. After an incubation of $40\,\mathrm{s}$, the channel was rinsed with $3\,\mathrm{ml}$ of Tico buffer ($\equiv$ 30 times the channel's volume). The channel was rinsed by creating a flow with a pipette on one side of the channel and a liquid absorbing paper tissue on the other. The homogeneity of the surface and the passivation performance were tested by imaging again at least a dozen areas of the channel's surface. By moving the microscope's stage in one direction only, eventual bleaching of the streptavidin, that could lead to an over-estimation of the slide's blocking

performance, was avoided. The procedure was repeated with increasing concentrations until the blocking limit was surpassed.
The concentration, at which the blocking is not sufficient anymore, is not a rigid border. It rather depends on the number of un-specifically attached molecules still considered acceptable in relation to the number of specifically bound molecules of interest. It was experienced that on a $40\,\mu\mathrm{m} \times 40\,\mu\mathrm{m}$ area, up to 300 evenly distributed peaks can still be well distinguished as single peaks. Requesting not more than 10% to be attached un-specifically, the blocking limit is reached at 30 peaks.Figure 7.4 shows a series of blocking tests with different streptavidin concentrations up to $1\,\mathrm{nM}$. It can be concluded that PEG-slides reproducibly block the non-specific attachment of labeled streptavidin up to more than $0.5\,\mathrm{nM}$ added.

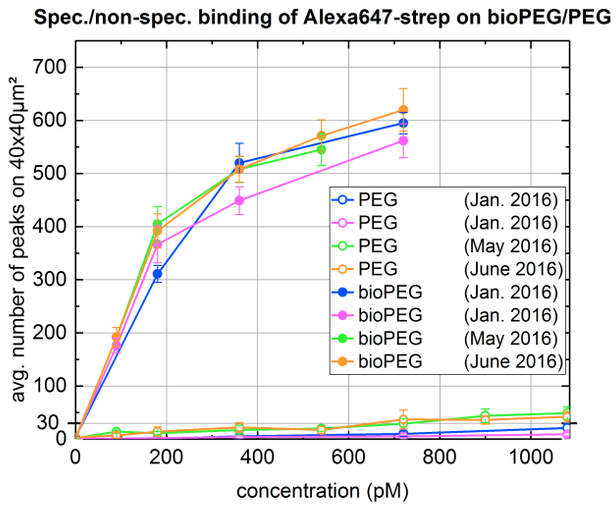

FIGURE 7.4: The blocking- and binding-curves of Alexa647-streptavidin over a six-month period

Having tested the blocking performance of the PEG-slide, the same measurement was repeated with a bioPEG-slide from the same batch, to make a statement about the specificity of the binding. At a ratio of $1 : 10^4$ of bioPEG to PEG, the number of detected peaks increase fast at low concentrations of added streptavidin, leading to the conclusion that the specific binding of the streptavidin is effective. Figure 7.4 shows a number of binding tests with the concentration ranging from $90\,\mathrm{pM}$ up to $720\,\mathrm{pM}$. From the binding curves can be concluded that over 90% of streptavidin is bound specifically to the surface, the surface functionalization works effectively throughout the tested concentration range. Figure 7.5 shows an example of how the spot density increases with an increasing concentration of streptavidin on PEG and bioPEG. On the

upper panel -the PEG surface- the number of spots increases hardly at all, compared to the lower panel with the bioPEG surface. At $720\,\mathrm{pM}$, it becomes difficult to distinguish the separate signals.

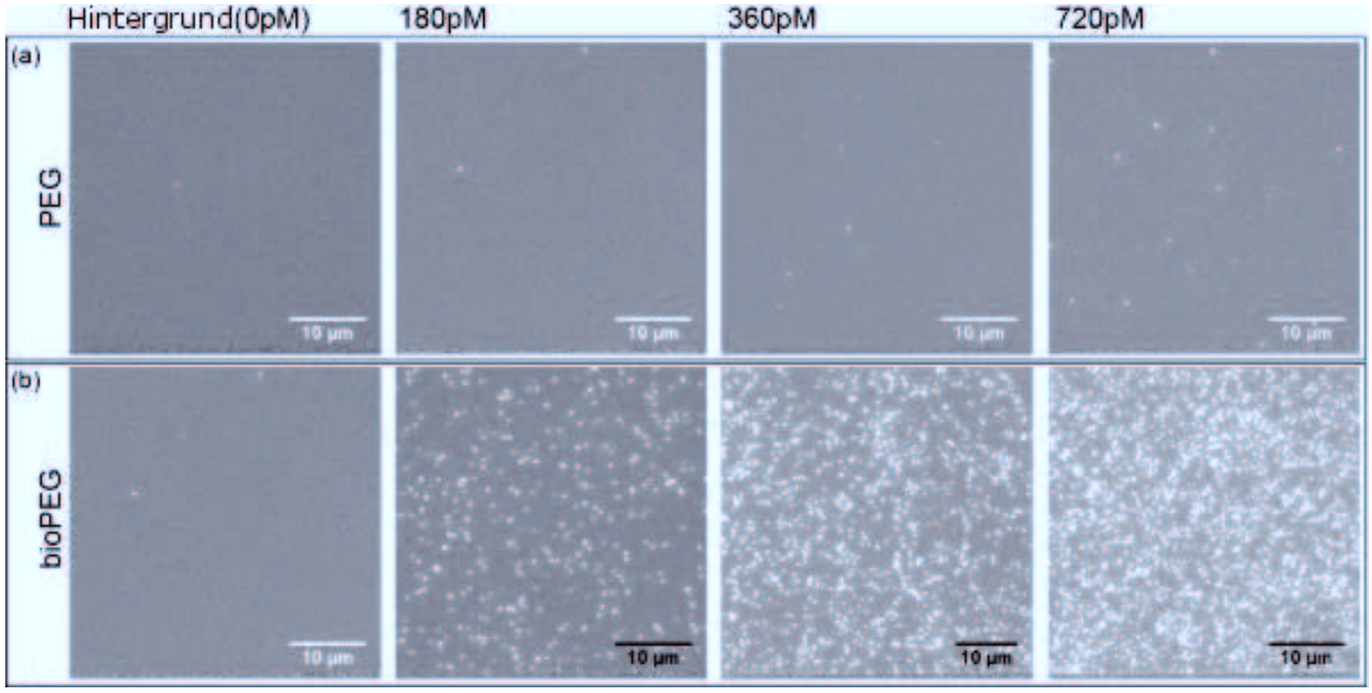

FIGURE 7.5: Surface areas imaged with different concentrations of Alexa647-labeled streptavidin that is either attached non-specifically to PEG (a), or specifically bound to the biotin anchors of the bioPEG slides (b).

7.5 Testing the linker accessibility with Atto655-conjugated biotin

The molecule of interest will bind specifically to the surface via biotin-neutravidin bond. Neutravidin with its four binding sites per protein molecule acts as a linker between the biotin anchors of the PEG surface and the biotinylated molecule of interest.

The number of accessible neutravidin linkers, at different concentrations, was tested with Atto655-biotin (Atto-tec, Germany):
The neutravidin stock solution (prepared from lyophilized, salt-free NeutrAvidin, VWR, Germany) was diluted to a certain concentration and injected to the sample channel, the unbound neutravidin was rinsed off after $40\,\mathrm{s}$ with $3\,\mathrm{ml}$ of Tico buffer. An increasing concentration of Atto655-conjugated biotin was injected and again the unbound excess was rinsed off after $40\,\mathrm{s}$. Consecutive areas were imaged to estimate the number of occupied neutravidin linkers at this concentration of neutravidin and Atto655-biotin. The procedure was repeated for increasing concentrations of neutravidin, as well as Atto655-biotin. For comparison, the same procedure was repeated in channel 2 of the same slide sandwich, without having added the neutravidin. The result in shown in figure 7.6. The figure shows that the specific binding via neutravidin linker is

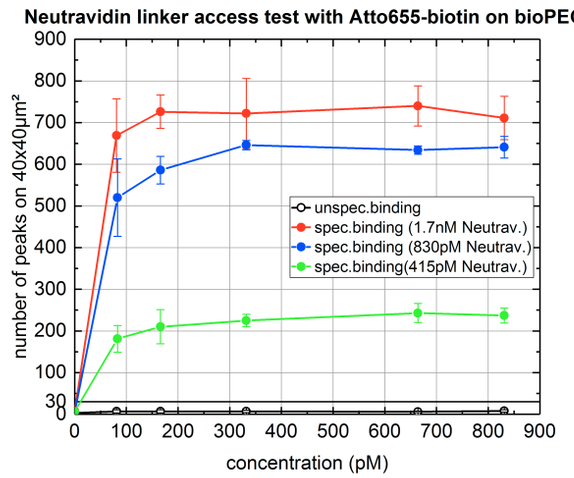

FIGURE 7.6: The specific-binding curve of Atto655 conjugated biotin with different employed neutravidin concentrations. The non-specific binding curve is shown for comparison

effective. The number of peaks detected in the second channel stays below the blocking limit for any concentration tested. It can be seen that for each neutravidin concentration, the accessible number of neutravidin linkers are occupied at low concentrations already, a further addition of Atto655-biotin does not increase the number of detected peaks.

According to the figure, the number of accessible binding sites can therefor be set by changing the neutravidin concentration. For the most part, the neutravidin concentration used was $1.7\,\mathrm{nM}$.

7.6 Testing the slide performance with Cy5-multilabeled bioCAN-ribosomes and GFPem

In anticipation of the colocalization measurements presented in the following chapter, the slides' blocking and binding performance was also tested with biotinylated Cy5 multi-labeled ribosomes and non-biotinylated GFPem. Before testing the slide's blocking and binding performance, an FCS measurement was made to ensure there are no aggregates (the diffusion coefficient for ribosomes should be close to approximately $22\,\mu\mathrm{m}^2/\mathrm{s}$ and approximately $120\,\mu\mathrm{m}^2/\mathrm{s}$ for GFP) and that the labeling reaction with Cy5-NHS was successful. An example of an FCS measurement for ribosomes is shown in figure 4.13 on page 39. The further proceeding was analogous to the slide tests done with Alexa647-streptavidin. The specific binding was tested using $1.7\,\mathrm{nM}$ of Neutravidin as a coupling layer between the biotin anchors at the surface and the biotinylated ribosomes. The measurement results are shown in figure 7.7.

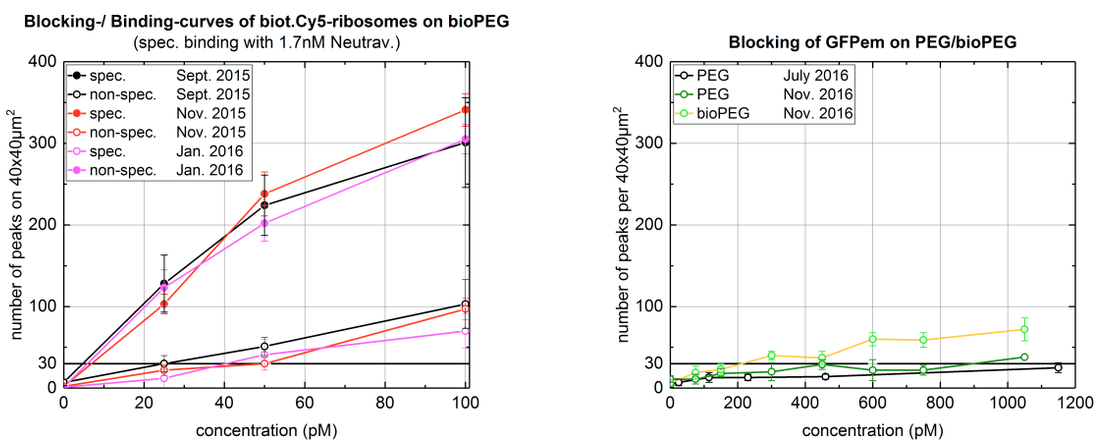

(A) (B) Single GFP emerald imaged on the surface

FIGURE 7.7: Blocking and specific binding of biotinylated Cy5-labeled ribosomes and blocking curves of GFPem on PEG and bioPEG.

7.7 Observations and comments

Due to the much higher non-specific binding rate of ribosomes, compared to the standard sample Alexa647-streptavidin, the high binding specificity of streptavidin to the bioPEG slides cannot be reproduced. The blocking limit

with bioPEG is reached for ribosomes already at concentrations as low as approximately $50\,\mathrm{pM}$. At an added concentration of $50\,\mathrm{pM}$ ribosomes, the binding ratio is 5:1. 20% of the ribosomes are bound unspecifically to the surface. The PEG- and bioPEG-slides prevent the unspecific binding of GFPem up to approximately $200\,\mathrm{pM}$. GFPem is less critical here; in the context of the studied CFPS system on the surface, the theoretically expected GFPem concentration is not more than $50\,\mathrm{pM}$. At that concentration, the number of GFPem should be lower than the number of background spots in the GFP-channel.
The limiting factor in the case of ribosomes is the surface's limited blocking capability for comparatively low concentration of ribosomes. A two-round PEGylation protocol is proposed in the literature [118], that may improve the passivation performance of the surfaces by filling eventual holes in the 'PEG'-carpet with a PEG of a lower molecular weight. The protocol has been tested to compliment the presented protocol, but the improvement in blocking performance was not statistically significant and therefore not continued.

Chapter 8

Results: Observing functional ribosomes on single-molecule level

8.1 Introduction: Colocalization measurements on the surface

The preceding chapters 6 and 7 presented the measurements, that were done to reliably image single fluorophores, and introduced the cover slide protocol to bind a fluorescent sample to the surface, while maintaining its functionality. During the simultaneous dual-color measurements, presented in the following, the WFM was employed as a tool, to detect and quantify single and rare events within a surface-bound sample, in order to answer biologically relevant questions.

8.2 Preliminary measurements with double-labeled DNA

The fraction of double-labeled molecules within a sample can be quantified by means of dual-color imaging, where a double-labeled molecule on the surface will lead to a colocalized signal in both color channels. Due to their high SNR and photo-stability, the first dual-color measurements were done with TS bead slides, during the alignment of the setup. On single-molecule level however, a test sample was needed with characteristics closer to the later measured real sample, to point out eventual additional challenges not encountered when imaging TS beads. The tested sample was a double-labeled DNA-strand that was labeled with one Alexa488 and one Alexa647 dye at the opposing ends of the strand (chapter 3).

8.2.1 Measurement

The imaged DNA did not have a biotin anchor and was therefore bound unspecifically to a plasma cleaned surface. A concentration of $25\,\mathrm{nM}$ of double-labeled DNA in DNA imaging buffer (chapter 3) was injected to the imaging chamber and allowed to absorb to the glass surface for $10\,\mathrm{min}$. Plasma-cleaned slides were chosen, due to their negligible number of dirt spots in either color channel, that could be mistaken for a signal peak. The unbound DNA was

rinsed off with $3\,\mathrm{ml}$ of buffer, resulting in a density of approximately 150 spots per area of $40\,\mu\mathrm{m} \times 40\,\mu\mathrm{m}$. To minimize photo-blinking and bleaching, the PCD-photoprotection system, as well as Trolox, had been added to the buffer. A representative number of areas all over the surface were imaged, collecting over 2000 signals in each channel. A TCCD measurement [1] of the same sample was done in parallel, to compare the results of the colocalization measurements on the surface with the coincidence-measurements in solution and to discuss the differences.

8.2.2 Data analysis

The analysis routine provided the number of signal peaks in both channels, as well as the number of colocalizations. The fraction of fluorescence signals, that have a corresponding partner in the complementary imaging channel, were determined, according to

$$\mathrm{Col}_{\mathrm{Red,Green}} = \frac{\sum \mathrm{colocalizations}}{\sum \mathrm{signals}_{\mathrm{Red,Green}}}. \tag{8.1}$$

Figure 8.1 shows an example of the recorded areas, the colocalized signals have been marked by the yellow circles.

8.2.3 Results and comments

Table 8.1 lists the results from the data analysis. The fraction of colocalized signals was expected to be high, considering the manufacturer's claim that the DNA should be mostly double-labeled.

TABLE 8.1: Results from the surface measurements

	avg. # of peaks per $40\,\mu\mathrm{m} \times 40\,\mu\mathrm{m}$	$\mathrm{Col}_{\mathrm{Red,Green}}(\%)$
Alexa488	146 ± 32	68±3 %
Alexa647	138 ± 27	73±4 %

In general, the number of fluorescent peaks on the surface is very similar in both channels. Between 68% and 73% of the fluorescence peaks are colocalized, meaning they have a corresponding partner in the complementary signal channel. The result is lower than expected, for comparison, the results from the TCCD measurements lead to a coincidence of 80% for Alexa488 and 96% for Alexa647.

[1] data provided by Henning Höfig from I.Physikalisches Institut, AG Biophysik, RWTH Aachen

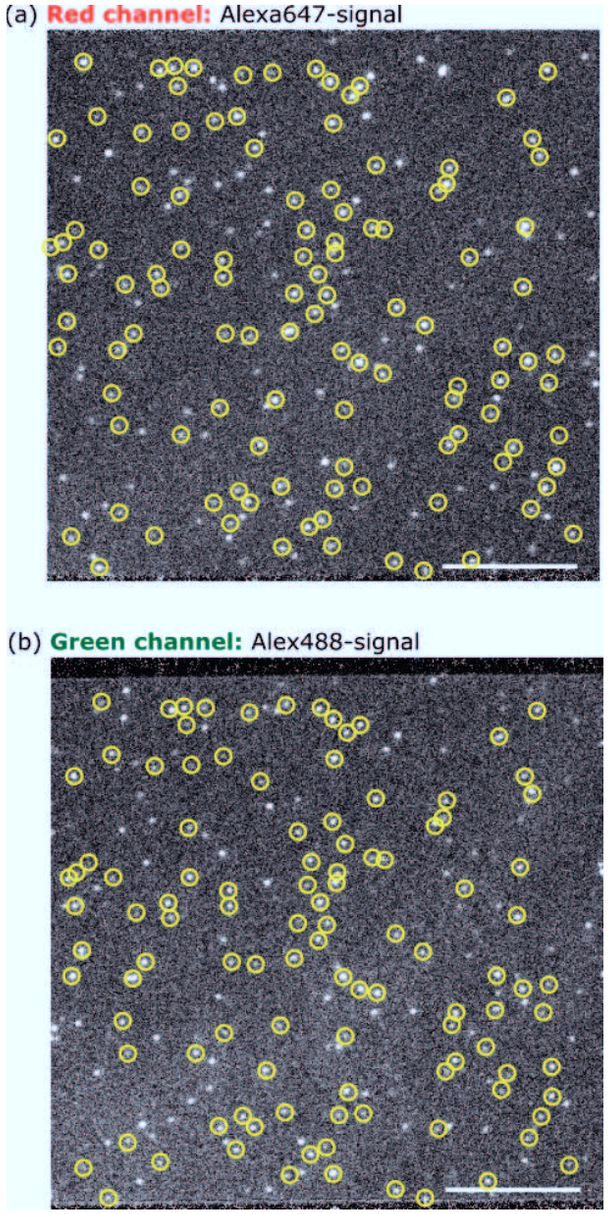

FIGURE 8.1: The red signal channel in (a) and the corresponding green channel in (b) of an imaged $40\,\mu\mathrm{m} \times 40\,\mu\mathrm{m}$ area, stained with double-labeled DNA. The colocalizations are marked by the yellow circles.

The discrepancy is possibly the result of differing measurement conditions. In the case of a TCCD measurement, the fraction of coincidence is limited by the a non-optimal overlap of the confocal volumes in both colors, as well as

possible photobleaching, due to the much higher excitation intensities within the confocal volume, while on the surface, the fraction of colocalized signals in this particular case may be limited, due to quenching effects. Since the DNA strands are adsorbed to the plasma cleaned surface, the dye may be in direct proximity of the surface, that could result in a substantial decrease or loss of fluorescence.

Nonetheless, the measurement shows the possibility to perform simultaneous dual-color measurements on single-molecule level with the WFM, that give quantifiable results.

8.3 Surface measurements of GFPem synthesized by exogenous modified ribosomes

8.3.1 Introduction to the project

Within the framework of a cell-free protein synthesis on single ribosome-level, the objective of the surface measurements was, on one hand, to determine the fraction of active ribosomes and on the other hand, to make a statement about the stalling efficiency of the construct, that keeps the GFPem bound to the ribosome after its synthesis [54]. Whereas an ensemble measurement could only provide the ratio of synthesized GFPem over the amount of ribosomes, simultaneous dual-color imaging on single ribosome level gives a direct insight on the fraction of active ribosomes bound to the surface, that have produced a GFPem, as well as how many of the imaged GFPem signals are colocalized to a ribosome signal in the red channel and hence, determine the stalling efficiency of the construct. Figure 8.2 represents a biotinylated Cy5-labeled ribosome with the synthesized and bound GFPem.

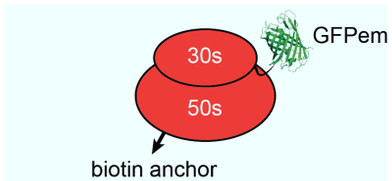

FIGURE 8.2: Depiction of a bioCAN 20/12E ribosome with the synthesized GFPem. Both subunits are labeled unspecifically with Cy5 (NHS-ester), the biotin anchor is attached to the 50S subunit. The GFPem remains bound after synthesis due to the SecMstr construct.

In a first part, the GFPem synthesis by biotinylated and Cy5-labeled ribosomes was done *in vitro*. The diluted reaction mixture of the *in vitro* experiment was brought to the surface of a plasma cleaned cover slide, where the three different populations (the ribosomes with and without bound GFPem and the free GFPem[2]) should adsorb to. The different populations were quantified, the results were then compared to the results of two other independent methods,

[2]Qualitative measurements were done to verify that the very low concentrations of GFPem contained in the injected sample solution could bind to the surface of plasma cleaned cover slides

that were run in parallel with the same sample (TCCD and co-precipitation). The ribosomes from the *in vitro* experiment were also attached specifically to the functionalized PEG cover slides (as presented in chapter 6). The fraction of colocalized signals in the GFPem channel should be potentially higher, compared to the previous measurements on the plasma cleaned slides, since the unbound GFPem is blocked by the passivated cover slide surface. Finally, an *in situ* measurement was done. The GFPem was synthesized by the specifically tethered ribosomes on the surface and the increase of GFPem was monitored over time.

8.3.2 Negative controls

Preliminary measurements were required before the *in vitro* measurements could take place. These were the negative controls of the experiment, done to ensure that the colocalized signals originate from the synthesized GFPem bound to the ribosome and are not artifacts. It is clear that, neither the Cy5-labeled ribosomes, nor the GFPem should emit a detectable signal in both of the imaging channels, that could be mistaken for a colocalization. This was verified during the optimization of the imaging parameters (in the case of GFPem) and the testing of the cover slide functionalization with the Cy5-labeled ribosomes. Another potential source for a false positive colocalization is the *in vitro* protein synthesis kit PURE express (chapter 3). Therefore, the ribosomes (approximately $50\,\mathrm{pM}$) with the added PURE express kit ($5.5\,\mathrm{nM}$) were imaged on the surface. A number of different areas within the imaging channel were recorded, to ensure there were no detectable signals in the GFPem channel. An example of the dual-color measurement is shown in figure 8.3:
While the upper part of the left panel (the red channel) shows a good density of Cy5-labeled ribosomes, the corresponding green channel is nearly empty, proving that the expression kit did not introduce a signal, that could be mistaken for GFPem. For comparison, an example taken from the *in vitro* CFPS experiment (presented in the following section) is shown in the right panel: the upper channel shows again the signals from the labeled ribosomes, while the corresponding area in green channel shows a typical density of GFPem signals.

8.3.3 Measurements with the confocal microscope and co-precipitation

FCS and TCCD measurements

As introduced in chapter 3, a preliminary FCS measurement of the sample allowed to make a qualitative statement about the success of the *in vitro* reaction before starting the surface measurement, as a GFPem's measured diffusion coefficient close to the ribosome's indicated, that a major fraction of GFPem is bound to the ribosome (compare with figure 4.13 on page 39).

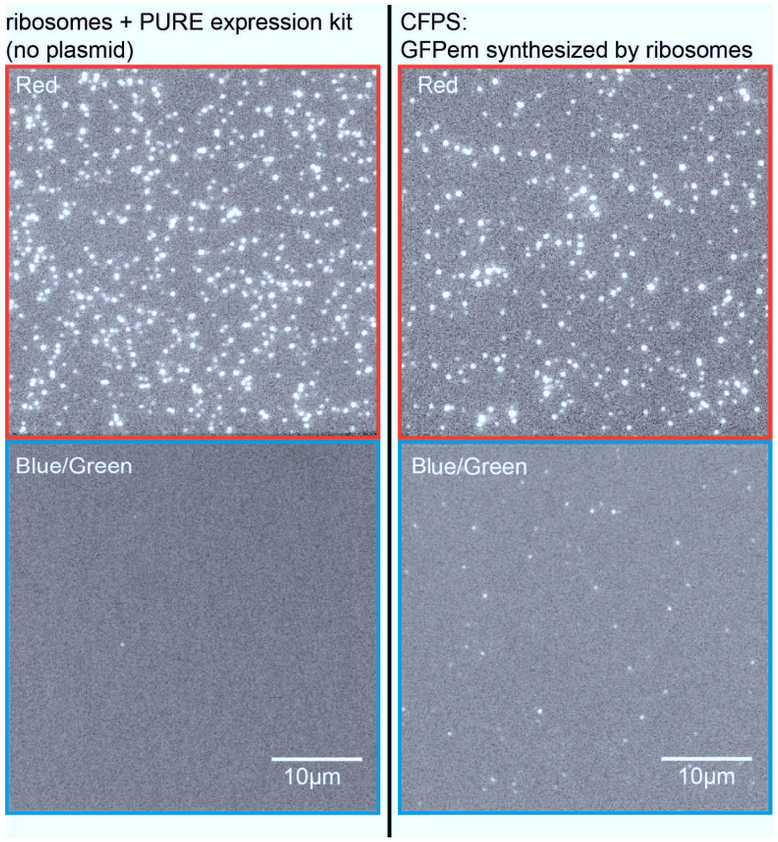

FIGURE 8.3: Two $40\,\mu\mathrm{m} \times 40\,\mu\mathrm{m}$ areas with unspecifically bound Cy5-labeled ribosomes on a plasma cleaned surface with the PURE express kit only in the left band and the synthesized GFPem in the right band. The upper red boxes represent the red channels with the Cy5-signals of the ribosomes and the lower blue boxes represent the green channel of the same area with the signal originating from the PURE express kit (left) and the GFPem signal on the right.

Quantitatively, the fractions of free GFPem and bound GFPem were determined on single-molecule level by a two-color coincidence detection (TCCD) measurement. The TCCD[3] measurements were done with a highly diluted two-color sample (on average less than 0.01 molecule in the confocal volume at one time to avoid a false positive coincidence due to the proximity of the molecules in solution) and two synchronized pulsed lasers to excite the confocal volume. The fraction of simultaneously recorded (coincident) intensity bursts in both color channels represent the fraction of two-colored molecules within the sample (in this case GFPem bound to a ribosome).

[3] data provided by Dr. Noémie Kempf, ICS-5: Molecular Biophysics, FZ Jülich

Co-precipitation measurements

During the co-precipitation experiment[4], the reaction mixture was layered onto $1.1\,\mathrm{M}$ sucrose in Tico-buffer and centrifuged at 110000 x g for $2.5\,\mathrm{h}$. By centrifugation, the heavier ribosomes will be separated from the free GFPem. Whereas the ribosomes will form a pellet, the free GFPem will stay in the supernatant. After resuspending the pellet in Tico buffer, the concentration of the ribosomes will be determined by absorption at $260\,\mathrm{nm}$. The GFPem concentration from both, the resuspended pellet and the supernatant, were determined by fluorescence spectroscopy and allowed to determine the fraction of free and bound GFPem, to make a statement about the fraction of active ribosomes and the efficiency of the SecMstr construct.

8.3.4 *In vitro* measurement on plasma cleaned glass slides

For a start, the diluted reaction mixture was imaged on a plasma cleaned surface, which can be compared to a snapshot of the reaction mixture contents: lacking the passivation of the PEG-slides to reduce unspecific binding of proteins, the ribosomes, as well as the GFP, should stick integrally to the cover slide surface.

Before adding the reaction mixture, the slide's background was imaged with Tico-buffer in both color channels. A plasma cleaned slide displayed a negligibly small number of peaks that could be mistaken for a GFP signal in green. Together with the added O_2-scavenger, the number of introduced background peaks was in general found to be 2 ± 1 on an imaged area of $40\,\mu\mathrm{m} \times 40\,\mu\mathrm{m}$, which corresponds to less than 10% of the later expected amount of GFPem on that area and was considered negligible.

In analogy to the negative controls, the reaction mixture was diluted in Tico-buffer to a ribosome-concentration below $50\,\mathrm{pM}$. After the injection of a volume of $1\,\mathrm{ml}$ of the solution to the imaging chamber and an incubation time of one minute, the unbound ribosomes were removed by flushing the imaging channel with $3\,\mathrm{ml}$ of buffer, resulting in a density of approximately 250 ribosomes on an area of $40\,\mu\mathrm{m} \times 40\,\mu\mathrm{m}$. After having replaced the buffer with Tico-buffer, where the O_2-scavenger GOC, as well as Trolox had been added, the image acquisition started.

The mentioned ribosome density of approximately 250 per $40\,\mu\mathrm{m} \times 40\,\mu\mathrm{m}$ appeared to be a good compromise:
the number of detected GFPem signals ranged within approximately 40-50 peaks (assuming a constant ribosome density throughout), leading to relatively constant values for the activity and stalling efficiency within the accumulated set of images. Yet, at a density of 250 per $40\,\mu\mathrm{m} \times 40\,\mu\mathrm{m}$, the ribosomes are still well isolated from each other, making it easy to discern single signals in the red channel, but also to attribute an eventual GFPem signal in the green channel to the corresponding ribosome signal. An example of an imaged is shown in figure 8.4.

[4]The co-precipitation data was provided by Dr. Alexandros Katranidis from ICS-5: Molecular Biophysics, FZ Jülich

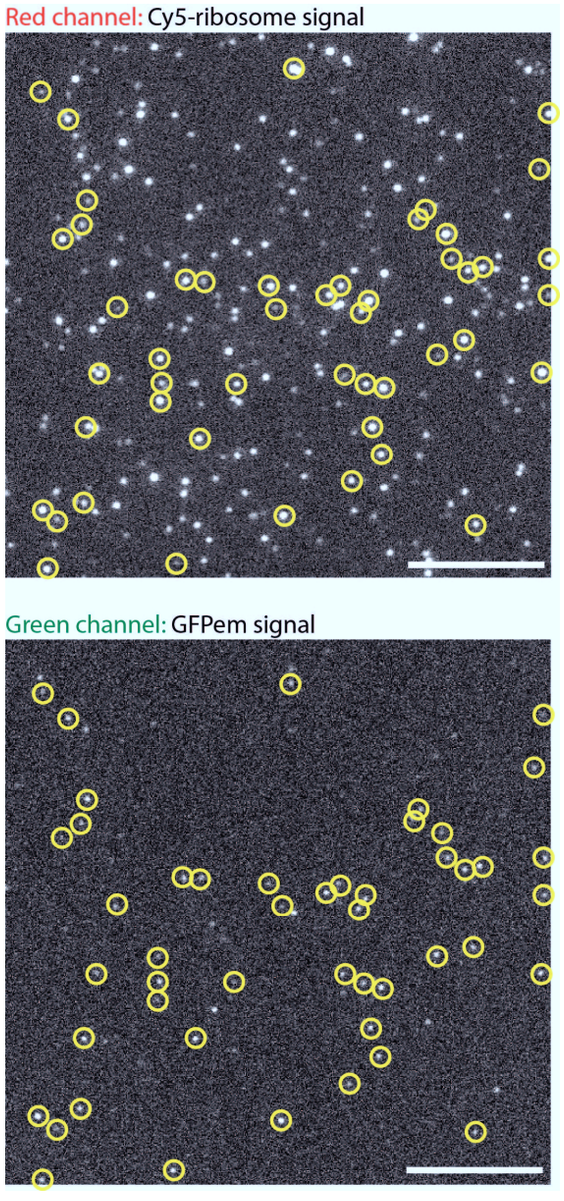

FIGURE 8.4: An example of the images from the colocalization measurements, done with Cy5-labeled bioCAN ribosomes, that have synthesized GFPem in vitro: The colocalized signals are marked with the yellow rings. The length of the scalebar is $10\,\mu\mathrm{m}$.

Care was taken to prevent an eventual early photodestruction of the GFPem that could result in a lower determined activity of the sample. Thus, image acquisition was done in one direction only, over the area of the imaging chamber.

Depending on the homogeneity of the ribosome density, more than a dozen areas were imaged, collecting the signals of more than 3000 ribosomes and 500 GFPem.

8.3.5 Data analysis and results

Data analysis provided the number of detected ribosomes, as well as the number of detected GFP and colocalized signals per processed image. The average values for the fraction of active ribosomes and the stalling efficiency of the plasmid were determined as follows

$$\text{activity} = \frac{\sum \text{colocalizations}}{\sum \text{ribosomes}} \tag{8.2}$$

$$\text{stalling efficiency} = \frac{\sum \text{colocalizations}}{\sum \text{GFPem}} \tag{8.3}$$

By repeating the *in vitro* synthesis five times under equal conditions, the results from the surface measurements could be compared to the two other methods. The averaged results of the three methods are listed in table 8.3.

TABLE 8.2: Results from the three independent methods

method	activity (%)	stalling efficiency (%)
WFM	17.4 ± 3.3	85.0±5.9
TCCD	20.3 ± 7.7	84.7±6.5
co-prec.	21.2 ± 3.8	93.6±4.7

By comparing the results from the three different methods, a good agreement within their respective errors is shown, validating the surface imaging as an independent method, to retrieve information from a sample on single-molecule level.

A critical factor, that influences the results on the surface, is the premature photobleaching of the components. Photobleaching impacts both the determined number for the ribosome activity, as well as for the construct's stalling efficiency. While the employed photoprotection system results in a photostable fluorescence signal of the Cy5-labeled ribosomes (in other words, the stalling efficiency should not be impacted), excessive exposition to excitation light must be avoided for GFPem, since an invisible GFPem will lead to an apparently lower ribosome activity.

Although, the sample is just like in the previous section adsorbed unspecifically to the surface, the interactions happening at the surface between the sample and the surface itself seem to have a much reduced influence on the determined values for the activity and stalling efficiency, as compared to the case of the DNA. The reasons may be on one hand the protective beta-barrel structure of the GFPem, that may hinder a possible quenching on the surface, as well as the multiple Cy5-labels of the ribosomes.

8.4 Measurements on bioPEG-slides

8.4.1 *In vitro* measurement

During the *in situ* measurement, the biotinylated ribosomes will be tethered to the biotin anchors of the bioPEG-slide's surface via Neutravidin linkers (see chapter 6), in order to maintain the ribosomes' functionality. Preliminary to the *in situ* measurement, the ribosomes with the bound GFPem, synthesized *in vitro*, were bound specifically to the bioPEG surface. In contrast to the plasma cleaned surface, which acted as a snapshot to image all the populations within the CFPS solution, the bioPEG surface (with the Neutravidin layer) should block the free GFPem at the employed low concentrations (according to the blocking test, presented in chapter 7), hence in the green channel, the only visible signals are coming from GFPem, that are bound to ribosomes.

A typical density of approximately 250 ribosomes per $40\,\mu\mathrm{m} \times 40\,\mu\mathrm{m}$ is achieved by injecting a $50\,\mathrm{pM}$ solution of ribosomes into the imaging channel. From the TCCD measurements is known that, within the CFPS solution, approximately 15% of the total amount of GFPem, present in the solution, is free GFP.

TABLE 8.3: Results of the in vitro measurement on bioPEG

#BG R/G	# ribos	# GFPem	# colocs	frac. col. GFPem(%)	frac. col.ribos(%)
3±2/6±3	231±16	46±12	40±10	**88±4**	17±4

By comparing the fraction of colocalized signals in the green channel from the specific binding on the biotinylated PEG slides to the unspecific binding of the plasma cleaned slides (presented in the previous section), a slight increase to 88% versus 85% was observed. The limiting factor here is the number of background spots in the green channel (GFPem): A passivated surface, free of background spots, should lead to images where nearly 100% of the GFPem peaks have a complementary partner in the ribosome channel. The average number of background spots in both channels was determined from the previously recorded background images with only the buffer added. The analysis allowed to estimate the fraction of colocalized background spots, that could be mistaken from the actual signal spots.

8.4.2 *In situ* measurement

The next step of the CFPS experiments was the *in situ* synthesis of GFPem by ribosomes on the surface. As described in the previous section, the biotinylated Cy5-labeled ribosomes were specifically attached to the surface's biotin anchors by a neutravidin linker, to achieve a density of approximately 250 ribosomes per $40\,\mu\mathrm{m} \times 40\,\mu\mathrm{m}$. The specific attachment should maintain the activity of the ribosomes. In addition to the *in vitro* measurement, the *in situ* measurement required the heating of the imaging chamber to a temperature of $37\,^{\circ}\mathrm{C}$, where the ribosomes display the highest activity. The heating of the chamber involved the change of the immersion oil, adapted to the imaging

at a temperature of $37\,^{\circ}\mathrm{C}$ (Zeiss Immersol $518\,\mathrm{F}/\ 37\,^{\circ}\mathrm{C}$). The heating of the imaging chamber was done by a pair of resistive heater elements, mounted to the chamber base (RC-30 Warner Instruments, Connecticut, USA), that was placed on the microscope stage. The chamber base accepted a cover slide size of $22\,\mu\mathrm{m} \times 40\,\mu\mathrm{m}$. The shape of the imaging chamber cutout was modified (as compared to figure 7.2) to account for the reaction mix volume, scaled up to $50\,\mu\mathrm{l}$, and the limited accessibility due to the heater base. A scheme is presented in figure 8.5. The temperature was monitored and controlled manually by a thermoresistor connected to a temperature controller (TC-324C by Warner Instruments), that was placed inside the imaging channel with the sample. Before starting the experiment, the temperature of the sample solution in the imaging channel was monitored for $30\,\mathrm{min}$ and corrected if necessary, until stabilization. After the reaction mix had been injected to the imaging channel, the imaging channel was closed with sticky tape, to avoid the evaporation of the solution.

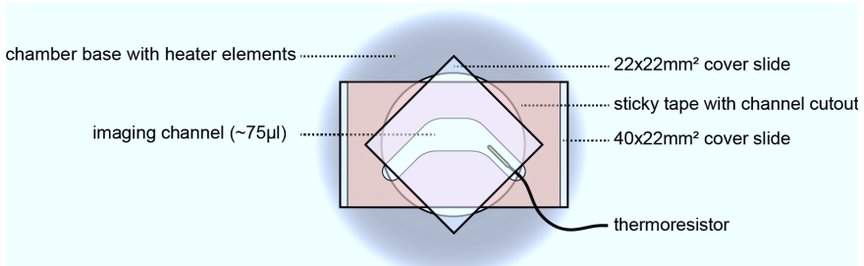

FIGURE 8.5: A sketch of the cover slide sandwich, mounted on top of the heated chamber base. The imaging chamber, with the thermoresistor necessary for the monitoring of the temperature inside the channel, had two openings, that were closed during the time-measurements.

The aim of the measurement was to observe the increase of synthesized GFPem over a time window of one hour. Starting from the number of background spots in the GFPem channel (which should be as small as possible) the number of determined fluorescent spots in the GFPem channel should increase with time. Since the SecMstr.-plasmid was used, the GFPem peaks should colocalize with a signal in the ribosome-channel. Oxygen is necessary for the protein synthesis, hence no photoprotection system was used during the measurement. Excessive illumination was avoided by changing the area to be imaged after each snapshot.

8.4.3 Results and comments

Figure 8.7 shows examples of $20\,\mu\mathrm{m} \times 20\,\mu\mathrm{m}$ sections of imaged areas from the *in situ* measurement. On the left panel, the tethered Cy5-ribosomes are shown, with the corresponding green channel of the same area on the right. The colocalized GFPem are marked by the yellow circles. The number of colocalizations increases over time as GFPem is synthesized by the ribosomes.

Figure 8.6 displays the trends for the determined fraction of active ribosomes and the fraction of stalled GFPem synthesized on the surface over the time of one hour. While the trend shows an increase over time in the fraction of active ribosomes, the reached level within one hour of consecutive measuring is below the level determined from corresponding *in vitro* measurements made in parallel. A number of reasons may contribute to the lower activity:

- reduced accessibility of the mix components on the surface as compared to the *in vitro* measurement,
- specifically bound ribosomes, that are oriented badly, may not produce a GFPem,
- approximately 20% of the ribosomes are not bound specifically to the surface (see chapter 7), resulting possibly in a lost activity,
- premature bleaching due to omitted O_2-scavenger,
- limited temperature stability inside the imaging chamber.

The stalling curve shows that a high fraction of the signals in the green channel are colocalized. Considering that the wast majority of background spots are not colocalized, the stalling indicates that the observed signals in the green channel are colocalized GFPem.

Throughout the measurement, the temperature inside the imaging chamber was monitored. The heating was not trivial, it required the closing of the chamber openings to minimize evaporation of the solution. Furthermore, a change in temperature came with a change of the focus position (the refractive index of the immersion oil is temperature dependent), requiring a constant correction of the the focal position along the z-axis.

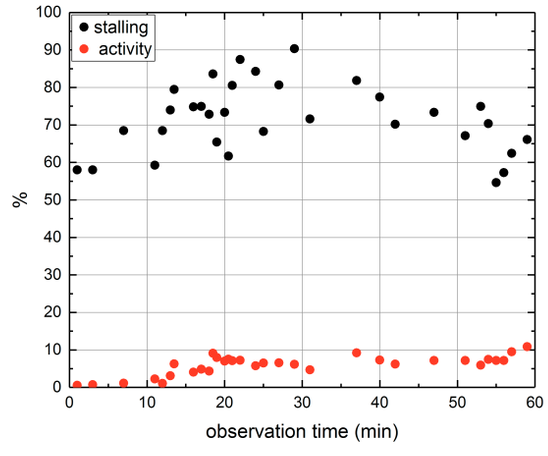

FIGURE 8.6: The determined trend of active ribosomes and the corresponding fraction of bound GFPem, as recorded over 60 min.

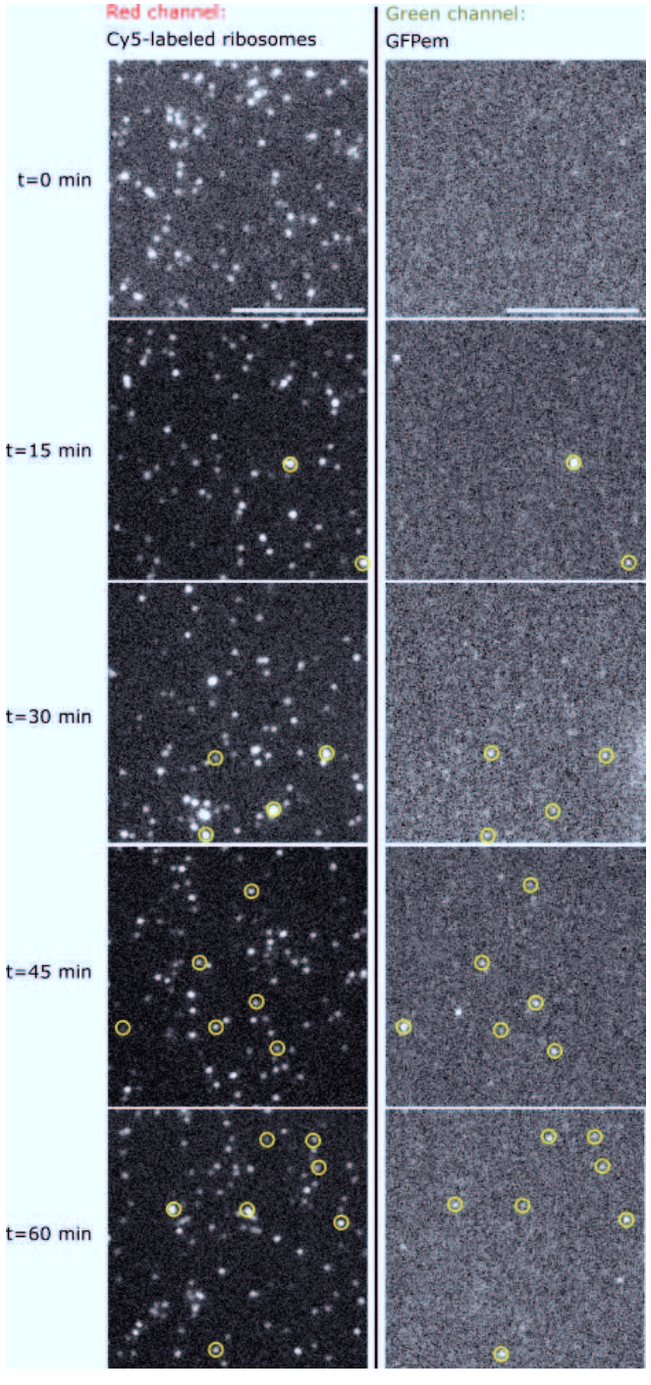

FIGURE 8.7: An strip of different areas taken from the *in situ* measurement. The left band shows the red channel with the ribosomes, the right band shows the corresponding green channel with the GFPem signals. The colocalizations are marked by the yellow circles. The length of the scale bar is $10\,\mu\mathrm{m}$.

8.5 Re-associated ribosomes

Within a study concerning the ribosomes' stability at picomolar concentrations, single re-associated 70S ribosomes were bound to the surface to determine if they remained stable during the time window of the measurement. In this case, the studied ribosomes had been labeled specifically with a Cy3-oligonucleotide hybridized to the 30S subunit and a Cy5-oligonucleotide to the 50S subunit respectively (see chapter 3). The complex formed by the oligonucleotide and the respective subunit leads to a dissociation constant k_d of $5\,\mathrm{nM}$. Since the ribosome solution will be added to the imaging channel at a concentration much lower than k_d, they will eventually dissociate. On the surface, dissociation becomes visible by a decrease in the fraction of colocalized peaks. In a first step, control-measurements on the surface were done to verify how long the oligonucleotide with the dye remained attached to the respective subunit. Having determined the time window, where the oligonuclotides remain bound to the subunits, the then re-associated ribosomes were bound to the PEG surface to monitor, if the fraction of colocalized signals changes over the previously determined time window.

8.5.1 The measurements

The subunits did not have a biotin anchor and were bound unspecifically to the PEG-surface. To achieve a reasonable density of peaks on the surface, a solution of $2.5\,\mathrm{nM}$ was injected to the imaging chamber. After an incubation time of $40\,\mathrm{s}$, the unbound subunits were rinsed off with $3\,\mathrm{ml}$ of Polytris buffer, resulting in a density of approximately 300 spots per $40\,\mu\mathrm{m} \times 40\,\mu\mathrm{m}$. To minimize photobleaching and blinking of the single dyes, the PCD-photoprotection system and Trolox were added to the imaging buffer before the measurement took place. While the adsorbed subunits should remain bound to the surface, the labeled oligonucleotides will possibly detach from the subunits with time. The advantage of a surface measurement here is that the fraction of subunits, where the oligonucleotide with the respective dye has detached, can be monitored over time. The detached oligonucleotides do not adsorb to the passivated surface at these low concentrations. Swimming in the solution (out of focus), they become invisible. To determine how long on average the oligonucleotide remains attached to the subunit at these concentrations, consequent imaging of consecutive areas at different incubation times was done for two hours.

8.5.2 Results

During data analysis, the average number of peaks on a $40\,\mu\mathrm{m} \times 40\,\mu\mathrm{m}$ area versus observation time was determined. The results for both subunits is illustrated in figure 8.8. Each measuring point is determined from the average number of spots from approximately 15 consecutively imaged areas. The error bars represent the distribution's standard deviation. The average number of Cy5-oligonucleotide hybridized to the 50S-subunit decreased by approximately 10% after one hour and by 20% after two hours. In the case of the Cy3-30S subunit, it was observed that, while there was a certain variation in the number of spots within one measurement time, overall the average number of

spots did not decrease over the course of two hours, indicating that the Cy3-oligonucleotide remains bound to the subunit. In combination, colocalization experiments with both labeled subunits should not exceed the duration of one hour if a reliable quantification is requested.

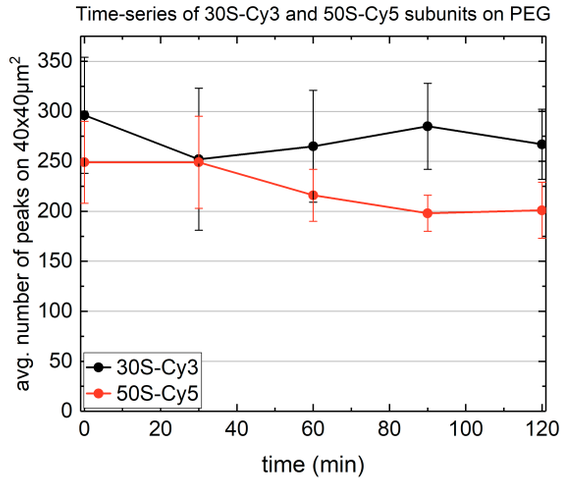

FIGURE 8.8: The trend of the average number of peaks detected versus time for the 30S-Cy3 as well as the 50S-Cy5 subunit.

8.5.3 Stability of the re-associated ribosomes

In the next step, the now re-associated ribosomes were bound unspecifically to the passivated slide surface. After having imaged the cover slide background, to verify that the number of background spots is small enough compared to the number of adsorbed ribosomes, a concentration of $500\,\mathrm{pM}$ of re-associated ribosomes was injected into the imaging channel, resulting in a density of approximately 150 peaks per $40\,\mu\mathrm{m} \times 40\,\mu\mathrm{m}$, after having rinsed the imaging channel after $40\,\mathrm{s}$ with $3\,\mathrm{ml}$ of Polytris-buffer. The surface was then imaged during $1\,\mathrm{h}$, the previously time window, where the oligonucleotides remained attached to the subunits. The goal was to determine, if a potential decrease in the fraction of colocalized signals, resulting from the eventually dissociating ribosomes, occurs within the determined time of stability.

8.5.4 Results and comments

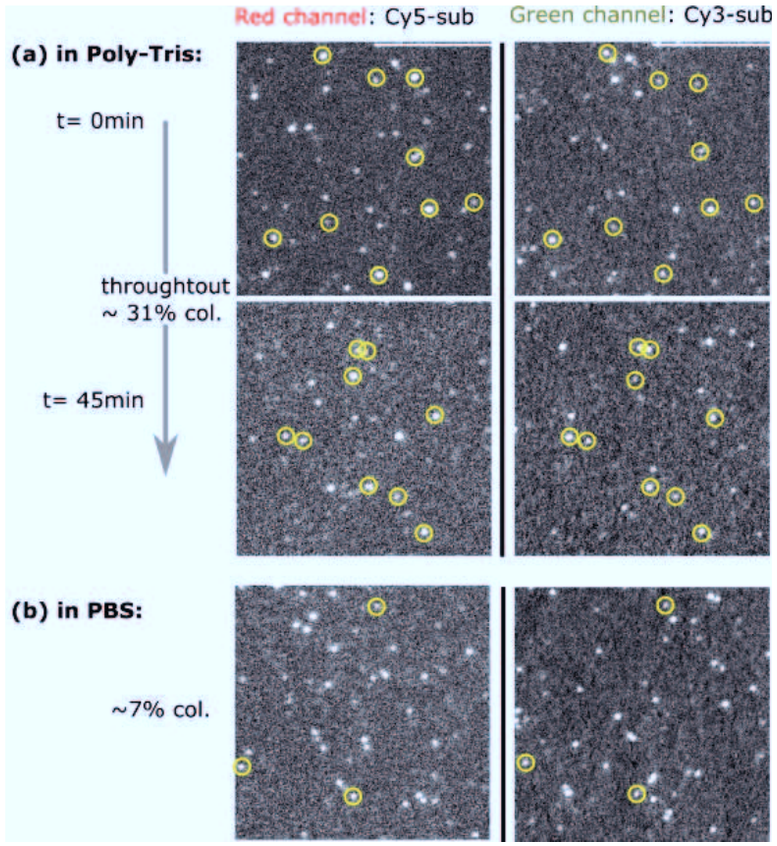

FIGURE 8.9: An representative example of the measurements with the re-associated ribosomes bound to the surface in Poly-Tris buffer imaged within the time window of $45\,\mathrm{min}$ (a) and an example taken from the negative control imaged with PBS in (b). The colocalized signals are marked by the yellow circles. Length of the scale bar $10\,\mu\mathrm{m}$.

Figure 8.9 (a) shows two examples of the recorded images, at the start of the measurement and towards the end, after $45\,\mathrm{min}$. The colocalized signals are marked again by the yellow circles. While the total number of identified peaks showed a certain degree of variation from area to area, which may have been the result of an irregular PEGylation of the surface, the fraction of colocalized signals was determined to be $31 \pm 3\%$ and remained constant throughout the measurement. The dual-color experiment was repeated with PBS buffer, instead of Poly-Tris. The lack of Mg^{2+} leads to a dissociation of the ribosomes. Brought to the surface, a clear difference compared to the previous measurement became visible, the fraction of colocalized signals was determined to be 7%, as opposed to 31%, when diluted and imaged in Poly-Tris buffer. An example of the recorded images is given in figure 8.9 (b).

The measurements on the surface were complimented by TCCD measurements in solution, done in parallel[5], to determine up to which time interval the subunits remained re-associated, before a noticeable decrease in coincidence occurs, due to presumable dissociation of the subunits.

The control measurement with PBS buffer resulted in a fraction of coincident signals below 5%, confirming the result from the surface measurement.
In the case of the measurement with Poly-Tris buffer although, the initial fraction of coincidence ranged from 22-24%. The fraction of coincidence dropped below 20% after 20 min, an indication that the ribosomes may dissociate. Contrary to the TCCD measurement in solution, this was not observed on the surface. On one hand, the slightly different measurement conditions in solution may lead to an earlier dissociation in solution. On the other hand, it may not be entirely excluded, that a fraction of the potentially dissociated ribosomes on the surface may not separate locally, the detached subunits may adsorb in proximity to each other, within the resolution-limit of the microscope and hence indiscernible from the undissociated ribosomes. Since, there was no notable decrease in the fraction of colocalized signals throughout the measurement though, this seems unlikely.

[5] by Dr. Noémie Kempf

Chapter 9

Conclusions

9.1 Imaging on single-molecule level

This thesis describes in first place the parameter optimization to image single fluorophores on the surface with a WFM, to subsequently employ the WFM as an independent tool, to identify and quantify single and rare events within a fluorescently labeled biological sample, that is tethered to the surface of a functionalized glass cover slide.

Preliminary measurements were done to assess the excitation intensity distribution at the available power ranges for the three different excitation lasers. By measuring the beam profiles near the surface of the cover slide, it was observed that the intensity variation within an imaged area is less than 5%, allowing the conclusion, that the excitation intensity is constant within the imaged area. The first measurements, done with the WFM, determined the resolution power of the setup within the three different spectral wavelengths and confirmed, that the setup is performing as expected.

Especially in low-light conditions, the optimization of imaging conditions is imperative for the reliable imaging and detection of single fluorophores and the subsequently conducted quantitative imaging on single-molecule level.

In short terms, the aim of the parameter optimization was to determine a set of imaging parameters that results in the collection of as many photons per fluorophore as possible, resulting in a high SNR. The relevant parameters, that govern the number of collected photons per fluorophore, are the illumination time and power. Both, the optimal illumination time and power for a fluorophore, depend on its photostability, and, in general, neither an excessive illumination time, nor power resulted necessarily in the highest SNR. Additionally, the application of the camera's EM-gain was tested, considering its impact on the fraction of fluorophores with a SNR$\leq$3, as well as on the the signals' E_{SNR}. The EM-gain impact was tested for each fluorophore separately. The results, considering the achieved SNR for a known number of recorded photons per fluorophore deviated from the theoretically expected values, as a result of the overall noise, that was higher than anticipated. It was evaluated for each type of fluorophore in particular, if an EM-gain application was advantageous or not. The finally chosen imaging parameters were the ones that lead to the highest fraction of signals with a SNR$\geq$3 and the arithmetic mean E_{SNR}. With the selected set of imaging parameters, the majority of the imaged fluorophores displayed a SNR$\geq$3 (between 86% and 94%), with an arithmetic mean E_{SNR} ranging from 4.8 up to 9.1. The determined values are in agreement with the SNR values commonly found in the literature.

The WFM was subsequently employed as a tool to perform quantitative measurements on the surface on single-molecule level. The procedure of the presented WFM measurements consisted in general of the imaging of a number of different areas, to get a representative overview of the homogeneity of the cover slide's surface. Due to the limited photostability of single fluorophores, it is advisable to limit excessive illumination to a minimum to prevent premature photobleaching. To increase a fluorophore's observation time, two photoprotection systems commonly employed were tested with time-series, regarding their impact on the observation time. Both photoprotection systems reduced photobleaching to a minimum for the Alexa Fluor and the Cyanine dyes. In combination with the employed imaging parameters, photobleaching became negligible, confirming the observations found in the literature [50]. The photoprotection systems' impact on the observation time of GFPem was small , compared to the fluorescent dyes. The strategy, that was adopted while imaging GFPem, was to prevent an excessive exposition to excitation light, by systematically changing the area to be imaged.

An essential part of the single-molecule imaging with the WFM is the surface preparation. The requirements on the surface were first of all a clean background, meaning a number of background signals below 10% of the to be expected number of imaged signal peaks in each color channel. Piranha and plasma cleaning of the cover slide resulted routinely in a surface with virtually no background signals in either color channel.

The surface functionalization protocol's goal was to offer on one hand binding sites, that allow the specific tethering of the molecule of interest without hindering its functionality, while at the same time prevent unspecific binding, that cold result in the denaturation of the sample. The surface of the glass cover slide has been passivated with a PEG carpet, specific tethering on the cover slide surface was allowed by the bioPEG, the biotinylated sample is then immobilized by a layer of neutravidin linkers. The achievable ratio of specific labeling was determined for each tested sample by binding curves. Repeated blocking and binding measurements for each sample confirm that the protocol is robust, the glass surface cleaning with piranha and plasma leads consistently to a surface background, that is clean enough to perform quantitative measurements on single-molecule level. Alexa647-streptavidin served as a standard to compare the reproducibility of the protocol over time. The ratio of bioPEG to PEG was selected to be $1{:}10^4$, leading to a specific binding ratio for the Alexa647-streptavidin $\geq$10, which was considered satisfactory. The specific binding ratio with multilabeled biotinylated ribosomes was lower ($\sim$ 5:1), limited by the higher affinity of the ribosomes to stick non-specifically to the surface. Tests with a lower weight PEG, to increase the blocking performance of the surface by filling potential gaps in the carpet, did not bring an improvement. Tests with BSA as a (additional) blocking agent were unsuccessful, due to the introduced background spots in the green/yellow channel that made the BSA useless for single-molecule measurements on the surface. While a higher binding ratio may be achieved by further increasing the ratio of the bioPEG:PEG mix brought to the surface, the surface is likely to be saturated at very low pM-concentrations, making it difficult to control the density of the bound ribosomes.

9.2 The WFM as a tool for quantitative surface measurements on single-molecule level

On the example of a CFPS study, the WFM was used to quantify the fraction of active ribosomes bound to the surface, as well as the stalling efficiency of the plasmid, that binds the GFPem to the ribosome after synthesis, by means of a simultaneous dual-color colocalization measurement. The comparison of the determined values from the *in vitro* measurements on the surface with the results from two different methods (TCCD and co-precipitation), that were carried out in parallel, revealed that the WFM gives very similar results repeatedly and hence demonstrates that, on one hand, the surface is clean enough to perform quantitative measurements on single-molecule level, while on the other hand, the measurement procedure does not lead to excessive photobleaching of the GFPem, that could result in an apparently reduced ribosome activity. Compared to the *in vitro* measurement, the lack of a photoprotection system and the constant focus drift, due to the temperature variation inside the imaging chamber, can complicate the *in situ* measurement. The focus drift may be the result of the manual temperature control and the relatively small, hence temperature-sensitive heater plate, an issue that may be solved by implementing an environmental heater chamber system with a greater thermal stability. A reduced activity compared to the *in vitro* measurement was observed, which may not only be an effect of the measurement procedure, but the result of several factors that are directly related to the surface binding of the ribosomes, such as their orientation on the surface, their resulting limited accessibility to the reaction mix components etc. Nonetheless, the simultaneous dual-color imaging with the WFM allowed to follow the increasing number of synthesized GFP over time.

Furthermore, the WFM was employed to determine the time of stability of an oligonucleotide hybridized to a ribosome subunit, at a concentration below k_d of the construct. Continuous imaging allowed to determine the time of stability, by following the number of identified peaks on the surface over time, utilizing the fact, that released oligonucleotides do not bind to the surface at the considered concentration. The monitoring of the number of identified peaks over time is therefore a simple and straightforward method to determine the time of stability of the construct below k_d, complimenting a solution measurement on a confocal measurement, where it would be more difficult to distinguish between a bound oligonucleotide and free oligonucleotide. Within the determined time-window, a similar measurement with double-labeled reassociated ribosomes was done to investigate if it is possible to observe their possible dissociation at pM-concentration during the previously determined time of stability. Since a decrease in the fraction of colocalized signals was not observed, it was concluded that the ribosomes, tethered to the surface, do not dissociate at the low employed pM-concentrations within the time of observation.

Appendix A

Appendix

A.1 Filter spectra

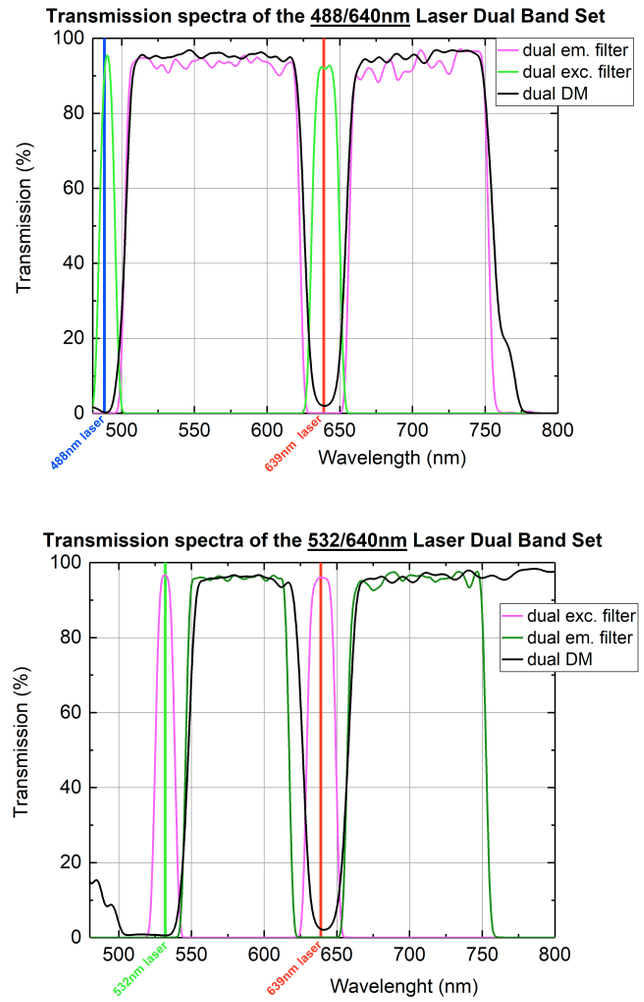

FIGURE A.1: The transmission spectra of both dual band sets used in this setup: The transmission spectra of the $488\,\mathrm{nm}/\ 640\,\mathrm{nm}$ and the $532\,\mathrm{nm}/\ 640\,\mathrm{nm}$ dual band set consisting of the spectra for the excitation filter, the dichroic mirror and the emission filter.

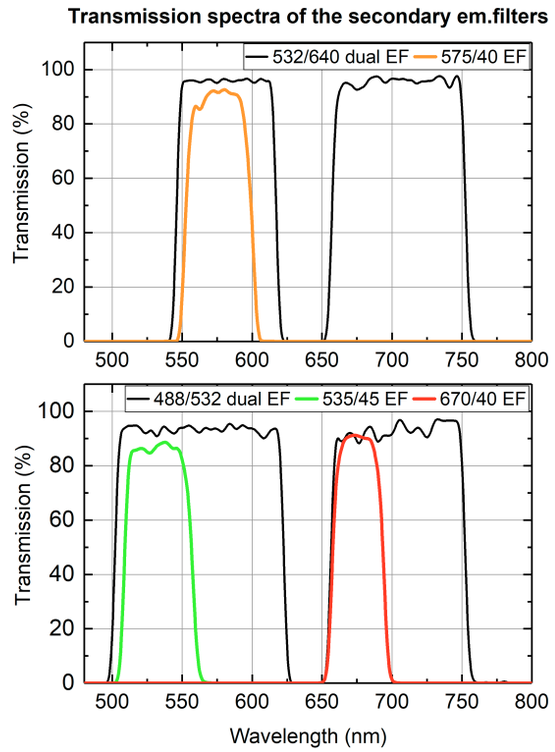

FIGURE A.2: The transmission spectra of the secondary emission filters used to determine the resolving power of the setup in 3 different spectral ranges: 535/40nm, 575/50nm and 670/40nm.

A.2 Convolution of the setup's transmission function with the emission spectra of the employed fluorophores

The normalized emission spectra of the five fluorophores and its convolution with the transmission function t_{tot} of the respective signal channel are given in figure A.3. Starting from the total fluorescence output of a fluorophore, 41.9% of the output enters the objective (section 4.1.2 on page 21). Approximately half of the photons, that enter the emission path, are lost due to the filter sets, the transmission function of the objective and the quantum efficiency of the camera. As a result, only between 20% and 25% of the fluorophore's emitted signal takes part in the image formation.

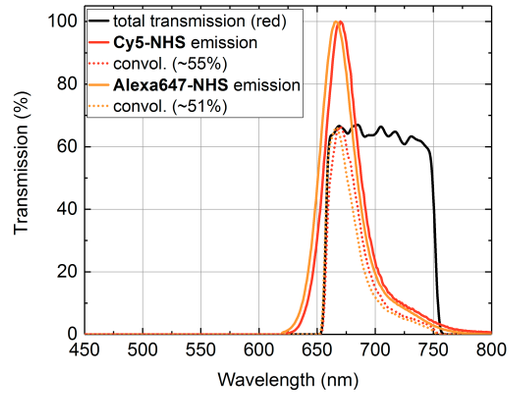

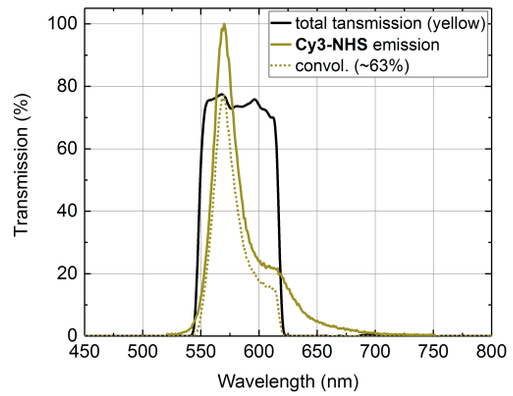

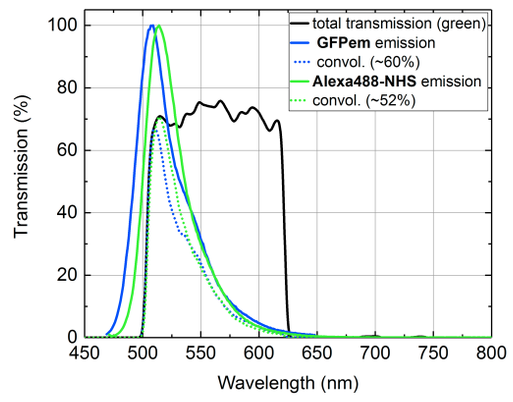

FIGURE A.3: The total transmission spectra of all the three spectral ranges along with the emission spectra of the fluorophores. Their convolution with the corresponding transmission function is represented by the dotted lines.

A.3 Illumination intensity

Table A.1 lists the excitation intensities [$\frac{photon}{cm^2 s}$] for the three laser sources, as derived in section 4.2.1 on page 29. Taking into account the molecular absorption cross sections σ of the fluorophores (4.2.1 on page 29), the number of absorbed photons per fluorophore per frame is on the the order of $10^4\,\gamma/\mathrm{s}$.

	λ_{ex}**=488nm** E_γ=4.071×10^{-19} W	λ_{ex}**=532nm** E_γ=3.734×10^{-19} W	λ_{ex}**=639nm** E_γ=3.109×10^{-19} W
Set power [mW]	photon flux at surface [$10^{19} \cdot \frac{photon}{cm^2 s}$]		
	Green/Red	Yellow/Red	Green/Red
15	-	1.3 ± 0.1	1.6 ± 0.1
20	1.8 ± 0.1	1.8 ± 0.1	2.2 ± 0.1
25	2.3 ± 0.1	2.3 ± 0.1	2.8 ± 0.2
50	4.8 ± 0.3	4.7 ± 0.3	5.7 ± 0.3
75	7.4 ± 0.4	7.2 ± 0.4	8.3 ± 0.5
100	9.9 ± 0.6	9.5 ± 0.6	11.1 ± 0.6
125	12.5 ± 0.8	12.0 ± 0.7	-
150	15.2 ± 0.9	14.4 ± 0.9	-
175	17.5 ± 1.1	-	-
200	20.0 ± 1.2	-	-

TABLE A.1: Power densities at the surface derived from the power measurements shown in figure 4.5

A.4 Determination of the molecular brightness

The average molecular brightness mB was estimated by summing up the number of photons collected within a 8x8 pixel array ($\equiv 640\,\mathrm{nm} \times 640\,\mathrm{nm}$, comprising the peak area) around the brightest pixel of a fluorescence peak. The histogram, composed of several thousand entries, was again fitted by a log-normal distribution. The fit's arithmetic mean of collected photons per molecule per frame, divided by 1.5 (illumination time of $1.5\mathrm{s}$), corresponds to the fluorophore's average molecular brightness mB, the determined values are listed in table A.2.

TABLE A.2: The fluorophores' molecular brightness and the average number of emitted photons emitted per second at the applied excitation power.

Fluorophore	mB ($\frac{N_\gamma}{molecule \cdot s}$)	$P_{meas}(mW)$
Alexa488	$(19.1 \pm 0.8) \cdot 10^3$	19
Cy5	$(4.9 \pm 0.1) \cdot 10^3$	7
GFPemerald	$(4.3 \pm 0.1) \cdot 10^3$	11
Alexa647	$(4.1 \pm 0.1) \cdot 10^3$	7
Cy3	$(3.8 \pm 0.1) \cdot 10^3$	9

Acknowledgements

My gratitude goes to Prof. Dr. Jörg Fitter, who offered me a position within the group of ICS-5 and introduced me to the interdisciplinary field of molecular biophysics. I also want to thank Prof. Dr. Andreas Offenhäusser for kindly accepting to review my thesis.
I also want to thank all the members of ICS-5, in particular Dr. Tina Züchner for introducing me to the field of fluorescence microscopy, for her general scientific advice and for providing me the analysis routine, that was of a great help during the processing of the large number of acquired images.
An essential component of my measurements was the surface preparation of the cover slides, the canvas for my surface measurements. Dr. Iris von der Hocht provided me the protocol for the surface functionalization and gave me helpful advice during the preparation steps.
Cristina Remes and Dr. Alexandros Katranidis did the time-consuming ribosome preparation and characterization and provided me a working biological sample.
Dr. Noémie Kempf and Henning Höfig performed the TCCD measurements and provided me their results, that allowed me compare and validate the results from my measurements acquired with the WFM.
I also want to thank Dr. Michele Cerminara for the helpful scientific discussions towards the end of my studies.

A surface measurement on single-molecule level is a delicate task. Its success relies on the careful planning, the effective interplay between all the involved components, the handling skills of the experimenter and sometimes, a quantum of luck. While a successful experiment feels more reassuring, a failed experiment can be a gain in its own way. What i consider an important part of my time as a PhD student were the constant discussions and exchange of thoughts, that followed an experiment, leading to changes in the design of experiments and further steps in the process and ultimately to the goal of my project.

Last but not least, i want to thank my parents and my sister Sena for their continuous support and my girlfriend Dragana for her love and encouragement.

Bibliography

[1] Barry R Masters. "The Development of Fluorescence Microscopy". In: *Encyclopedia of Life Sciences* (2010). DOI: 10.1002/9780470015902.a0022093.

[2] Malte Renz. "Fluorescence microscopy-A historical and technical perspective". In: *Cytometry Part A* 83.9 (2013), 767–779. DOI: 10.1002/cyto.a.22295.

[3] *Fluoreszenzmikroskopie*. URL: https://med.scio.pw/Lex/Fluoreszenzmikroskopie (visited on 07/07/2017).

[4] Ruchuan Liu, Yuliang Li, and Liyu Liu. "Single molecule fluorescence spectroscopy for quantitative biological applications". In: *Quantitative Biology* 4.3 (2016), 177–191. DOI: 10.1007/s40484-016-0083-0.

[5] Ph. Ellinger and A. Hirt. "Mikroskopische Beobachtungen an lebenden Organen mit Demonstrationen (Intravitalmikroskopie)". In: *Archiv für Experimentelle Pathologie und Pharmakologie* 147.1-3 (1929), 63–63. DOI: 10.1007/bf01946036.

[6] W. Heubner and B. Behrens. "Eröffnungsansprache". In: *Verhandlungen der Deutschen Pharmakologischen Gesellschaft* (1929), 14–17. DOI: 10.1007/978-3-662-33817-9_2.

[7] Evgenii M. Brumberg. "Fluorescence microscopy of biological objects using light from above". In: *Biophysics* 4 (1959), pp. 97–104.

[8] Friedrich Walter and Johan Sebastiaan Ploem. *Multi-Wavelength Epi-Illumination in Fluorescence Microscopy*. 2001. URL: http://www.leica-microsystems.com/science-lab/multi-wavelength-epi-illumination-in-fluorescence-microscopy/#c64517 (visited on 07/07/2017).

[9] H. Hampel M. Heitinger. "Ein neue Beleuchtungsverfahren für mikrophotographische Zwecke". In: *Zeitschrift für mikroskopisch-anatomische Forschung* 33 (1933), pp. 193–221.

[10] A. H. Coons, H. J. Creech, and R. N. Jones. "Immunological Properties of an Antibody Containing a Fluorescent Group." In: *Experimental Biology and Medicine* 47.2 (1941), 200–202. DOI: 10.3181/00379727-47-13084p.

[11] Osamu Shimomura, Frank H. Johnson, and Yo Saiga. "Extraction, Purification and Properties of Aequorin, a Bioluminescent Protein from the Luminous Hydromedusan,Aequorea". In: *Journal of Cellular and Comparative Physiology* 59.3 (1962), 223–239. DOI: 10.1002/jcp.1030590302.

[12] Richard N. Day and Michael W. Davidson. "The fluorescent protein palette: tools for cellular imaging". In: *Chemical Society Reviews* 38.10 (2009), p. 2887. DOI: 10.1039/b901966a.

[13] N. C. Shaner, G. H. Patterson, and M. W. Davidson. "Advances in fluorescent protein technology". In: *Journal of Cell Science* 120.24 (2007), 4247–4260. DOI: 10.1242/jcs.005801.

[14] Roger Y. Tsien. "The Green Fluorescent Protein". In: *Annual Review of Biochemistry* 67.1 (1998), 509–544. DOI: 10.1146/annurev.biochem.67.1.509.

[15] Patrick J. Macdonald, Yan Chen, and Joachim D. Mueller. "Chromophore maturation and fluorescence fluctuation spectroscopy of fluorescent proteins in a cell-free expression system". In: *Analytical Biochemistry* 421.1 (2012), 291–298. DOI: 10.1016/j.ab.2011.10.040.

[16] Roger Heim and Roger Y Tsien. "Engineering green fluorescent protein for improved brightness, longer wavelengths and fluorescence resonance energy transfer". In: *Current Biology* 6.2 (1996), 178–182. DOI: 10.1016/s0960-9822(02)00450-5.

[17] Alan M. McLennan Serina Stretton Somkiet Techkarnjanaruk and Amanda E. Goodman. "Use of Green Fluorescent Protein To Tag and Investigate Gene Expression in Marine Bacteria". In: *Applied and Environmental Microbiology* 64.7 (1998), 2554–2559.

[18] Diane Schroeder Hannali Webber Bradley J. Feilmeier Ginger Iseminger and Gregory J. Phillips. "Green Fluorescent Protein Functions as a Reporter for Protein Localization in Escherichia coli". In: *Journal of Bacteriology* 182.14 (2000), 4068–4076.

[19] Graham T. Dempsey et al. "Photoswitching Mechanism of Cyanine Dyes". In: *Journal of the American Chemical Society* 131.51 (2009), pp. 18192–18193. DOI: 10.1021/ja904588g. URL: https://doi.org/10.1021/ja904588g.

[20] Masafumi Minoshima and Kazuya Kikuchi. "Photostable and photoswitching fluorescent dyes for super-resolution imaging". In: *JBIC Journal of Biological Inorganic Chemistry* 22.5 (2017), pp. 639–652. DOI: 10.1007/s00775-016-1435-y. URL: https://doi.org/10.1007/s00775-016-1435-y.

[21] Graham T Dempsey et al. "Evaluation of fluorophores for optimal performance in localization-based super-resolution imaging". In: *Nature Methods* 8.12 (2011), pp. 1027–1036. DOI: 10.1038/nmeth.1768. URL: https://doi.org/10.1038/nmeth.1768.

[22] Y Hiraoka, J. Sedat, and D. Agard. "The use of a charge-coupled device for quantitative optical microscopy of biological structures". In: *Science* 238.4823 (1987), 36–41. DOI: 10.1126/science.3116667.

[23] E. J. Ambrose. "A Surface Contact Microscope for the study of Cell Movements". In: *Nature* 178.4543 (1956), 1194–1194. DOI: 10.1038/1781194a0.

[24] D Axelrod, T P Burghardt, and N L Thompson. "Total Internal Reflection Fluorescence". In: *Annual Review of Biophysics and Bioengineering* 13.1 (1984), 247–268. DOI: 10.1146/annurev.bb.13.060184.001335.

[25] Daniel Axelrod. "Total Internal Reflection Fluorescence Microscopy in Cell Biology". In: *Traffic* 2.11 (2001), 764–774. DOI: 10.1034/j.1600-0854.2001.21104.x.

[26] M. Minsky. "Memoir on inventing the confocal scanning microscope". In: *Scanning* 10.4 (1988), 128–138. DOI: 10.1002/sca.4950100403.

[27] Alexandros Katranidis et al. "Fast Biosynthesis of GFP Molecules: A Single-Molecule Fluorescence Study". In: *Angewandte Chemie International Edition* 48.10 (2009), 1758–1761. DOI: 10.1002/anie.200806070.

[28] James B. Munro et al. "A new view of protein synthesis: Mapping the free energy landscape of the ribosome using single-molecule FRET". In: *Biopolymers* 89.7 (2008), 565–577. DOI: 10.1002/bip.20961.

[29] Taekjip Ha. "Single-Molecule Fluorescence Resonance Energy Transfer". In: *Methods* 25.1 (2001), 78–86. DOI: 10.1006/meth.2001.1217.

[30] Sander Verbrugge, Lukas C. Kapitein, and Erwin J.g. Peterman. "Kinesin Moving through the Spotlight: Single-Motor Fluorescence Microscopy with Submillisecond Time Resolution". In: *Biophysical Journal* 92.7 (2007), 2536–2545. DOI: 10.1529/biophysj.106.093575.

[31] Martin Böhmer and Jörg Enderlein. "Orientation imaging of single molecules by wide-field epifluorescence microscopy". In: *Journal of the Optical Society of America B* 20.3 (2003), p. 554. DOI: 10.1364/josab.20.000554.

[32] Rudolf Rigler, Jerker Widengren, and Ülo Mets. "Interactions and Kinetics of Single Molecules as Observed by Fluorescence Correlation Spectroscopy". In: *Fluorescence Spectroscopy* (1993), 13–24. DOI: 10.1007/978-3-642-77372-3_2.

[33] Angel Orte, Richard Clarke, and David Klenerman. "Single-molecule two-colour coincidence detection to probe biomolecular associations". In: *Biochemical Society Transactions* 38.4 (2010), 914–918. DOI: 10.1042/bst0380914.

[34] Christoph Zander, Jörg Enderlein, and Richard A Keller. *Single molecule detection in solution - methods and applications*. 1. Aufl. Weinheim: Wiley-VCH, 2002. ISBN: 978-3-527-40310-3.

[35] Peter Tc So and Chen Y Dong. "Fluorescence Spectrophotometry". In: *Encyclopedia of Life Sciences* (2001). DOI: 10.1038/npg.els.0002978.

[36] J. R. Albani. *Structure and dynamics of macromolecules: absorption and fluorescence studies*. Elsevier, 2004.

[37] Michelle T. Z. Spence and Iain D. Johnson. *The molecular probes handbook: a guide to fluorescent probes and labeling technologies*. Live Technologies Corporation, 2010.

[38] Steven A. Soper, Quincy L. Mattingly, and Pradeep. Vegunta. "Photon burst detection of single near-infrared fluorescent molecules". In: *Analytical Chemistry* 65.6 (1993), 740–747. DOI: 10.1021/ac00054a015.

[39] Donald A. McQuarrie and John D. Simon. *Physical chemistry: a molecular approach*. Viva Books, 2013.

[40] S. E. Braslavsky. "GLOSSARY OF TERMS USED IN PHOTOCHEMISTRY, 3rd EDITION (IUPAC Recommendations 2006)". In: *Pure and Applied chemistry* 79.3 (), pp. 293–465. DOI: 10.1515/iupac.79.0029.

[41] Alberto Diaspro et al. "Photobleaching". In: *Handbook Of Biological Confocal Microscopy* (2006), 690–702. DOI: 10.1007/978-0-387-45524-2_39.

[42] Wolfgang Demtröder. *Experimentalphysik 2 - Elektrizität und Optik*. 6. Aufl. Berlin Heidelberg New York: Springer-Verlag, 2014. ISBN: 978-3-642-29944-5.

[43] Eugene Hecht. *Optics*. Pearson, 2016.

[44] *Understanding Microscopes and Objectives*. URL: https://www.edmundoptics.com/resources/application-notes/microscopy/understanding-microscopes-and-objectives/ (visited on 07/14/2017).

[45] Beyer H. *Handbuch der Mikroskopie, Zweite Auflage*. VEB Technik Verlag, 1985.

[46] Udo J. Birk. *Super-resolution microscopy: a practical guide*. Wiley-VCH, 2017.

[47] *Education in Microscopy and Digital Imaging*. URL: http://zeiss-campus.magnet.fsu.edu/articles/basics/resolution.html (visited on 07/14/2017).

[48] Simon Sindbert et al. "Accurate Distance Determination of Nucleic Acids via Forster Resonance Energy Transfer: Implications of Dye Linker Length and Rigidity". In: *Journal of the American Chemical Society* 133.8 (2011), 2463–2480. DOI: 10.1021/ja105725e.

[49] M. Dorywalska. "Site-specific labeling of the ribosome for single-molecule spectroscopy". In: *Nucleic Acids Research* 33.1 (2005), 182–189. DOI: 10.1093/nar/gki151.

[50] Colin Echeverría Aitken, R. Andrew Marshall, and Joseph D. Puglisi. "An Oxygen Scavenging System for Improvement of Dye Stability in Single-Molecule Fluorescence Experiments". In: *Biophysical Journal* 94.5 (2008), 1826–1835. DOI: 10.1529/biophysj.107.117689.

[51] Luis A Campos et al. "A photoprotection strategy for microsecond-resolution single-molecule fluorescence spectroscopy". In: *Nature Methods* 8.2 (2011), 143–146. DOI: 10.1038/nmeth.1553.

[52] Cristina Remeş. "Translation initiation with 70S ribosomes : a single molecule study". PhD thesis. Publikationsserver der RWTH Aachen University, 2018.

[53] Hiroyuki Ohashi et al. "A Highly Controllable Reconstituted Cell-Free System -a Breakthrough in Protein Synthesis Research". In: *Current Pharmaceutical Biotechnology* 11.3 (2010), 267–271. DOI: 10.2174/138920110791111889.

[54] Noémie Kempf et al. "A Novel Method to Evaluate Ribosomal Performance in Cell-Free Protein Synthesis Systems". In: *Scientific Reports* 7 (2017), p. 46753. DOI: 10.1038/srep46753.

[55] *Spatial Filters Tutorial*. URL: https://www.thorlabs.com/newgrouppage9.cfm?objectgroup_id=10768 (visited on 09/09/2017).

[56] *Achromat, Apochromat, Superachromat – What is the Difference?* URL: http://lenspire.zeiss.com/en/apochromat/ (visited on 09/09/2017).

[57] C. E. Shannon. "A Mathematical Theory of Communication". In: *Bell System Technical Journal* 27.4 (1948), 623–656. DOI: 10.1002/j.1538-7305.1948.tb00917.x.

[58] H. Nyquist. "Certain Topics in Telegraph Transmission Theory". In: *Transactions of the American Institute of Electrical Engineers* 47.2 (1928), pp. 617–644. ISSN: 0096-3860.

[59] *Electron-Multiplying (EM) Gain*. URL: https://www.qimaging.com/resources/pdfs/emccd_technote.pdf (visited on 09/09/2017).

[60] *CCD Signal to Noise Ratio*. URL: http://www.andor.com/learning-academy/ccd-signal-to-noise-ratio-calculating-the-snr-of-a-ccd (visited on 07/15/2017).

[61] G.i. Mashanov and J.e. Molloy. "Automatic Detection of Single Fluorophores in Live Cells". In: *Biophysical Journal* 92.6 (2007), 2199–2211. DOI: 10.1529/biophysj.106.081117.

[62] I. Izeddin et al. "Wavelet analysis for single molecule localization microscopy". In: *Optics Express* 20.3 (2012), p. 2081. DOI: 10.1364/oe.20.002081.

[63] Ulrich Kubitscheck et al. "Imaging and Tracking of Single GFP Molecules in Solution". In: *Biophysical Journal* 78.4 (2000), 2170–2179. DOI: 10.1016/s0006-3495(00)76764-6.

[64] David Grünwald et al. "Calibrating excitation light fluxes for quantitative light microscopy in cell biology". In: *Nature Protocols* 3.11 (2008), 1809–1814. DOI: 10.1038/nprot.2008.180.

[65] *Astronomical Optics*. URL: https://www.handprint.com/ASTRO/ae4.html (visited on 09/09/2017).

[66] *Water Immersion Objectives*. URL: https://www.microscopyu.com/microscopy-basics/water-immersion-objectives (visited on 10/14/2017).

[67] Stelzer. "Contrast, resolution, pixelation, dynamic range and signal-to-noise ratio: fundamental limits to resolution in fluorescence light microscopy". In: *Journal of Microscopy* 189.1 (1998), 15–24. DOI: 10.1046/j.1365-2818.1998.00290.x.

[68] Peter J. Shaw. "Comparison of Widefield/Deconvolution and Confocal Microscopy for Three-Dimensional Imaging". In: *Handbook Of Biological Confocal Microscopy* (2006), 453–467. DOI: 10.1007/978-0-387-45524-2_23.

[69] Mark B. Cannell, Angus McMorland, and Christian Soeller. "Image Enhancement by Deconvolution". In: *Handbook Of Biological Confocal Microscopy*. Ed. by James B. Pawley. Boston, MA: Springer US, 2006, pp. 488–500. ISBN: 978-0-387-45524-2.

[70] O. Schulz et al. "Resolution doubling in fluorescence microscopy with confocal spinning-disk image scanning microscopy". In: *Proceedings of the National Academy of Sciences* 110.52 (2013), 21000–21005. DOI: 10.1073/pnas.1315858110.

[71] Bo Huang, Mark Bates, and Xiaowei Zhuang. "Super-Resolution Fluorescence Microscopy". In: *Annual Review of Biochemistry* 78.1 (2009), 993–1016. DOI: 10.1146/annurev.biochem.77.061906.092014.

[72] Donna J. Webb and Claire M. Brown. "Epi-Fluorescence Microscopy". In: *Methods in Molecular Biology Cell Imaging Techniques* (2012), 29–59. DOI: 10.1007/978-1-62703-056-4_2.

[73] Siegfried Weisenburger and Vahid Sandoghdar. “Light microscopy: an ongoing contemporary revolution”. In: *Contemporary Physics* 56.2 (2015), 123–143. DOI: 10.1080/00107514.2015.1026557.

[74] *quantitative fcs: determination of the confocal volume by FCS and Bead Scanning with the Micro Time 200*. URL: https://www.picoquant.com/images/uploads/page/files/7351/appnote_quantfcs.pdf (visited on 08/02/2017).

[75] *Calculate and Fit FCS Traces with the FCS Script*. URL: https://www.picoquant.com/images/uploads/downloads/calculate_and_fit_fcs-traces_with_the_fcs-script_step_by_step.pdf (visited on 08/02/2017).

[76] Angel Orte, Richard Clarke, and David Klenerman. “Single-molecule two-colour coincidence detection to probe biomolecular associations”. In: *Biochemical Society Transactions* 38.4 (2010), 914–918. DOI: 10.1042/bst0380914.

[77] Ikuko Koyama-Honda et al. “Fluorescence Imaging for Monitoring the Colocalization of Two Single Molecules in Living Cells”. In: *Biophysical Journal* 88.3 (2005), 2126–2136. DOI: 10.1529/biophysj.104.048967.

[78] *Introduction to Fluorescence Microscopy*. URL: https://www.microscopyu.com/techniques/fluorescence/introduction-to-fluorescence-microscopy (visited on 07/14/2017).

[79] Joseph R. Lakowicz. *Principles of Fluorescence Spectroscopy*. Springer Verlag, 2016.

[80] Christopher P. Toseland. “Fluorescent labeling and modification of proteins”. In: *Journal of Chemical Biology* 6.3 (2013), 85–95. DOI: 10.1007/s12154-013-0094-5.

[81] Ratnakar B. Mujumdar et al. “Cyanine dye labeling reagents: Sulfoindocyanine succinimidyl esters”. In: *Bioconjugate Chemistry* 4.2 (1993), 105–111.

[82] *Cyanine dyes*. URL: http://www.atdbio.com/content/32/Cyanine-dyes (visited on 07/14/2017).

[83] Marcia Levitus and Suman Ranjit. “Cyanine dyes in biophysical research: the photophysics of polymethine fluorescent dyes in biomolecular environments”. In: *Quarterly Reviews of Biophysics* 44.01 (2010), 123–151. DOI: 10.1017/s0033583510000247.

[84] Jerker Widengren and Petra Schwille. “Characterization of Photoinduced Isomerization and Back-Isomerization of the Cyanine Dye Cy5 by Fluorescence Correlation Spectroscopy”. In: *The Journal of Physical Chemistry A* 104.27 (2000), 6416–6428. DOI: 10.1021/jp000059s.

[85] Ke Jia et al. “Characterization of Photoinduced Isomerization and Intersystem Crossing of the Cyanine Dye Cy3”. In: *The Journal of Physical Chemistry A* 111.9 (2007), 1593–1597. DOI: 10.1021/jp067843i.

[86] Judith E. Berlier et al. “Quantitative Comparison of Long-wavelength Alexa Fluor Dyes to Cy Dyes: Fluorescence of the Dyes and Their Bioconjugates”. In: *Journal of Histochemistry Cytochemistry* 51.12 (2003), 1699–1712. DOI: 10.1177/002215540305101214.

[87] Richa Dave et al. "Mitigating Unwanted Photophysical Processes for Improved Single-Molecule Fluorescence Imaging". In: *Biophysical Journal* 96.6 (2009), 2371–2381. DOI: 10.1016/j.bpj.2008.11.061.

[88] Laura C. Zanetti-Domingues et al. "Hydrophobic Fluorescent Probes Introduce Artifacts into Single Molecule Tracking Experiments Due to Non-Specific Binding". In: *PLOS ONE* 8.9 (Sept. 2013), pp. 1–11. DOI: 10.1371/journal.pone.0074200.

[89] Nataliya Panchuk-Voloshina et al. "Alexa Dyes, a Series of New Fluorescent Dyes that Yield Exceptionally Bright, Photostable Conjugates". In: *Journal of Histochemistry Cytochemistry* 47.9 (1999), 1179–1188. DOI: 10.1177/002215549904700910.

[90] *Alexa® dyes*. URL: http://www.atdbio.com/content/34/Alexa-dyes (visited on 07/14/2017).

[91] *Fluorescence quantum yields (QY) and lifetimes (τ) for Alexa Fluor dyes-Table 1.5*. URL: http://www.thermofisher.com/de/de/home/references/molecular-probes-the-handbook/tables/fluorescence-quantum-yields-and-lifetimes-for-alexa-fluor-dyes.html (visited on 07/14/2017).

[92] *The Alexa Fluor Dye Series-Note 1.1*. URL: http://www.thermofisher.com/de/de/home/references/molecular-probes-the-handbook/technical-notes-and-product-highlights/the-alexa-fluor-dye-series.html (visited on 07/14/2017).

[93] Fan Yang, Larry G. Moss, and George N. Phillips. "The molecular structure of green fluorescent protein". In: *Nature Biotechnology* 14.10 (1996), 1246–1251. DOI: 10.1038/nbt1096-1246.

[94] Andrew B. Cubitt, Leslie A. Woollenweber, and Roger Heim. "Chapter 2: Understanding Structure—Function Relationships in the Aequorea victoria Green Fluorescent Protein". In: *Methods in Cell Biology Green Fluorescent Proteins* (1998), 19–30. DOI: 10.1016/s0091-679x(08)61946-9.

[95] C.r. Bagshaw and D. Cherny. "Blinking fluorophores: what do they tell us about protein dynamics?" In: *Biochemical Society Transactions* 34.5 (2006), 979–982. DOI: 10.1042/bst0340979.

[96] Andor. *iXon EMCCD Cameras*. URL: http://www.andor.com/cameras/ixon-emccd-camera-series (visited on 07/15/2017).

[97] Sarah A. Mutch et al. "Deconvolving Single-Molecule Intensity Distributions for Quantitative Microscopy Measurements". In: *Biophysical Journal* 92.8 (2007), 2926–2943. DOI: 10.1529/biophysj.106.101428.

[98] David Dussault and Paul Hoess. "Noise performance comparison of ICCD with CCD and EMCCD cameras". In: *Infrared Systems and Photoelectronic Technology* (2004). DOI: 10.1117/12.561839.

[99] *CCD Signal-To-Noise Ratio*. URL: https://www.microscopyu.com/tutorials/ccd-signal-to-noise-ratio (visited on 07/14/2017).

[100] Peter Hinterdorfer and Antoine Van Oijen. *Handbook of single-molecule biophysics*. Springer, 2009.

[101] Qinsi Zheng et al. “The Contribution of Reactive Oxygen Species to the Photobleaching of Organic Fluorophores”. In: *Photochemistry and Photobiology* 90.2 (2013), 448–454. DOI: 10.1111/php.12204.

[102] Yoshie Harada et al. “Mechanochemical coupling in actomyosin energy transduction studied by in vitro movement assay”. In: *Journal of Molecular Biology* 216.1 (1990), 49–68. DOI: 10.1016/s0022-2836(05)80060-9.

[103] Ruth E. Benesch and Reinhold Benesch. “Enzymatic Removal of Oxygen for Polarography and Related Methods”. In: *Science* 118.3068 (1953), pp. 447–448. ISSN: 0036-8075. DOI: 10.1126/science.118.3068.447.

[104] Toshio Yanagida et al. “Direct observation of motion of single F-actin filaments in the presence of myosin”. In: *Nature* 307.5946 (1984), 58–60. DOI: 10.1038/307058a0.

[105] Taekjip Ha and Philip Tinnefeld. “Photophysics of Fluorescent Probes for Single-Molecule Biophysics and Super-Resolution Imaging”. In: *Annual Review of Physical Chemistry* 63.1 (2012), 595–617. DOI: 10.1146/annurev-physchem-032210-103340.

[106] Thorben Cordes, Jan Vogelsang, and Philip Tinnefeld. “On the Mechanism of Trolox as Antiblinking and Antibleaching Reagent”. In: *Journal of the American Chemical Society* 131.14 (2009), 5018–5019. DOI: 10.1021/ja809117z.

[107] Xinghua Shi, John Lim, and Taekjip Ha. “Acidification of the Oxygen Scavenging System in Single-Molecule Fluorescence Studies: In Situ Sensing with a Ratiometric Dual-Emission Probe”. In: *Analytical Chemistry* 82.14 (2010), 6132–6138. DOI: 10.1021/ac1008749.

[108] Leila Nahidiazar et al. “Optimizing Imaging Conditions for Demanding Multi-Color Super Resolution Localization Microscopy”. In: *Plos One* 11.7 (2016). DOI: 10.1371/journal.pone.0158884.

[109] Marko Swoboda et al. “Photostability without pH Drop - An Alternative Oxygen Scavenging System for Sinlge-Molecule FRET Experiments”. In: *Biophysical Journal* 102.3 (2012). DOI: 10.1016/j.bpj.2011.11.972.

[110] C. Zhang and J. B. Konopka. “A Photostable Green Fluorescent Protein Variant for Analysis of Protein Localization in Candida albicans”. In: *Eukaryotic Cell* 9.1 (2009), 224–226. DOI: 10.1128/ec.00327-09.

[111] Nathan C Shaner, Paul A Steinbach, and Roger Y Tsien. “A guide to choosing fluorescent proteins”. In: *Nature Methods* 2.12 (2005), 905–909. DOI: 10.1038/nmeth819.

[112] Taekjip Ha et al. “Initiation and re-initiation of DNA unwinding by the Escherichia coli Rep helicase”. In: *Nature* 419.6907 (2002), 638–641. DOI: 10.1038/nature01083.

[113] Ankur Jain et al. “Single-molecule pull-down for studying protein interactions”. In: *Nature Protocols* 7.3 (2012), 445–452. DOI: 10.1038/nprot.2011.452.

[114] Rajan Lamichhane et al. “Single-molecule FRET of protein–nucleic acid and protein–protein complexes: Surface passivation and immobilization”. In: *Methods* 52.2 (2010), 192–200. DOI: 10.1016/j.ymeth.2010.06.010.

[115] Kazuhiro Nakanishi, Takaharu Sakiyama, and Koreyoshi Imamura. “On the adsorption of proteins on solid surfaces, a common but very complicated phenomenon”. In: *Journal of Bioscience and Bioengineering* 91.3 (2001), 233–244. DOI: 10.1016/s1389-1723(01)80127-4.

[116] Boyang Hua et al. “An Improved Surface Passivation Method for Single-Molecule Studies”. In: *Biophysical Journal* 106.2 (2014). DOI: 10.1016/j.bpj.2013.11.2218.

[117] Y.l. Jeyachandran et al. “Efficiency of blocking of non-specific interaction of different proteins by BSA adsorbed on hydrophobic and hydrophilic surfaces”. In: *Journal of Colloid and Interface Science* 341.1 (2010), 136–142. DOI: 10.1016/j.jcis.2009.09.007.

[118] Stanley D. Chandradoss et al. “Surface Passivation for Single-molecule Protein Studies”. In: *Journal of Visualized Experiments* 86 (2014). DOI: 10.3791/50549.

Band / Volume 164
Impact and Regulatory Control of the CGP3 Prophage in *Corynebacterium glutamicum*
E. Pfeifer (2018), IV, 206 pp
ISBN: 978-3-95806-301-3

Band / Volume 165
Establishment of Bacterial Microcompartments in the Industrial Production Strain *Corynebacterium glutamicum*
I. Huber (2018), X, 114, XI-XXXIV pp
ISBN: 978-3-95806-302-0

Band / Volume 166
Current-Induced Magnetization Dynamics in Ferromagnetic Nanowires
M. I. Khan (2018), vi, 138 pp
ISBN: 978-3-95806-308-2

Band / Volume 167
Management of Electrophysiological Data & Metadata
Making complex experiments accessible to yourself and others
L. Zehl (2018), 182 pp
ISBN: 978-3-95806-311-2

Band / Volume 168
Investigation of GeSn as Novel Group IV Semiconductor for Electronic Applications
C. Schulte-Braucks, Christian (2018), xx, 165, XII pp
ISBN: 978-3-95806-312-9

Band / Volume 169
Tailoring the Electronic Properties of Epitaxial Oxide Films via Strain for SAW and Neuromorphic Applications
Y. Dai (2018), VI, 133 pp
ISBN: 978-3-95806-319-8

Band / Volume 170
The electronic structure of transition metal dichalcogenides investigated by angle-resolved photoemission spectroscopy
M. Gehlmann (2018), ii, 108, XVIII pp
ISBN: 978-3-95806-324-2

Band / Volume 171
Control of neuron adhesion by metal nanoparticles
A. Q. Tran (2018), viii, 108 pp
ISBN: 978-3-95806-332-7

Schriften des Forschungszentrums Jülich
Reihe Schlüsseltechnologien / Key Technologies

Band / Volume 172
Neutron Scattering
Lectures of the JCNS Laboratory Course held at Forschungszentrum Jülich and at the Heinz-Maier-Leibnitz Zentrum Garching
edited by T. Brückel, S. Förster, G. Roth, and R. Zorn (Eds.) (2018), ca 300 pp
ISBN: 978-3-95806-334-1

Band / Volume 173
Spin scattering of topologically protected electrons at defects
P. Rüßmann (2018), vii, 230 pp
ISBN: 978-3-95806-336-5

Band / Volume 174
Interfacing EuO in confined oxide and metal heterostructures
P. Lömker (2018), vi, 140 pp
ISBN: 978-3-95806-337-2

Band / Volume 175
Operando Chemistry and Electronic Structure of Electrode / Ferroelectric Interfaces
S. Gonzalez (2018), 159 pp
ISBN: 978-3-95806-341-9

Band / Volume 176
Magnetic Properties of Self-assembled Manganese Oxide and Iron Oxide Nanoparticles
Spin Structure and Composition
X. Sun (2018), ii, 178 pp
ISBN: 978-3-95806-345-7

Band / Volume 177
Model-based reconstruction of magnetisation distributions in nanostructures from electron optical phase images
J. Caron (2018), XXI, 183 pp
ISBN: 978-3-95806-346-4

Band / Volume 178
Simultaneous dual-color imaging on single-molecule level on a Widefield microscope and applications
R. Ledesch (2018), ix, 119 pp
ISBN: 978-3-95806-348-8

Weitere ***Schriften des Verlags im Forschungszentrum Jülich*** unter
http://wwwzb1.fz-juelich.de/verlagextern1/index.asp

Schlüsseltechnologien / Key Technologies
Band / Volume 178
ISBN 978-3-95806-348-8

Mitglied der Helmholtz-Gemeinschaft

JÜLICH
Forschungszentrum